

# **The development of stylolites, from small-scale heterogeneities to multi-scale roughness**

**Dissertation zur Erlangung des Grades  
„Doktor der Naturwissenschaften“ im Promotionsfach Geologie  
am Fachbereich Chemie, Pharmazie und Geowissenschaften  
der Johannes Gutenberg-Universität in Mainz**

**Marcus Johannes Ebner**

geb. in Linz / Österreich

Mainz, August 2009



## **Erklärung**

Hiermit versichere ich, die vorgelegte Arbeit selbstständig und unter Verwendung der angegebenen Quellen und Hilfsmittel verfasst zu haben.

Mainz, August 2009

Datum der mündlichen Prüfung: 6. November 2009





## Table of Contents

Table of Contents .....	I
Abstract .....	IV
Zusammenfassung .....	V
<b>1. Introduction .....</b>	<b>1</b>
1.1. Current state of the research .....	1
1.2. Motivation, objectives and methods .....	2
1.3. Organization of the thesis .....	4
1.4. References .....	5
<b>2. Stress sensitivity of stylolite morphology .....</b>	<b>9</b>
Abstract .....	9
2.1. Introduction .....	9
2.2. Stylolite data-set, roughness measurements and analysis .....	11
2.3. Results .....	14
2.4. Discussion & Conclusions .....	17
2.5. References .....	18
<b>3. Anisotropic scaling of tectonic stylolites: a fossilized signature of the stress field? .....</b>	<b>21</b>
Abstract .....	21
3.1. Introduction .....	21
3.2. Geological setting .....	24
3.3. Methodology .....	26
3.4. Data analysis .....	27
3.4.1. 1D analysis .....	27
3.4.2. 2D analysis .....	32
3.4.3. Synthetic data analysis .....	37
3.5. Discussion .....	39
3.6. Conclusions .....	41

3.7.	Appendix: Stress Calculation.....	42
3.7.1.	Part I.....	42
3.7.2.	Part II.....	42
3.8.	References .....	44
<b>4.</b>	<b>The influence of localized pressure solution at &amp; around stylolite interfaces: multi-scale quenched noise as roughness origin.....</b>	<b>47</b>
	Abstract .....	47
4.1.	Introduction.....	47
4.2.	Dataset and Methods.....	50
4.2.1.	Stylolite dataset .....	50
4.2.2.	Methodology (EBSD and OC settings).....	51
4.3.	Data Analysis & Results.....	52
4.3.1.	Noise around initial interfaces.....	52
4.3.2.	Noise around mature interface.....	58
4.3.3.	Matrix adjustments around mature interfaces .....	60
4.4.	Discussion .....	64
4.4.1.	Quenched noise around stylolites.....	64
4.4.2.	Matrix modifications around stylolite interfaces .....	65
4.5.	Conclusion .....	67
4.6.	References .....	68
<b>5.</b>	<b>The influence of rock heterogeneity on the scaling properties of simulated and natural stylolites .....</b>	<b>73</b>
	Abstract .....	73
5.1.	Introduction.....	73
5.2.	Numerical model setup .....	75
5.2.1.	Theory .....	76
5.2.2.	Basic numerical step.....	77
5.2.3.	Parameters, boundary conditions, limitations.....	78
5.3.	Data analysis & results.....	78
5.3.1.	Roughness exponents .....	80
5.3.2.	Interface growth .....	83
5.3.3.	Crossover length scales.....	88
5.4.	Discussion .....	90
5.5.	Conclusions.....	92

---

5.6.	References .....	92
<b>6.</b>	<b>Synthesis and general conclusions .....</b>	<b>95</b>
6.1.	Scaling of natural stylolites.....	95
6.2.	Initiation of stylolite roughness.....	96
6.3.	Formation of localized pressure solution features .....	97
6.4.	Outlook: suggestion for further research .....	98
6.5.	References .....	100
<b>7.</b>	<b>Appendix.....</b>	<b>101</b>
7.1.	Appendix A.....	101
7.2.	Appendix B .....	105
7.3.	Appendix C.....	111
	Curriculum Vitae.....	115

---

## Abstract

Stylolites are rough paired surfaces, indicative of localized stress-induced dissolution under a non-hydrostatic state of stress, separated by a clay parting which is believed to be the residuum of the dissolved rock. These structures are the most frequent deformation pattern in monomineralic rocks and thus provide important information about low temperature deformation and mass transfer. The intriguing roughness of stylolites can be used to assess amount of volume loss and paleo-stress directions, and to infer the destabilizing processes during pressure solution. But there is little agreement on how stylolites form and why these localized pressure solution patterns develop their characteristic roughness.

Natural bedding parallel and vertical stylolites were studied in this work to obtain a quantitative description of the stylolite roughness and understand the governing processes during their formation. Adapting scaling approaches based on fractal principles it is demonstrated that stylolites show two self affine scaling regimes with roughness exponents of 1.1 and 0.5 for small and large length scales separated by a crossover length at the millimeter scale. Analysis of stylolites from various depths proved that this crossover length is a function of the stress field during formation, as analytically predicted. For bedding parallel stylolites the crossover length is a function of the normal stress on the interface, but vertical stylolites show a clear in-plane anisotropy of the crossover length owing to the fact that the in-plane stresses ( $\sigma_2$  and  $\sigma_3$ ) are dissimilar. Therefore stylolite roughness contains a signature of the stress field during formation.

To address the origin of stylolite roughness a combined microstructural (SEM/EBSD) and numerical approach is employed. Microstructural investigations of natural stylolites in limestones reveal that heterogeneities initially present in the host rock (clay particles, quartz grains) are responsible for the formation of the distinctive stylolite roughness. A two-dimensional numerical model, i.e. a discrete linear elastic lattice spring model, is used to investigate the roughness evolving from an initially flat fluid filled interface induced by heterogeneities in the matrix. This model generates rough interfaces with the same scaling properties as natural stylolites. Furthermore two coinciding crossover phenomena in space and in time exist that separate length and timescales for which the roughening is either balanced by surface or elastic energies. The roughness and growth exponents are independent of the size, amount and the dissolution rate of the heterogeneities. This allows to conclude that the location of asperities is determined by a polimict multi-scale quenched noise, while the roughening process is governed by inherent processes i.e. the transition from a surface to an elastic energy dominated regime.

## Zusammenfassung

Stylolithen sind raue paarweise Oberflächen, indikativ für spannungsinduzierte Lösung in einem nicht hydrostatischen Spannungsfeld, welche von einer tonigen Zwischenschicht getrennt sind, die als Residuum des aufgelösten Gesteins angesehen wird. Diese Strukturen sind das häufigste Deformationsmuster in monomineralischen Gesteinen und liefern deshalb wichtige Erkenntnisse über Niedrigtemperatur-Deformation und Materialtransport. Die faszinierende Rauigkeit von Stylolithen kann dazu benutzt werden um die Menge des Volumsverlusts und die Paläospannungsrichtungen abzuschätzen, und die destabilisierenden Prozesse während der Drucklösung zu verstehen. Allerdings gibt es wenig Übereinstimmung darüber, wie sich Stylolithen bilden und wie diese lokalen Drucklösungsmuster ihre charakteristische Rauigkeit bilden.

Natürliche, schichtparallele und vertikale Stylolithen werden in dieser Arbeit untersucht, um eine quantitative Beschreibung der Stylolith-Rauigkeit zu erhalten und die vorherrschenden Prozesse bei ihrer Bildung zu verstehen. Die Benutzung einer Skalierungsmethode, die auf Prinzipien der fraktalen Geometrie basieren, ergab an Stylolithen zwei selbstaffine Skalierungsregime mit Rauigkeitsexponenten von 1.1 und 0.5 für kleine und großen Maßstäbe, welche von einer Übergangslänge im Millimeterbereich getrennt sind. Die Untersuchung von Stylolithen aus unterschiedlichen Tiefen belegt, dass diese Übergangslänge eine Funktion des Spannungsfeldes während der Bildung ist, wie von analytischen Modellen vorhergesagt. Für schichtparallele Stylolithen ist die Übergangslänge eine Funktion der Hauptnormalspannung, welche auf die Oberfläche wirkt, während vertikale Stylolithen eine deutliche Anisotropie der Übergangslänge zeigen, welche auf die unterschiedlichen Spannungen parallel zur Stylolithfläche ( $\sigma_2$  and  $\sigma_3$ ) zurückzuführen ist. Die Rauigkeit von Stylolithen enthält deshalb eine Signatur des Spannungsfeldes während der Bildung.

Um den Ursprung für die Stylolith-Rauigkeit zu verstehen, wird ein kombinierter Ansatz aus mikrostrukturellen (SEM/EBSD) und numerischen Untersuchungen verwendet. Diese mikro-strukturellen Untersuchungen von Stylolithen in Kalksteinen zeigen, dass Heterogenitäten, die ursprünglich im Gestein enthalten sind (Tonpartikel, Quarzkörner), verantwortlich für die Bildung der ausgeprägten Rauigkeit sind. Ein zweidimensionales numerisches Modell (im eigentlichen ein diskretes linear-elastisches hexagonales Federnmodell) wird benutzt, um die Entwicklung der Rauigkeit von einer anfänglich flachen, fluidgefüllten Grenzfläche zu untersuchen. Dieses Modell erzeugt raue Grenzflächen mit denselben Skalierungseigenschaften wie natürliche Stylolithen. Des Weiteren existieren zwei gleichartige Übergangsphänomene in räumlicher und zeitlicher Entwicklung, für welche die Rauigkeitsentwicklung entweder von Oberflächen- oder von elastischen Energien ausgeglichen werden. Die Rauigkeits- und Wachstumsexponenten sind jedoch unbeeinflusst von der Größe, der Anzahl und der Lösungsgeschwindigkeit der Heterogenitäten im System. Dies erlaubt das Fazit, dass die Position der Unebenheit der Oberfläche von unterschiedlichen mehrskaligen Heterogenitäten bestimmt wird,

wohingegen der Prozess des Aufrauens von inhärenten Prozessen, dem Übergang von einem Oberflächen- Energien zu einem von elastischen Energien dominierten Regime beherrscht wird.

# 1. Introduction

This thesis focuses on localized pressure solution features, one of the most frequent deformation patterns in sedimentary rocks. The motivation for this introductory chapter is threefold: First a short general introduction into pressure solution features is given. The main focus here lies on stylolites and the related scientific work up to now (a more specific introduction can be found in chapters 2, 3, 4 and 5). Major foundations of research on localized pressure solution and remaining questions are outlined and thus lead to the second part (motivation and objectives) of this introductory chapter. This second part focuses on the motivation arisen from the scientific literature and tries to emphasize the key issues and objectives of this thesis, simultaneously the methods to approach these issues are presented. These objectives are refereed to in the conclusion at the end of the thesis. In a third part, this introduction should give an overview of the organization of this thesis. Since chapters are organized in independent sections this part will focus on how these chapters meet the objectives and their interrelation outlined before.

## 1.1. Current state of the research

Pressure solution in sedimentary rocks manifests itself in either intergranular or localized dissolution of material (Tada & Siever 1989). Intergranular pressure solution occurs at contacts of individual grains (Sorby 1863). Localized pressure solution is responsible for the formation of stylolites (Stockdale 1922, Dunnington 1954, Heald 1955, Dunnington 1967, Park & Schot 1968, Buxton & Sibley 1981, Rutter 1983, Guzzetta 1984, Bayly 1986, Bathurst 1987, Tada & Siever 1989, Railsback 1993). Despite discrepancies, there is a general agreement that stylolites are rough interfaces which form by stress induced dissolution of monomineralic rock types under a non-hydrostatic state of stress. Stylolites are further distinguished by their characteristic roughness and by a clay parting which is believed to be the insoluble residuum of the dissolved rock (Railsback 1993). The wide morphological variety of stylolites invoked different qualitative descriptions which group stylolites into generic classes. One classification uses the orientation of the stylolite plane relative to bedding. Bedding-parallel stylolites are supposed to form due to the layer-normal overburden pressure, while tectonic stresses cause the formation of stylolites oblique or perpendicular to bedding (Park & Schot 1968, Railsback & Andrews 1995). A second classification is based on the orientation of the stylolite teeth relative to the stylolite plane. Here the term “stylolite” is used for teeth at a high angle to the plane, and “slickolite” for dissolution surfaces where the teeth are distinctly oblique to the dissolution plane (Bretz 1940, Gratier et al. 2005, Simon 2007). Finally the shape of the characteristic teeth-like asperities and spikes along the interface is used to characterize stylolites (Park & Schot 1968, Guzzetta 1984). More quantitative approaches showed that stylolites obey a fractal scaling over several

orders of magnitude (Drummond & Sexton 1998, Karcz & Scholz 2003). Investigation of the entire interface demonstrated that stylolites belong to a broader class of self-affine fractals, exhibiting two scaling regimes with two distinct roughness exponents on respective scales (Renard et al. 2004, Schmittbuhl et al. 2004).

In contrast, relatively little is known on the thickness of overburden required for bedding-parallel stylolites constraining the stress states and magnitudes necessary for stylolitization. The reported values of stylolite formation depth range from 800-1000 m (e.g. Railsback 1993) to a range of 500 m (Lind 1993) down to as little as 90 m for the formation of microstylolites (Tada & Siever 1989, and references cited therein), which corresponds to normal stress range of 24.5 to 2.2 MPa (assuming a constant density of 2.5 g/cm<sup>3</sup>).

A second controversial issue is the origin of the characteristic stylolite roughness. Based on field observations, microstructural investigations, numerical and analytical considerations, two main concepts for the roughening of stylolites prevail. In the first concept (termed *instability concept* in the following), a stress-induced roughening instability exists along an initially flat solid-solid interface (Angheluta et al. 2008) or solid-fluid-solid interface (Bonnetier et al. 2009). Although the studies of Angheluta et al. (2008) and Bonnetier et al. (2009) differ significantly, the roughening instability is induced by elastic stresses acting normal on the interface in both models. In addition it was demonstrated that stresses parallel to the interface can induce roughening if an initial perturbation exists (Gal & Nur 1998, Gal et al. 1998). In the second concept (Renard et al. 2004, Schmittbuhl et al. 2004, Koehn et al. 2007), the quenched noise, i.e. heterogeneities initially present in the host rock, is the destabilizing term responsible for roughening of the interface (and therefore termed *heterogeneity concept*). It is either surface or elastic energy which operates against these heterogeneities and thus acts as a stabilizing term on small and large length-scales, respectively.

Finally, a third issue on which controversial opinions can be found in the literature is the initiation of stylolites. Several theories based on field studies exist for the initiation of stylolites: (i) formation along preexisting planar anisotropies e.g. bedding-planes or compositional layering (Bathurst 1987); (ii) as anticracks, which propagate due to stress concentration at the anticrack tips; similar to mode I fractures (Fletcher & Pollard 1981), although this theory has been challenged (Katsman & Aharonov 2006); (iii) and finally by stress induced self-organization (Merino 1992, Railsback 1998, Fletcher & Merino 2001, Merino et al. 2006).

## 1.2. Motivation, objectives and methods

Pressure solution features such as stylolites are among the most prominent deformation patterns in sedimentary rocks and thus caught the continuing attention of the geoscientific community. Structural Geologists, especially those working in the field, investigate deformed rocks and deformation features, e.g. folds and fractures within those rocks to address questions of both scientific and economic interest. The general goal is to estimate the strain and the style of deformation by a detailed illustration of the



investigated structure. Such a geometric description in turn leads to the construction of a kinematic model which allows to trace back the evolution from an undeformed to a deformed state of every part of the investigate rock. But a kinematic model itself does not give information about the physical processes that generated a certain deformation feature in a rock. Nevertheless, a geometric/kinematic model is a crucial prerequisite to decipher and understand the governing physical processes responsible for the formation of deformation features.

Thus, this work aims to provide both, a quantitative description of natural pressure solution features and, building on this description, tries to explore the physical processes responsible for the development of localized pressure solution features. It is clear that stylolites with their intriguing roughness are one of the most prominent deformation patterns indicative of pressures solution in rocks of the upper crust. The abundance of stylolites and their wide spread occurrence in various monomineralic rock-types (Tada & Siever 1989) makes them one of the most promising candidates to study both, geometric characteristics and variability and the physical processes which govern the formation and dynamic evolution of localized pressure solution features. As outlined above, a considerable amount of research has been conducted on localized pressure solution features and especially on stylolites. But there are tree major research topics which remain controversial in the literature:

1. What is the best way to quantitatively characterize stylolites and what does a quantitative description tell us about the formation conditions (e.g. stress, strain, formation depth etc.)?
2. What is the reason for stylolite roughness to develop and how does this roughness evolve dynamically?
3. What causes the initiation of localized pressure solution and thus the origin of stylolites?

This thesis mainly focuses (1) on the quantitative characterization of stylolites and its implication for the formation conditions and (2) on the origin of the distinct roughness of stylolites; (3) in addition, the results presented here will give some qualitative indication on how stylolites probably initiate.

To address the first issues, a new approach is used, which is based on the pioneering works of Renard et al. (2004) and Schmittbuhl et al. (2004) who demonstrated that the roughness of stylolites can be described as self-affine surfaces with two distinct scaling regimes separated by a crossover length at the millimeter scale,. In addition, analytical considerations by these authors revealed that this crossover-length contains a signature of the stress field. The aim of this study is to apply these newly developed quantitative tools based on statistical physics principles to natural stylolites from various settings (e.g. varying structural levels, bedding parallel and tectonic stylolites) to investigate their roughness scaling. Both, 1D signals from polished slabs, and 2D surfaces from opened interfaces were investigated using image analysis and high resolution laser profilometry. This allows to decipher whether stylolite roughness can be used as a quantitative stress gauge and in addition examines if a general scaling law for stylolites exists.

To address the issue concerning the origin of stylolite roughness a twofold approach is chosen. First a detailed microstructural approach based on optical microscopy and SEM/EBSD (scanning electron

microscopy / electron backscatter diffraction) analysis combined with orientation contrast (OC) image analysis of stylolites in limestones is presented. The aim of this microstructural investigation is to reveal the role of quenched noise, i.e. heterogeneities initially present in the host-rock, on the initiation of this roughness. This should give insights on whether stylolite roughness is generated by a stress-induced instability or by the quenched material disorder. Following the qualitative identification of the quenched noise (i.e. the composition of the heterogeneity), a (semi-)quantitative characterization of the quenched disorder (i.e. spatial and size distribution of heterogeneities) is employed. This microstructural analysis seeks to provide a quantitative basis for the distribution of heterogeneities initially present during stylolite formation, which can be applied to construct realistic numerical models. The second part of our twofold approach facilitates such numerical simulations, which aim to understand the dynamic evolution of the roughness along stylolite interfaces. Based on the numerical model developed by Koehn et al. (2007) (i.e. a 2D linear elastic lattice spring model coupled with a dissolution routine at the interface), this study examines the influence of heterogeneities, which induce the roughening due to a dissolution rate constant smaller than that of the matrix. Varying the size, amount and dissolution rate of the heterogeneities in the system allows to exhibit the influence on the roughness evolving from an initially flat interface. Additionally a quantitative analysis based on statistical physics principles (applied to natural stylolites in previous chapters) facilitates a comparison between nature and numerical experiment. This approach permits the construction of scaling laws for stylolites in space and time. Beyond that, the rates at which the stylolite roughness grows give a possibility to constrain the amount of compaction necessary to produce a specific roughness in natural stylolites and thus give important indications on volume change along stylolites which can be applied in basin as well as tectonic research.

### 1.3. Organization of the thesis

This work resulted from an interdisciplinary research project at the Johannes Gutenberg University of Mainz, funded for a three year period by the DFG, in cooperation with researchers at Universities of Strasbourg, Grenoble, Stockholm and Tübingen. The thesis itself is structured in four main chapters (chapters 2, 3, 4 & 5), which are presented in a logical order in agreement with an easier comparison of the results and a thematic grouping.

*Chapter 2* represents the investigation of bedding parallel stylolites in limestones from various depths from an outcrop in southeastern France. Careful statistical analysis based on fractal analysis was carried out to demonstrate that the crossover-length, a characteristic of stylolite morphology, contains a signature of the stress field during formation, confirming analytical predictions. The work performed in this chapter is published in Earth and Planetary Science Letters.

*Chapter 3* reports the analysis of 3D morphology obtained by high-resolution laser profilometry of tectonic (vertical) stylolites in Jurassic limestones from locations in NE Spain and SW Germany. Application of the 1D statistical tools used in *chapter 2* demonstrates that an in-plane scaling anisotropy exists for tectonic stylolites which lead to the development of a new 2D-Fourier approach to capture the

full complexity of the roughness scaling of tectonic stylolites. The orientation of this anisotropy can be related to the principal stress directions and is thus related to the 3D stress field during formation. This chapter was submitted to *Journal of Geophysical Research – Solid Earth* and is currently under review.

*Chapter 4* comprises the results of a microstructural investigation conducted on bedding parallel and tectonic stylolites. This examination employs SEM and EBSD analysis to study the influence of quenched noise on the evolution of the stylolites roughness. Strong arguments for heterogeneities as roughness origin are put forward. In addition, matrix modifications around mature stylolite interfaces are investigated. The microstructural investigations presented in this chapter will be submitted to *Journal of Structural Geology* in the near future.

*Chapter 5* summarizes the experimental results of a numerical investigation of stylolite roughness based on a 2D linear elastic spring model. The size, amount and composition of the heterogeneities (i.e. the cause for the roughness) are systematically varied to investigate their influence on the evolving topography. Roughness of experimental stylolites is analyzed using the statistical tools of chapter 2 & 3. Furthermore the dynamic evolution of the roughness is analyzed and is finally compared to natural stylolites. The results of this chapter are published in *Journal of Structural Geology*.

Chapter 6 compiles the main conclusion of the thesis and its implications, in addition a short outlook on suggested further research is given based on the questions arisen during the course of this thesis. The appendix lists the most important *Matlab*© scripts used for data analysis in chapters 2, 3 & 5. Finally it has to be noticed that the four main chapters (2-5) are organized to serve as self-contained studies, each containing an abstract, introduction, methods, data-analysis, discussion and conclusion section.

## 1.4. References

- Angheluta, L., Jettestuen, E., Mathiesen, J., Renard, F. & Jamtveit, B. 2008. Stress-Driven Phase Transformation and the Roughening of Solid-Solid Interfaces. *Physical Review Letters* 100(9), 096105.
- Bathurst, R. G. C. 1987. Diagenetically Enhanced Bedding in Argillaceous Platform Limestones - Stratified Cementation and Selective Compaction. *Sedimentology* 34(5), 749-778.
- Bayly, B. 1986. A Mechanism for Development of Stylolites. *Journal of Geology* 94(3), 431-435.
- Bonnetier, E., Misbah, C., Renard, F., Toussaint, R. & Gratier, J. P. 2009. Does roughening of rock-fluid-rock interfaces emerge from a stress-induced instability? *The European Physical Journal B - Condensed Matter and Complex Systems* 67(1), 121-131.
- Bretz, J. H. 1940. Solution cavities in the Joliet limestone of northeastern Illinois. *Journal of Geology* 48(4), 337-384.
- Buxton, T. M. & Sibley, D. F. 1981. Pressure Solution Features in a Shallow Buried Limestone. *Journal of Sedimentary Petrology* 51(1), 19-26.
- Drummond, C. N. & Sexton, D. N. 1998. Fractal structure of stylolites. *Journal of Sedimentary Research* 68(1), 8-10.

- Dunnington, H. V. 1954. Stylolite development post-dates rock induration. *Journal of sedimentary Petrology* 24(1), 27-49.
- Dunnington, H. V. 1967. Aspects of diagenesis and shape change in stylolitic limestone reservoirs.
- Fletcher, R. C. & Pollard, D. D. 1981. Anticrack model for pressure solution surfaces. *Geology* 9(9), 419-424.
- Fletcher, R. C. & Merino, E. 2001. Mineral growth in rocks: Kinetic-rheological models of replacement, vein formation, and syntectonic crystallization. *Geochimica Et Cosmochimica Acta* 65(21), 3733-3748.
- Gal, D. & Nur, A. 1998. Elastic strain energy as a control in the evolution of asymmetric pressure-solution contacts. *Geology* 26(7), 663-665.
- Gal, D., Nur, A. & Aharonov, E. 1998. Stability analysis of a pressure-solution surface. *Geophysical Research Letters* 25(8), 1237-1240.
- Gratier, J. P., Muquet, L., Hassani, R. & Renard, F. 2005. Experimental microstylolites in quartz and modeled application to natural stylolitic structures. *Journal of Structural Geology* 27(1), 89-100.
- Guzzetta, G. 1984. Kinematics of Stylolite Formation and Physics of the Pressure-Solution Process. *Tectonophysics* 101(3-4), 383-394.
- Heald, M. T. 1955. Stylolites in Sandstones. *Journal of Geology* 63(2), 101-114.
- Karcz, Z. & Scholz, C. H. 2003. The fractal geometry of some stylolites from the Calcare Massiccio Formation, Italy. *Journal of Structural Geology* 25(8), 1301-1316.
- Katsman, R. & Aharonov, E. 2006. A study of compaction bands originating from cracks, notches, and compacted defects. *Journal of Structural Geology* 28(3), 508-518.
- Koehn, D., Renard, F., Toussaint, R. & Passchier, C. W. 2007. Growth of stylolite teeth patterns depending on normal stress and finite compaction. *Earth and Planetary Science Letters* 257(3-4), 582-595.
- Lind, I. L. 1993. Stylolites in chalk from Leg 130, Ontong Java Plateau. In: *Proceedings of the Ocean Drilling Program; Ontong Java Plateau, covering Leg 130 of the cruises of the drilling vessel JOIDES Resolution, Apra Harbor, Guam, to Apra Harbor, Guam, Sites 805-807, 18 January-26 March 1990.* (edited by Berger, W. H., Kroenke, L. W. & Mayer, L. A.). *Proceedings of the Ocean Drilling Program Scientific Results 130.* Texas A & M University, Ocean Drilling Program College Station, TX, United States, 445-451.
- Merino, E. 1992. Self-organization in stylolites. *American Scientist* 80(5), 466.
- Merino, E., Calas, A. & Fletcher, R. C. 2006. Genesis of self-organized zebra textures in burial dolomites: Displacive veins, induced stress, and dolomitization. *Geologica Acta* 4(3), 383-393.
- Park, W. C. & Schot, E. H. 1968. Stylolites: their nature and origin. *Journal of sedimentary Petrology* 38(1), 175-191.
- Railsback, B. L. & Andrews, L. M. 1995. Tectonic stylolites in the 'undeformed' Cumberland Plateau of southern Tennessee. *Journal of Structural Geology* 17(6), 911-915.

- 
- Railsback, L. B. 1993. Lithologic Controls on Morphology of Pressure-Dissolution Surfaces (Stylolites and Dissolution Seams) in Paleozoic Carbonate Rocks from the Mideastern United-States. *Journal of Sedimentary Research* 63(3), 513-522.
- Railsback, L. B. 1998. Evaluation of spacing of stylolites and its implications for self-organizations of pressure dissolution. *Journal of Sedimentary Research* 68(1), 2-7.
- Renard, F., Schmittbuhl, J., Gratier, J. P., Meakin, P. & Merino, E. 2004. Three-dimensional roughness of stylolites in limestones. *Journal of Geophysical Research-Solid Earth* 109(B3), -.
- Rutter, E. H. 1983. Pressure solution in nature, theory and experiment. *Journal of the Geological Society of London* 140(5), 725-740.
- Schmittbuhl, J., Renard, F., Gratier, J. P. & Toussaint, R. 2004. Roughness of stylolites: Implications of 3D high resolution topography measurements. *Physical Review Letters* 93(23), -.
- Simon, J. L. 2007. Analysis of solution lineations in pebbles: Kinematical vs. dynamical approaches. *Tectonophysics* 445(3-4), 337-352.
- Sorby, H. C. 1863. On the direct correlation of mechanical and chemical forces. *Proc. R. Soc. London* 12, 583-600.
- Stockdale, P. B. 1922. Stylolites: their nature and origin. *Indiana University Studies* 9, 1-97.
- Tada, R. & Siever, R. 1989. Pressure Solution during Diagenesis. *Annual Review of Earth and Planetary Sciences* 17, 89-118.



## 2. Stress sensitivity of stylolite morphology

### Abstract

Stylolites are rough surfaces that form by localized stress-induced dissolution. Using a set of limestone rock samples collected at different depths from a vertical section in Cirque de Navacelles (France), we study the influence of the lithostatic stress on the stylolites morphology on the basis of a recent morphogenesis model. We measured the roughness of a series of bedding-parallel stylolites and show that their morphology exhibits a scaling invariance with two self-affine scaling regimes separated by a crossover-length ( $L$ ) at the millimeter scale consistent with previous studies. The importance of the present contribution is to estimate the stylolite formation stress  $\sigma$  from the sample position in the stratigraphic series and compare it to the crossover-length  $L$  using the expected relationship:  $L \sim \sigma^{-2}$ . We obtained a successful prediction of the crossover behavior and reasonable absolute stress magnitude estimates using relevant parameters: depth of stylolite formation between 300 to 600 m with corresponding normal stress in the range of 10-18 MPa. Accordingly, the stylolite morphology contains a signature of the stress field during formation and we thus suggest that stylolites could be used as paleo-stress gauges of deformation processes in the upper crust.

*(\*) This chapter was published as:*

*Ebner, M., Koehn, D., Toussaint, R., Renard, F. & Schmittbuhl, J. 2009. Stress sensitivity of stylolite morphology. Earth and Planetary Science Letters 277(3-4), 394-398.*

### 2.1. Introduction

Stylolites are rough paired surfaces (as illustrated in Fig. 2.1 A), mainly observed in monomineralic sedimentary rocks. The fact that stylolites can be found in a variety of rocks and display a wide range of morphologies, even within a single outcrop, makes comparison and description of natural stylolites a difficult task (Park and Schot, 1968). Early classifications were mainly based on qualitative parameters such as the visual appearance of the interface and the orientation with respect to the bedding (Park and Schot, 1968; Guzzetta, 1984). Moreover, the necessary overburden for the formation of bedding-parallel stylolites is still debated: up to 800-1000 m (e.g. Railsback, 1993) whereas other studies (Tada and Siever, 1989 and references cited therein) report depths as shallow as 90 m for the onset of stylolitization. Stylolites form by localized stress induced dissolution (e.g. Stockdale, 1922; Dunnington, 1954; Rutter, 1983). They reflect important diagenetic processes like local mass transfer, compaction, and porosity reduction in sedimentary basins (e.g. Tada and Siever, 1989). They are often used to estimate the amount

of dissolved material in the rock (Tada and Siever, 1989), and therefore the total amount of deformation. The long axis of stylolite teeth-like patterns (Fig. 2.1) is also commonly used to decipher the largest principal compressive stress direction based on field observations (Petit and Mattauer, 1995; Ebner and Grasemann, 2006).

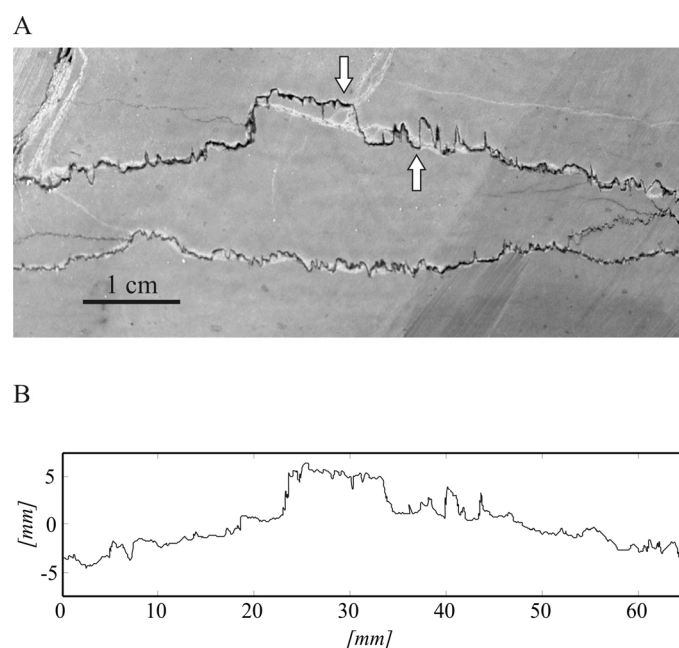


**Figure 2.1** Bedding-parallel stylolite from Cirque de Navacelles (southern France). **(A)** Plane section of a sample is cut perpendicular to the mean stylolitic plane. Arrow indicates “teeth-like” structures that are oriented parallel to the principal stress direction. **(B)** 1D roughness of the stylolite shown in A after removal of overhangs and linear trend. This data was used to calculate the scaling properties of the roughness.

Modeling of stylolite morphogenesis is a challenging task (Gal et al., 1998). When their shape is analyzed at large scales and reduced to a flat penny-shape disk, they have been thought to propagate as anticracks (Fletcher and Pollard, 1981). A significant step in stylolite morphogenesis modeling has been obtained from extended roughness measurements in particular 3D profiling of open stylolites. These data have allowed quantitative approaches based on fractal analysis tools (Drummond and Sexton, 1998) and demonstrated fractal scaling invariance over several orders of magnitude of stylolite roughness (Renard et al., 2004; Schmittbuhl et al., 2004; Gratier et al., 2005; Karcz and Scholz, 2003; Brouste et al., 2007). In addition Schmittbuhl et al. (2004) and Renard et al. (2004) observed the existence of a crossover-length ( $L$ ) that separates two scaling regimes with different roughness exponents for small and large scales. These scaling regimes are consistent with an interface morphogenesis model (Schmittbuhl et al., 2004; Renard et al., 2004) that describes the growth of a stylolite surface as a competition between two stabilizing forces: long range elastic fluctuations and local surface tension, and a destabilizing force due to the presence of heterogeneities in the material. These heterogeneities are thought to be caused by mineral impurities that induce local fluctuations of the elastic moduli. According to this model, the roughening destabilization is induced by the heterogeneities in the material, whereas surface tension balances the roughening process on small and elastic energies on large scales. The key point in the modeling is the prediction of the crossover-length  $L$ , i.e. a property of the present stylolite geometry, as a function of the stress field during



stylolite formation, i.e. the driving paleo-stress. A numerical check of this modeling was proposed by Koehn et al. (2007), which verified the basic assumptions of interrelation between stress orientation and the orientation of stylolite teeth. The motivation of the present work is to examine the link between stylolite morphology and stress magnitude, based on a data set of natural stylolites for which the stress magnitude can be estimated.

## 2.2. Stylolite data-set, roughness measurements and analysis

We studied a set of 14 bedding-parallel stylolites from Cirque de Navacelles (southern France), where a 300 m section of flat-lying upper Jurassic limestone crops out (e.g. Bodou, 1976). The investigated succession is an external shelf deposit of the Vocontian Basin that consists mainly of fine-grained (5-40  $\mu\text{m}$ ) mudstones and wackestones. The top 100 m is made up of massive Kimmeridgian limestones, whereas the lower 200 m part contains well-bedded Oxfordian mudstones with higher marl content and a slight secondary dolomitization (Bodou, 1976). The main tectonic overprint in this area is caused by Eocene roughly N-S directed compression from the Pyrenean (e.g. Rispoli, 1981; Petit and Mattauer, 1995). This tectonic phase reactivated subvertical fractures, which trend NE-SW and show a left-lateral displacement. The main tectonic structures are exposed south of the sampling area, but a set of approximately E-W striking vertical stylolites that accompany this tectonic event can be found in the investigated area (Petit and Mattauer, 1995). Such vertical tectonic stylolites were not used or investigated in this study.

The investigated samples were all collected along fresh road-cuts. Only closed interfaces were considered for sampling to avoid overprint due to weathering. In addition, we collected only macroscopically visible stylolites in calcitic limestones for the present study. The samples are very fine-grained mudstones and, for all samples, the porosity is secondary and amounts to less than 10 %, in line with high seismic velocities measured (see later). Microstructural investigation of the samples showed that bioclast content is below 5-10 % and that clasts do not pin the surface, i.e. do not register in the roughness. The bedding parallel stylolites did not initiate along preexisting planes of anisotropy, such as bedding planes, but originated along sites of stress concentration (e.g. clay particles). Microstylolites observed in thin-section frequently revealed tapered terminations as predicted by the anticrack theory (Fletcher and Pollard, 1981). Insoluble materials, including fine-grained clay minerals that have accumulated along the stylolitic interface do not exceed 0.5 mm in thickness (Bodou, 1976). The samples were collected along the vertical profile to systematically investigate the influence of lithostatic stress on stylolite roughness.

Since mechanical opening along the stylolitic interface was not possible for most of the samples, we could not investigate the stylolite surface morphology with a profiler (e.g. Renard et al., 2004). Therefore we examined 2D slabs that displayed the stylolite seam.

All oriented specimens were cut normal to the main stylolitic plane to contain the principal stress direction. Each slab was imaged with an SLR camera (sample size along the cut surface is 10-30 cm with a

pixel resolution of 35  $\mu\text{m}$ ) without further treatment (see Fig. 2.1). The signals were extracted from these images using two different methods. In the first method we manually digitized the images using standard drawing software (CorelDraw©). To check the consistency of our method and to avoid bias from human input we used a second method, for which we used simple image analysis tools. For that purpose, we clipped the appropriate value range (i.e. the stylolite) from the histogram of the grayscale image and converted the clipped part to a binary image. This image contains the trace of the stylolite from which the boundary pixels were extracted for further treatment.

The raw 1-D profiles (Fig. 2.1 B) were pre-treated by removing the overhangs to get single valued functions down to the inverse of the Nyquist-frequency (i.e. of twice the pixel size of the digital images). This binning of the raw data was executed using an algorithm that extracts the topmost pixel of the stylolite signal along each vertical column of the image. A reference frame has been defined for each profile, by adjusting its horizontal (x) axis to the global linear trend i.e. a regression over the profile, and the vertical (z) axis is set to have zero mean height. We verified that the signal derived from our stylolite cross-sections shows a scaling behavior similar to extended measurements from 3D topographies by taking side pictures of “opened” stylolites not used in this study, applying the same image extraction technique as described above and comparing the outcome to profiler measurements as suggested by Schmittbuhl et al., (2004).

Results from Schmittbuhl et al. (2004) and Renard et al. (2004) show that stylolite roughness exhibits complex self-affine scaling invariance. A self-affine rough surface is characterized statistically by the fact that points along the surface separated by a distance  $\Delta x$  from each other are typically distant in the direction transverse to the surface by  $\Delta b \approx \Delta x^H$ , where  $H$  is the roughness or Hurst exponent. Indeed two self-affine regimes are observed on stylolites which can be summed up for the average description of the height difference  $h$  of points along the surface separated by a distance  $\Delta x$  as:

$$h(\Delta x) \approx A \Delta x^{H_s} g(\Delta x / L) \quad \text{with} \quad g(u) = \begin{cases} u^0 & \text{if } u \ll 1 \\ u^{H_L - H_s} & \text{if } u \gg 1 \end{cases} \quad (2.1)$$

where  $A$  is a scaling factor  $g$  is a scaling function and  $u$  is the ratio  $\Delta x/L$  with  $L$  being a crossover-length.  $H_s, H_L$  correspond to the roughness exponents for small and large scales, respectively.

We calculated the Fourier power spectrum  $P$  of the stylolite profiles as a function of the wave number  $k$  (Renard et al., 2004; Schmittbuhl et al., 2004) (see Fig. 2.2 A). The power spectrum actually exhibits two power law regimes separated by a crossover at a wave number  $k_L \approx 1 \text{ mm}^{-1}$ . Knowing that the power spectrum of a self-affine profile behaves as:  $P(k) \sim k^{-1-2H}$ , we can estimate both roughness exponents from the asymptotic behaviors at small and large scales. To verify our results, we used a second independent signal processing technique, the average wavelet coefficient method (AWC), with Daubechies D4 wavelets (Simonsen et al., 1998). The wavelet spectrum of a self-affine function behaves as a power law with an exponent equal to  $1/2+H$  (see Fig. 2.2 B). Using both methods, our results confirm the presence of two scaling regimes with  $H_s \sim 1.1$  and  $H_L \sim 0.5$  for small and large length scales respectively.

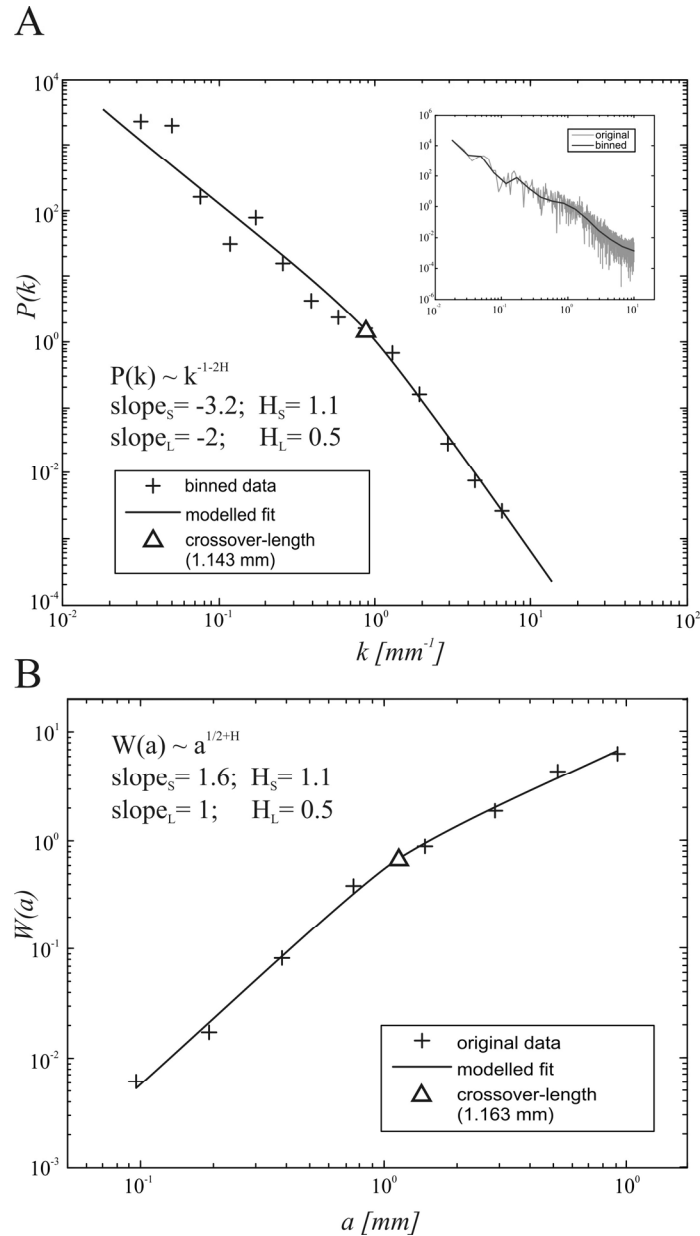


**Figure 2.2** Scaling of Fourier power and averaged wavelet spectra from 1D stylolite profiles. **(A)** Fourier power spectrum (inset) of the stylolite shown in (A) and logarithmically binned spectrum (crosses) used for nonlinear least square fitting (solid line) with  $L$  indicated by a triangle;  $H_S$  and  $H_L$  denote the roughness exponents of the signal. **(B)** Averaged wavelet spectrum (AWC) of the stylolite (crosses) of (A) with modeled fit (solid line) and  $L$  (triangle). Both independent methods reveal similar values for the crossover-length and roughness exponents of individual samples.

A sensitive task is to estimate precisely the crossover-length scale  $L$ . For this, we assumed a linear-by-parts fit of the Fourier or wavelet spectra in the logarithmic space, with a crossover function to change from the small scale branch of the scaling law to the large scale one: More precisely, noting in Fourier space,  $x = \ln(k)$  and  $f(x) = \ln[P(k)]$  with  $P(k)$  the power spectrum, or alternatively in wavelet space,  $x = \ln(a)$  where  $a$  is the scale parameter, and  $f(x) = \ln[W(a)]$  with  $W(a)$  the associated average wavelet coefficient, we fit these spectra to the following model:

$$f(x) = (a_L x + m_L)(1 - w(x)) + (a_S x + m_S)w(x) \quad \text{and} \quad w(x) = \frac{(\tanh(x + L) + 1)}{2} \quad (2.2)$$

where  $a_{L,S}$  are the exponents of the scaling function for large and small scales (i.e.  $a_{L,S} = -1-2H_{L,S}$  in Fourier, and  $a_{L,S} = 0.5+H_{L,S}$  for the wavelet spectrum),  $m_{L,S}$  are the corresponding intercepts with the ordinate and  $w(x)$  is the weighting function. We fixed the roughness exponents and searched using a least square algorithm the best estimates of  $L$  and  $m_{L,S}$ . In addition we verified that the obtained parameters did not vary along the interface by performing the scaling analysis over independent parts of the same 1D signal. This procedure allowed a robust investigation of the data. Note that to model the data with an equal importance for the large and small scale, we resample the power spectra with a logarithmic binning, i.e. to get a constant density of data points over the complete spectrum in logarithmic representation.

### 2.3. Results

We calculated the crossover-lengths  $L$  for all samples from Fourier and wavelet spectra. Figure 2.3 A shows the correlation between  $L$  and the relative vertical position of the sample in the stratigraphic series. We observe that  $L$  decreases from  $\sim 2.1$  mm near the top (525 Meters Above Sea level – MAS) to  $\sim 0.7$  mm at the bottom of the series (250m – MAS), which corresponds to a factor 3 for almost 300m of relative depth. The crossover-length for sample N2 is clearly off the trend (see Fig. 2.3 A) for both methods but the respective roughness exponents are similar compared to the other samples (Fig. 2.3 B). A way to check the consistency of our crossover length-scale estimate is to collapse all data on a single curve (i. e. a uniform scaling function) using  $L$  to scale the horizontal distance along the sample and the vertical magnitude of the roughness for all samples (see Fig. 2.3 B for the collapse of the wavelet spectra) as proposed by Renard et al. (2004). The accordance of the collapse is a measurement for the quality of the overall fit of  $L$  for all samples. Indeed, a good data collapse should demonstrate that the crossover-lengths used to normalize the data are correct for individual samples. We however notice a systematic offset of  $\sim 0.13$  mm between estimates of  $L$  from the Fourier spectra and that from the wavelet spectra. This systematic offset is of the same order of magnitude as the precision of measurement of  $L$  as indicated in Fig. 2.3 A. Error analysis performed by Schmittbuhl et al. (1995) revealed that the Fourier analysis is more sensitive to signal length and self affinity of the signal compared to the AWC analysis (Simonsen et al., 1998) when using synthetic signals with known properties. Hence in the following we correct the Fourier estimates by adding this offset to all the values.

Schmittbuhl et al. (2004) and Renard et al. (2004) established from first principles of mechanics and thermodynamics a model for stylolite growth under the form of a stochastic partial differential equation (a generalized Langevin equation), which successfully described stylolite growth as a competition between material disorder and stabilizing forces such as surface tension and elastic interactions.

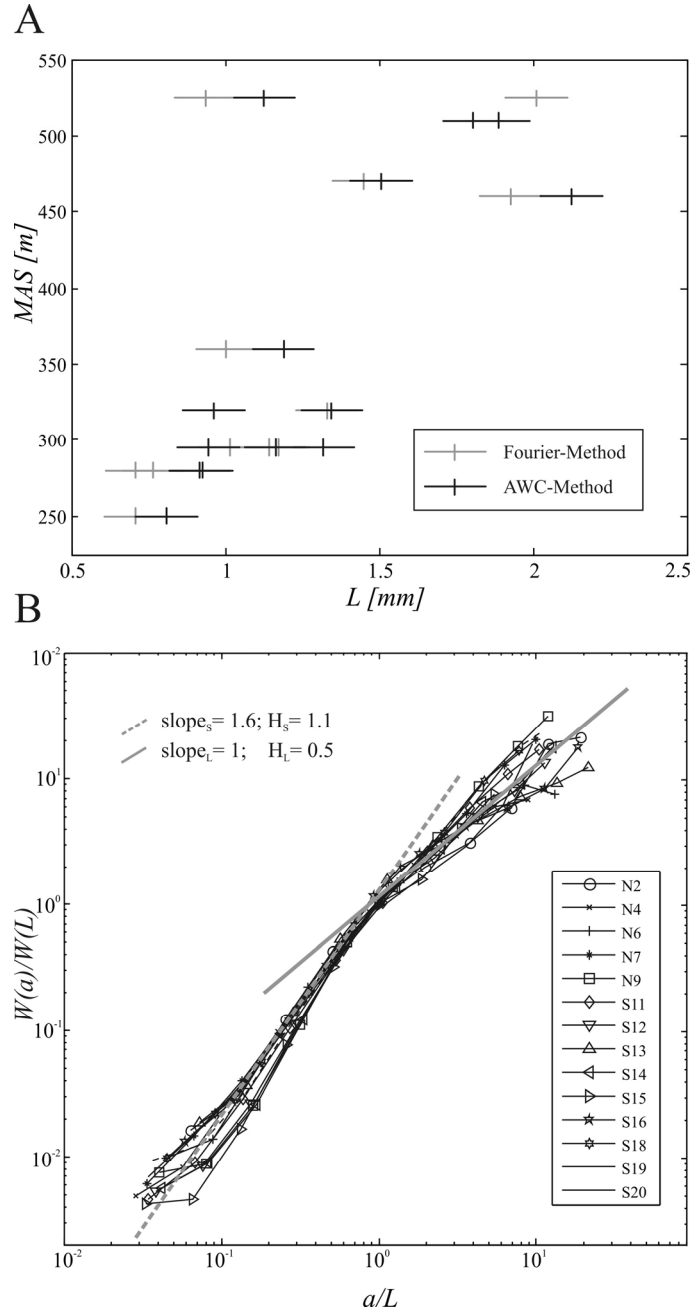


**Figure 2.3** Crossover-length and scaling data for all samples. **(A)** Relative sample position MAS (=meters above sea-level) versus  $L$  for the whole stylolite data set (error-bars indicate the precision of measurements). Notice the increase in  $L$  with the sample vertical position in the profile. **(B)** Data collapse for the scaling functions of all samples for the AWC method.  $L$  is used to normalize the scaling functions demonstrating that there is one scaling function common to all stylolites investigated.

Hence a possible link between  $L$ , surface tension and the state of stress during stylolite formation has been proposed by Schmittbuhl et al. (2004):

$$L = \frac{\gamma E}{\beta \sigma_m \sigma_d}, \quad (2.3)$$

where  $E$  is the Young's Modulus,  $\gamma$  is the solid-fluid interfacial energy,  $\beta = \nu(1-2\nu)/\pi$  is a dimensionless constant with  $\nu$  the Poisson's ratio,  $\sigma_m$  and  $\sigma_d$ , are the mean and differential stresses respectively. For the

Cirque de Navacelles stylolites, we assumed that the main principal stress is vertical ( $\sigma_{zz}$ ), whereas both horizontal stresses are equal and smaller than the vertical stress component. Accordingly,  $\sigma_m = 1/3(\sigma_{zz} + 2\sigma_{xx})$  and  $\sigma_d = \sigma_{zz} - \sigma_{xx}$ . Finally, we consider the strain to be uniaxial (i.e. zero horizontal displacement), which is a reasonable simplification for the early stages of sedimentation in most basins. This allowed us to relate the horizontal and vertical components of stress ( $\sigma_{xx} = \sigma_{yy} = [\nu/(1-\nu)] \sigma_{zz}$ ). Expressing the mean and differential stresses as a function of the vertical principal normal stress ( $\sigma_{zz}$ ) gives:  $\sigma_m \sigma_d = a \sigma_{zz}^2$  with  $a = 1/3[(1+\nu)/(1-\nu)][(1-2\nu)/1-\nu]$ . Introducing these estimates in Equation 2.3 provides a relationship between the crossover  $L$ , the surface tension and the principal normal stress component  $\sigma_{zz}$ :

$$L = \frac{\gamma E}{\beta} \cdot \frac{1}{\alpha \sigma_{zz}^2}, \quad (2.4)$$

if the physical parameters are known. For the surface free energy, we adopted a typical value of a calcite-water interface in limestones,  $\gamma = 0.23 \text{ J/m}^2$  (Wright et al., 2001). We assumed a Poisson's ratio  $\nu = 0.25 \pm 0.05$  (Clark, 1966).

The last step is to measure the vertical stress independently of Equation 2.4. This is obtained assuming that the vertical stress equals the weight of overburden, i.e. lithostatic stress:  $\sigma_{zz} = \rho g z$  with  $\rho$  is the rock-density;  $g$  is the acceleration of gravity ( $9.81 \text{ m/s}^2$ ), and  $z$  the depth. We measured a constant bulk density from our samples of:  $\rho = 2.7 \text{ g/cm}^3$ .

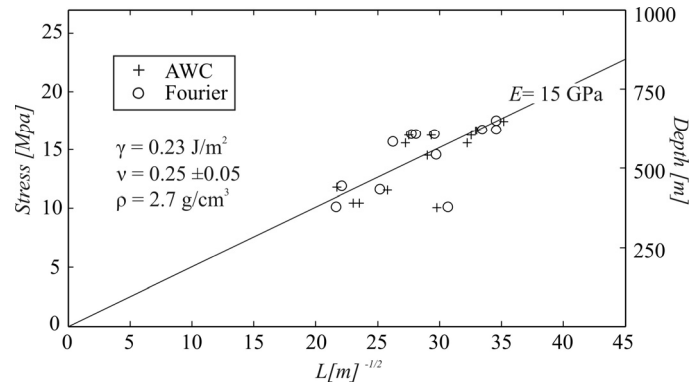


**Figure 2.4** Plot of a principal normal stress as a function of  $L^{-1/2}$ . The plot illustrates the linear dependence of the field data and demonstrates that a linear trend for both scaling-methods confirms the analytical solution of Schmittbuhl et al., (2004). The slope of the linear fit of the natural datasets (solid line) correspond to a Young's modulus of 15 GPa for a given set of material properties ( $\rho, \gamma, \nu$ ) calculated from Eq. 2.4.

We rearranged Equation 2.4 in a way that stress is plotted as a function of  $L^{-1/2}$  in order to obtain a linear relationship (Fig. 2.4). That this plot exhibits such a linear behavior demonstrates the consistency of our model. The plot shown in Figure 2.4 suggests that the roughness of bedding-parallel stylolites contains a significant signature of the stress-field during formation of the stylolites. We found that the Young's modulus was  $E=15 \text{ GPa}$ , i.e. the regression line through the data points, which is in line with values measured on limestones (Clark, 1966). Our dataset indicates that the thickness of the overlying rock mass was  $\sim 300 \text{ m}$  (which can be read from the representation in Figure 2.4), which corresponds to  $\sim 10 \text{ MPa}$

and  $\sim 18$  MPa of vertical normal stress at the top and bottom of the investigated section, respectively, applying the stated assumptions. The related horizontal normal stresses were then  $\sim 4$  MPa and  $\sim 6.5$  MPa.

## 2.4. Discussion & Conclusions

To characterize the present material constants, we determined the elastic parameters for two characteristic rock samples using seismic wave velocity measurements under laboratory conditions. From the P and S-wave velocities we calculated the elastic parameters (Jaeger et al., 2007) of two representative samples (ST-17:  $E = 86$  GPa,  $\nu = 0.09$ ; N-6:  $E = 97$  GPa,  $\nu = 0.05$ ). The elastic parameters are clearly different from the values plotted in Figure 2.4. Indeed, during stylolite formation, the rock was softer and the Young's modulus and Poisson's ratio might have been different than for a compacted rock. Given that carbonates are prone to diagenetic alterations that may modify the porosity and thus seismic velocities, especially in the vicinity of a stylolite (Raynaud and Carrio-Schaffhauser, 1992), the elastic parameters derived from our samples may be strongly altered (Anselmetti and Eberli, 1993). Accordingly mechanico-chemical tests to reproduce the observed stylolites using present rock samples would be inappropriate.

Equation 2.4 shows that the crossover length is a function of the elastic properties, which are strongly influenced by the rock porosity (e.g. Eberli et al., 2003). It is likely that the elastic parameters evolve with the compaction process, consequently the elastic parameters may change with depth. We do not think that our observed trend in the stylolite crossover is a function of varying elastic parameters. In order to explain such a smooth variation of the crossover over the whole profile by a variation of one of the parameters (Young's modulus, porosity or density) would require that these parameters vary smoothly and linearly with depth, which is not very often the case (compare Eberli et al., 2003). For example a decrease in porosity down-section, i.e. an increase in the Young's modulus, would result in a non-linear increase of the crossover-length with depth. This seems to be a second order effect since our data are consistent with a linear relationship (Eq. 2.4) and more importantly a decrease of  $L$  with depth.

Our assumption that elastic parameters are constant throughout the profile implies that the kinetics of the roughening must be fast relative to the progressive burial of rocks so that the stylolite roughness can re-equilibrate with depth. Schmittbuhl et al. (2004) demonstrated that the time to saturate the roughness and thus develop self-affine scaling invariance and a respective crossover-length is in the order of 200 years. Even high accumulation rates in platform carbonates usually do not exceed  $\sim 40$  m/my i.e. less than 1 cm in 200 years (e.g. McNeill, 2005), which would easily allow the re-equilibration of the roughness. Under the assumption that the timescale for the roughening would be much larger than that for a change in the accumulation of the burial load, stylolites would record the terminal stresses before they become inactive. We conclude that our constant Young's modulus assumption seems to fit the data over the investigated range but further investigations are necessary that span greater differences in formation depth. It has to be added that the measured vertical distances between the samples in the section were probably larger during formation of the stylolites due to ongoing compaction of the rock-

mass. This effect would result in a telescoping of the data along the ordinate of Figure 2.3 A and an opposite effect would be noticed in Figure 2.4, i.e. the slope through the data would be steeper.

Another assumption used in this study is that all stylolites formed more or less simultaneously, which is indeed questionable. However, if the stylolites formed one after the other when their host rock reached a certain depth in the basin, they would not reveal a difference in crossover-lengths.

It can be further noticed that another petrographical factor, the transition from massif to bedded mudstone layers, does not register in the observed crossovers. We are therefore confident that these large scale heterogeneities played, if any, a negligible role in the scaling of the crossover-length in the investigated section. Additional analysis is necessary to investigate the influence of different lithologies from the same structural level since we only investigated very homogeneous mudstone along the section. In summary we suggest that the systematic variation of the crossover-length in the investigated section is mainly a function of stress. Our results are in line with differential stress/depth relations obtained from in-situ stress measurements and comparable to other paleo-piezometers e.g. calcite twinning (Lacombe, 2007 and references cited therein).

We propose that bedding-parallel stylolites can be considered as quantitative stress gauges because their roughness depicts the stress field during formation. Investigation of a set of samples from different depth allows determining their depth of formation and the absolute stress magnitudes if the assumptions stated above can be adopted.

In this contribution we investigated bedding-parallel stylolites that formed due to lithostatic overburden. This setting allows simplifications that are not valid for stylolites that formed in response to a stress field that has its largest principal stress direction oblique to the Earth's surface. Assessment of the stress field around vertical stylolites needs more prerequisites e.g. a test if the scaling is isotropic as in the case of bedding-parallel stylolites and, further, needs good depth constraints e.g. from independent methods or under favorable circumstances from horizontal stylolites with the method proposed here. Knowledge of these quantities would enable us to investigate stresses around vertical stylolites and thus magnitudes of tectonic loading in the Earth's crust.

## 2.5. References

- Anselmetti, F.S., Eberli, G.P., 1993. Controls on Sonic Velocity in Carbonates. *Pure Appl. Geophys.* 141 (2-4), 287-323.
- Bodou, P., 1976. Importance of the stylolitic joints in the compaction of limestones. *Bull. Centre Rech. Pau - SNPA* 10, 627-644.
- Brouste, A., Renard, F., Gratier, J.P., Schmittbuhl, J., 2007. Variety of stylolites' morphologies and statistical characterization of the amount of heterogeneities in the rock. *J. Struct. Geol.* 29 (3), 422-434.
- Clark, S.P.J., 1966. *Handbook of Physical Constants*. Geological Society of New York, New York.
- Drummond, C.N., Sexton, D.N., 1998. Fractal structure of stylolites. *J. Sediment. Res.* 68 (1), 8-10.



- Dunnington, H.V., 1954. Stylolite development post-dates rock induration. *J. Sediment. Petrol.* 24 (1), 27-49.
- Eberli, G.P., Baechle, G.T., Anselmetti, F.S., Incze, M.L., 2003. Factors controlling elastic properties in carbonate sediments and rocks. *The Leading Edge* 22, 654-660.
- Ebner, M., Grasemann, B., 2006. Divergent and convergent non-isochoric deformation. *J. Struct. Geol.* 28 (10), 1725-1733.
- Fletcher, R.C., Pollard D.D., 1981. Anticrack model for pressure solution surfaces. *Geology* 9 (9), 419-424.
- Gal, D., Nur, A., Aharonov, E., 1998. Stability analysis of a pressuresolution surface. *Geophys. Res. Lett.* 25 (8), 1237– 1240.
- Gratier, J.P., Muquet, L., Hassani, R., Renard, F., 2005. Experimental microstylolites in quartz and modeled application to natural stylolitic structures. *J. Struct. Geol.* 27 (1), 89-100.
- Guzzetta, G. 1984. Kinematics of Stylolite Formation and Physics of the Pressure-Solution Process. *Tectonophysics* 101, 383-394.
- Jaeger, J.C., Cook, N.G.W., Zimmermann, R.W., 2007. *Fundamentals of rock mechanics*. Blackwell Publishing Ltd, Oxford.
- Karcz, Z., Scholz, C.H., 2003. The fractal geometry of some stylolites from the Calcare Massiccio Formation, Italy. *J. Struct. Geol.* (8), 1301-1316.
- Koehn, D., Renard, F., Toussaint, R., Passchier, C.W., 2007. Growth of stylolite teeth patterns depending on normal stress and finite compaction. *Earth Planet. Sc. Lett.* 257 (3-4), 582-595.
- Lacombe, O., 2007. Comparison of paleostress magnitudes from calcite twins with contemporary stress magnitudes and frictional sliding criteria in the continental crust: Mechanical implications. *J. Struct. Geol.* 29 (1), 86-99.
- McNeill, D.F., 2005. Accumulation rates from well-dated late Neogene carbonate platforms and margins. *Sediment. Geol.* 175 (1-4) 73-87.
- Park, W.C., Schot, E.H., 1968. Stylolites: their nature and origin. *J. Sediment. Petrol.* 38 (1), 175-191.
- Petit, J.P., Mattauer M., 1995. Palaeostress superimposition deduced from mesoscale structures in limestone: the Matelles exposure, Languedoc, France. *J. Struct. Geol.* 17 (2), 245-256.
- Railsback, L.B., 1993. Lithologic Controls on Morphology of Pressure-Dissolution Surfaces (Stylolites and Dissolution Seams) in Paleozoic Carbonate Rocks from the Mideastern United-States. *J. Sediment. Petrol.* 63 (3), 513-522.
- Raynaud, S., Carrio-Schaffhauser, E., 1992. Rock matrix structures in a zone influenced by a stylolite. *J. Struct. Geol.* 14 (8-9), 973-980.
- Renard, F., Schmittbuhl, J., Gratier, J.P., Meakin, P., Merino, E., 2004. Three-dimensional roughness of stylolites in limestones. *J. Geophys. Res.-Sol. Ea.* 109 (B03209), doi:10.1029/2003JB002555.
- Rispoli, R., 1981. Stress fields about strike-slip faults inferred from stylolites and tension gashes. *Tectonophysics* 75, 29-36.

- 
- Rutter, E.H., 1983. Pressure solution in nature, theory and experiment. *J. Geol. Soc. London.* 140 (5), 725-740.
- Schmittbuhl, J., Vilotte, J.P., Roux, S., 1995. Reliability of Self-Affine Measurements. *Phys. Rev. E* 58 (1), 131-147.
- Schmittbuhl, J., Renard, F., Gratier, J.P., Toussaint, R., 2004. Roughness of stylolites: Implications of 3D high resolution topography measurements. *Phys. Rev. Lett.* 93 (238501), doi:10.1103/PhysRevLett.93.238501.
- Simonsen, I., Hansen, A., Nes, O.M., 1998. Determination of the Hurst exponent by use of wavelet transforms. *Phys. Rev. E* 58 (3), 2779-2787.
- Stockdale, P.B., 1922. Stylolites: their nature and origin. *Indiana University Studies* 9, 1-97.
- Tada, R., Siever, R., 1989. Pressure Solution during Diagenesis. *Annual Review of Earth and Planetary Sciences* 17, 89-118.
- Wright, K., Cygan, R.T., Slater B., 2001. Structure of the  $(10\bar{1})$  surfaces of calcite, dolomite and magnesite under wet and dry conditions. *Phys. Chem. Chem. Phys.* 3 (5), 839-844.

### 3. Anisotropic scaling of tectonic stylolites: a fossilized signature of the stress field?

#### Abstract

Vertical stylolites are pressure solution features, which are considered to be caused by horizontal tectonic loading with the largest principal compressive stress being (sub) parallel to the earth surface. In the present study we analyze the roughness of such tectonic stylolites from two different tectonic settings in southern Germany and north-eastern Spain aiming to investigate their scaling properties with respect to the stress during formation. High resolution laser profilometry has been carried out on opened stylolite surfaces of nine samples. These datasets were then analyzed using 1D and 2D Fourier power spectral approaches. We found that tectonic stylolites show two self-affine scaling regimes separated by a distinct crossover-length ( $L$ ), as known for bedding parallel stylolites. In addition tectonic stylolites exhibit a clear in-plane scaling anisotropy which modifies  $L$ . Since the largest and smallest crossover-lengths are always oriented with the sample vertical and horizontal directions (i.e.  $\sigma_2$  and  $\sigma_3$ ) and  $L$  is a function of the stress field during formation as analytically predicted we conclude that the scaling anisotropy of tectonic stylolites is a function of the stress field. Knowledge of this crossover-length anisotropy would enable the reconstruction of the full 3D stress tensor if independent constraints of the depth of formation can be obtained.

*(\*) This chapter is submitted to: Journal of Geophysical Research – Solid Earth*

*Ebner M., Toussaint R., Schmittbuhl J., Koehn D. & Bons P. (under review) Anisotropic scaling of tectonic stylolites: a fossilized signature of the stress field? Journal of Geophysical Research – Solid Earth*

#### 3.1. Introduction

The intriguing variety of pressure solution features and its wide-spread occurrence in monomineralic rock types provoked a continuous interest and attention in various geoscience disciplines over the past decades (Tada & Siever 1989). One of the most prominent and complex pressure solution features are stylolites, which are rough dissolution interfaces that can be found in a large variety of sedimentary rocks (Stockdale 1922, Dunnington 1954, Heald 1955, Park & Schot 1968, Buxton & Sibley 1981, Rutter 1983, Tada & Siever 1989, Railsback 1993). Until recently stylolite morphology has been described qualitatively by the use of a descriptive terminology, which grouped stylolites into generic classes. One classification uses the orientation of the stylolite plane relative to bedding. Bedding-parallel stylolites are supposed to

have formed due to the layer-normal overburden pressure, while tectonic stresses cause the formation of stylolites oblique or perpendicular to bedding (Park & Schot 1968, Railsback & Andrews 1995). A second classification is based on the orientation of the stylolite teeth relative to the stylolite plane. Here the term "stylolite" is used for teeth at a high angle to the plane, and 'slickolite' for dissolution surfaces where the teeth are distinctly oblique to the dissolution plane (Bretz 1940, Gratier et al. 2005, Simon 2007). Finally the shape of the characteristic teeth-like asperities and spikes along the interface has been used to characterize stylolites (Park & Schot 1968, Guzzetta 1984).

More recently, stylolites have been subjected to more rigorous quantitative analyses to characterise the roughness of the stylolite surface (Drummond & Sexton 1998, Karcz & Scholz 2003, Renard et al. 2004, Schmittbuhl et al. 2004, Gratier et al. 2005, Brouste et al. 2007, Koehn et al. 2007, Ebner et al. 2009a, Ebner et al. 2009b). It was demonstrated that the 1D stylolite roughness obeys a fractal scaling invariance (Drummond & Sexton 1998, Karcz & Scholz 2003). Investigation of the rough interface of opened stylolite surfaces by means of laser profilometry revealed that the stylolite morphology shows two self-affine scaling regimes with two distinct roughness exponents on their respective scales, which are separated by a characteristic crossover length at the millimeter scale (Renard et al. 2004, Schmittbuhl et al. 2004) for bedding parallel stylolites. Self-affine surfaces define a group of fractals, which remain statistically unchanged by the transform:  $\Delta x \rightarrow b \cdot \Delta x$ ,  $\Delta y \rightarrow b \cdot \Delta y$ ,  $\Delta z \rightarrow b^H \cdot \Delta z$ , where  $b$  is a transformation factor, which can take any real value and  $H$  is the Hurst or roughness exponent (Barabasi & Stanley 1995), which is a quantitative measure for the roughness of the signal.

Analytical and numerical investigations demonstrated that the growth of the stylolite roughness is induced by heterogeneities in the host rock that pin the interface and is slowed down by two stabilizing forces, the elastic and surface energies. The elastic energy dominates on larger scales and is represented by a small roughness exponent of 0.3 to 0.5 whereas the surface energy is dominant on small scales with a roughness exponent of about 1 (Renard et al. 2004, Schmittbuhl et al. 2004, Koehn et al. 2007). The characteristic crossover length ( $L$ ) that separates these two scaling regimes is a function of the principal normal stress (Renard et al. 2004, Schmittbuhl et al. 2004) on the interface of a sedimentary stylolite and was used by Ebner et al. (2009b) to successfully test the stress sensitivity of the stylolite morphology in the field. The 1D scaling of stylolites with two self-affine scaling invariance regimes can be described as the height difference  $h$  of points along the surface separated by a distance  $\Delta x$  as (Ebner et al. 2009b)

$$h(\Delta x) \approx A \Delta x^{H_s} g(\Delta x / L) \quad \text{with} \quad g(u) = \begin{cases} u^0 & \text{if } u \ll 1 \\ u^{H_L - H_s} & \text{if } u \gg 1 \end{cases} \quad (3.1)$$

where  $A$  is a scaling factor  $g$  is a scaling function and  $u$  is the ratio  $\Delta x/L$  with  $L$  being a crossover-length.  $H_s$ ,  $H_L$  correspond to the roughness exponents for small and large scales, respectively. Numerical simulations also demonstrate that the crossover-length is very robust with regard to the kind and amount of quenched noise (heterogeneities initially present) in the rock (Ebner et al. 2009a). Hence, the use of bedding parallel stylolites as a quantitative stress gauge under the assumption of uniaxial strain (zero

horizontal displacement) seems to be verified. Investigations of the surface morphology of bedding parallel stylolites showed that their scaling is isotropic within the plane defined by the stylolite (Renard et al. 2004, Schmittbuhl et al. 2004). This implies that an arbitrary section through the stylolite interface that contains the principal stress direction (i.e. normal to the plane) fully characterizes the complex self-affine roughness of bedding parallel stylolites.

Up to now no study has quantitatively investigated the 3D topography of tectonic stylolites, which formed due to (sub-)horizontal compression. Tectonic stylolites differ in two major characteristics from bedding parallel stylolites. First, the stress field during the formation of tectonic stylolites is non-isotropic i.e. the in-plane normal stresses differ (i.e.  $\sigma_{zz} > \sigma_{xx}$ ) whereas bedding parallel stylolites often have equal in-plane normal stresses  $\sigma_{xx} = \sigma_{yy}$  (Fig. 3.1). This would imply that the scaling of tectonic stylolites is not invariant within the plane, since the crossover-length should scale with the (non-isotropic) stress field as was shown analytically (Schmittbuhl et al. 2004). A second common feature of tectonic stylolites are oblique/tilted teeth with respect to the mean stylolite plane due to overprinting of pre-existing planes of anisotropy such as joints etc. Tilting of the teeth with respect to the stylolite plane also influences the morphology because it leads to the dominance of long grooves and ridges (Simon 2007). These features could lead to an anisotropic scaling of the stylolite interface in addition to variations of the in-plane stresses.

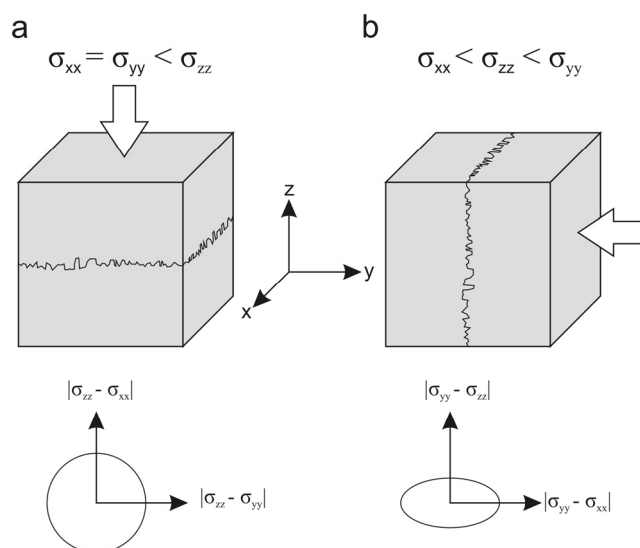


**Figure 3.1** Schematic drawing of the formation stress state for **(a)** bedding parallel and **(b)** tectonic stylolites. The largest compressive stress direction ( $\sigma_1$ ) is indicated by a white arrow. Below the sketch map an idealized graph of the in-plane differential stress plotted as a function of the orientation within the stylolite plane. For bedding parallel stylolites **(a)** the horizontal normal stresses are equal and thus the differential stress is equal in every direction. For tectonic stylolites **(b)** the in-plane normal stresses are dissimilar and  $\sigma_{zz}$  is generally larger than  $\sigma_{xx}$ . Thus the in-plane differential stress scales inversely with the magnitudes of the  $\sigma_{xx}$  and  $\sigma_{zz}$  directions having a maximum along the x-axis.

The present study investigates such tectonic stylolites. We mainly concentrate on the influence of (i) the orientation of the dissolution surface with respect to the displacement direction and (ii) the formation stress on the scaling properties of natural stylolites in limestones. To accomplish this task we use laser

profilometry data of opened interfaces of tectonic stylolites from flat lying Jurassic limestones of the Swabian Alb in southern Germany and from a Tertiary fold and thrust belt of the Iberian Chain of north-eastern Spain.

## 3.2. Geological setting

In the following section we give a brief introduction of the investigated field areas in southern Germany and north-eastern Spain, which both expose upper Jurassic limestones. The Swabian Alb of southern Germany form a region of flat-lying mainly marine Jurassic deposits (Geyer & Gwinner 1991). The studied sections are located 10 km south of the city of Tübingen and comprise upper Jurassic (Oxfordian to Kimmeridgian) limestones. The basal part of the sections (*UTM 32U; E 0515212 m; N 5362240 m*) are made up of well bedded Oxfordian limestones whereas the upper part of the profile contains massive Kimmeridgian limestones representing a riff facies with sponges and algae being the main rock forming species (Geyer & Gwinner 1991, Etzold et al. 1996). The bedding is (sub-) horizontal, dipping slightly ( $<5^\circ$ ) to the SE on a regional scale. The principal structural features are ENE-WSW striking graben structures, which exhibit a mixed mode displacement with a major normal and a subordinate dextral component (Geyer & Gwinner 1991, Etzold et al. 1996). The investigated stylolites (*Samples: Sa6/1a, Sa6/1b, Sa9/2*) form vertical planes which trend WNW-ESE with teeth pointing parallel to the surface normal direction, hence recording a NNE-SSW compression (Fig. 3.2 a). Additionally small scale reverse-faults and NNE-SSW trending joints confirm the same kinematic framework. A younger subordinate set of stylolites not investigated in this study form NE-SW trending vertical stylolite planes which can be related to the prominent dextral graben structures found in the area (Geyer & Gwinner 1991, Kley & Voigt 2008). Our relative chronological sequence of deformation events is in agreement with data reported by Kley and Voigt (2008), demonstrating a change in the stress field from NNE-SSW directed compression in the late Cretaceous to a NW-SE directed compression in the Neogene.

The Iberian Chain of north-eastern Spain is located south of the Ebro-basin and trends roughly NW-SE. The succession is composed of up to 6000 m of Mesozoic, mainly Jurassic and Cretaceous sediments (Capote et al. 2002), although the sequence is significantly reduced to only 300-400 m in the investigated area. The investigated area belongs to the Maestrazgo structural domain which forms the transition zone between the NW-SE striking fold and thrust belt of the Aragon Branch and the NE-SW striking Catalanian Coastal Ranges. The main structural features are ENE-WSW striking fold-trains and reverse-faults with top to the NNW kinematics. The onset of deformation is estimated to be around Early to Middle Eocene, whereas the deformational peak is assumed to be during the Oligocene (Liesa & Simón, Casas et al. 2000, Capote et al. 2002). Liesa and Simon (in press) report stylolite data which they argue to be attributed to Betic and Guadarrama compressions both having their deformational peaks during the Oligocene. The investigated section (*UTM 30T; E 07111963 m; N 4518336 m*) comprises well bedded limestones in an upper Jurassic upright antiform which contains several smaller synforms that plunges  $25^\circ$  to the NW. Stylolites were investigated in shallow ENE dipping limb (*set A* in Fig. 3.2 b) and from an

overturned limb which dips steeply to the SE (*set B* in Fig. 3.2 b). In the eastwards-dipping limb of the fold the stylolites (*Samples: M4/1, M4/2, M4/3, M4/4*) track the far field shortening direction (SSE-NNW) confirmed from field measurements in other outcrops in the area. In the overturned and steeply

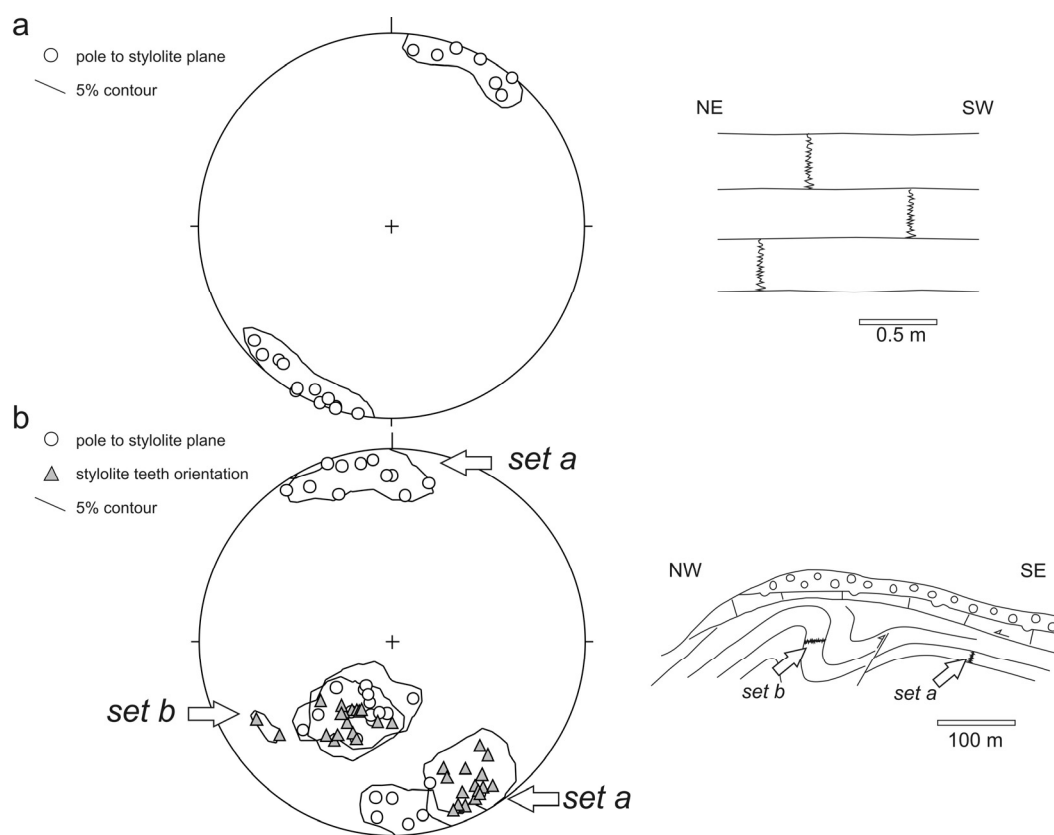


Figure 3.2 Lower hemispheric equal area projection (Schmidt's net) of the field data and schematic cross-sections of the investigated outcrops. **(a)** The Swabian Alb of southern Germany ( $n=22$ ). Right panel shows the flat lying Jurassic strata with vertical stylolites limited to individual beds **(b)** Iberian Chain of north-eastern Spain ( $n=32$ ). Right panel shows a cross-section of NE plunging fold and the position of *set a* and *set b* with respect to the fold limbs. All samples are from well bedded Jurassic strata. In the overlying massif Jurassic limestones (vertical stripes) and conglomerates (circles) no stylolites were found. Notice that in **(a)** only the poles to the stylolite planes are displayed since the shortening direction is normal to that plane. In panel **(b)** two populations are shown which correspond to the two investigated fold limbs. Poles to planes (circles) diverge slightly from the orientation of the long axis of the teeth (triangle); See text for detailed explanation.

dipping fold-limb the stylolites (*Samples: M4c/1, M4c/3*) are rotated around the fold axis into a shallow dipping orientation (i.e. a counter-clockwise or clockwise rotation of  $65^\circ$  around the fold axis would transform the stylolite orientation from one limb into the orientation of the stylolites in the other limb of the fold). Hence, the stylolite formation in this outcrop predates the folding event. In addition the angle between the stylolite plane and the bedding (not shown) is consistent in both positions of the fold thus corroborating the evidence that stylolitization predates the folding event. Another important feature to notice is that the stylolite teeth are somewhat oblique ( $\sim 10^\circ$ ) to the mean stylolite plane, which we interpret as a result of pressure-solution overprint of a pre-existing joint-set which strikes NE-SW, sub-parallel to the stylolite planes.

### 3.3. Methodology

The samples collected in the locations described above were all taken oriented in the outcrop to reconstruct the spatial position of the 3D stylolite morphology after laser profilometry. For analysis only “closed” specimens were considered. Stylolite surfaces that were already open in the outcrop and were subjected to an unknown amount of weathering were ignored. The sampled specimens were opened mechanically along the two opposing interfaces of the stylolite. This method causes some negligible damage to the surface due to the interlocking of asperities. The split surfaces were cleaned from any clay material, i.e. the residuum of the dissolved rock, with a soft brush and distilled water. Areas which did not exhibit visual mechanical damage were chosen for profilometry.

Optical profilometry is based on a laser triangulation of the surface similar to previous studies (Renard et al. 2004, Schmittbuhl et al. 2004, Schmittbuhl et al. 2008). The triangulation technique uses a laser beam that is focused on the surface of the object, which is monitored by a nearby CCD sensor. The distance between the object and the sensor changes as a function of changes of the angle under which the point of consideration is observed. The distance between the object and the laser-head is then calculated from angular relationships (Schmittbuhl et al. 2008). Before every individual measurement a test run was made to calibrate voltage fluctuations of the laser beam (voltage-height relationship is virtually linear in the chosen range, which gives the estimate of the vertical resolution – small distortions of the profile height, less than 1%, can be expected.). The laser beam is 30  $\mu\text{m}$  wide and horizontal steps between measurement points were  $\Delta x = \Delta y = 25\mu\text{m}$  with a horizontal precision of  $1\mu\text{m}$ . The vertical resolution is  $2\mu\text{m}$ . Maps were constructed by movement of the laser-head along parallel profiles over the specimen (Fig. 3.3). Eight samples have been measured at high resolution ( $\Delta x = \Delta y = 25\mu\text{m}$ ) with map sizes of  $1200 \times 1200$  (Samples: *M4/1*, *M4/4*),  $1600 \times 1600$  (Samples: *Sa6/1a*, *Sa6/1b*, *M4/2*, *M4/3*, *M4c/1*, *M4c/3*) &  $2000 \times 2000$  measurement points (Sample: *Sa9/2*), which corresponds to square maps with physical side lengths of 30, 40 and 50 mm. Care was taken that from the orientation of map x/y direction the sample orientation could be reconstructed.

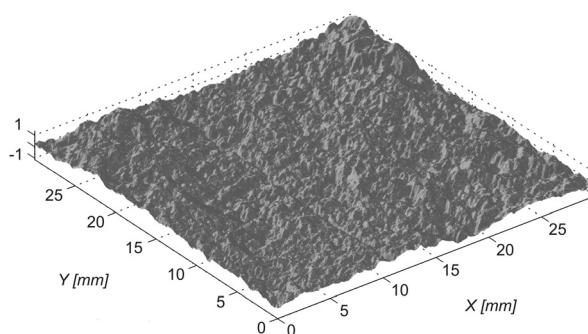


**Figure 3.3** Oblique view of the 3D morphology of the surface of an opened stylolite (sample *M4/4*) reconstructed from optical profilometry. A linear trend is removed from the raw data (compare Fig. 3.4 for details).



Additionally Sample Sa6/1 was measured twice where the second measurement (Sa6/1b) was rotated  $32^\circ$  clockwise around a vertical axis with respect to the first measurement (Sa6/1a). This was done to test the robustness of the measurements used against possible noise arising from the measurement procedure along discrete profiles. An image registration (Goshtasby 1986, 1988) of the two measurements in spatial domain revealed the same amount of rotation of  $32^\circ$  with an uncorrelated noise in the height difference between the two images that arises from the discreteness of the two maps (not shown). This height difference is less than 5% (i.e. the ratio of the standard deviation  $\sigma$  of the height difference is 0.063 mm to  $\sigma$  of the height of the surface 1.477 mm). Hence, there seems to be no significant error introduced by the measurement procedure.

### 3.4. Data analysis

Before we analyzed the 2D maps in detail the raw data from the laser profilometry was subjected to a series of pre-treatments (Fig. 3.4). First a mean plane calculated from a least square fit was subtracted from the raw data (Fig. 3.4 a), i.e. the x/y-plane is adjusted to a global trend and the vertical (z) axis is set to have zero mean height (Fig. 3.4b). To increase the quality of our Fourier transforms (described below) we used a Hanning window technique (Karcz & Scholz 2003, Press et al. 2007) to force our data to taper to zero at the boundaries (Fig. 3.4 c) in order to reduce spectral leakage (compare Fig. 3.3). This is a standard technique in signal processing, which does not modify the frequency and amplitude of the original signal.

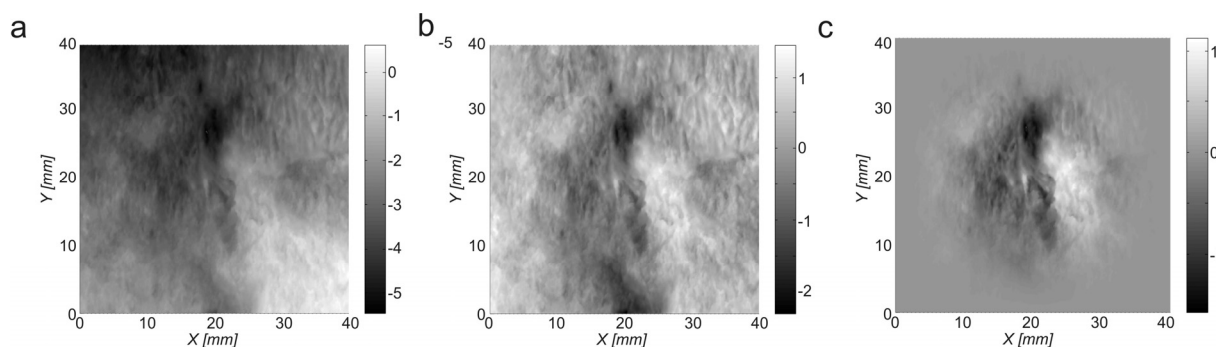


**Figure 3.4** Grayscale maps of sample M4/3 where **(a)** shows the raw data from profilometry (notice a general trend from the top left to bottom right); **(b)** detrended data i.e. linear trend is removed and mean height is set to be zero; **(c)** detrended data which is modified with a Hanning window technique where the data is forced to taper off to zero at the boundaries (for explanation see text). Light colors correspond to peaks and ridges and dark colors represent local depressions.

#### 3.4.1. 1D analysis

From the 2D height-field a 1D profile can be extracted either along the x or y-direction or in any arbitrary direction. For an arbitrary 1D profile  $f(x)$  the Fourier transform  $F(s)$  can be calculated and the power spectrum  $P \sim |F(s)|^2$  of the transform can be plotted as a function of the wave number  $k = 2\pi/\lambda$  [ $m^{-1}$ ], which scales inversely to the wavelength  $\lambda$  (Schmittbuhl et al. 1995, Renard et al. 2004, Schmittbuhl et

al. 2004). In Figure 3.5 the averaged spectra of Sample M4/3 along the x and y direction of the measured map are shown. The averaged spectra are found from calculating the mean of every  $k$ -value over all 1D profiles in one direction (Renard et al. 2004, Schmittbuhl et al. 2004). This averaging procedure reduces the noise attached to an individual 1D profile. A linear slope of the power spectra confirms a self-affine scaling invariance. The power spectrum of a self-affine signal behaves as

$$P(k) \sim k^{-D-2H}, \quad (3.2)$$

where  $D$  is the topological dimension of the signal ( $D=1$  for 1D profiles) and  $H$  the Hurst exponent. The Hurst exponent can thus be calculated from the slope of the power spectra.

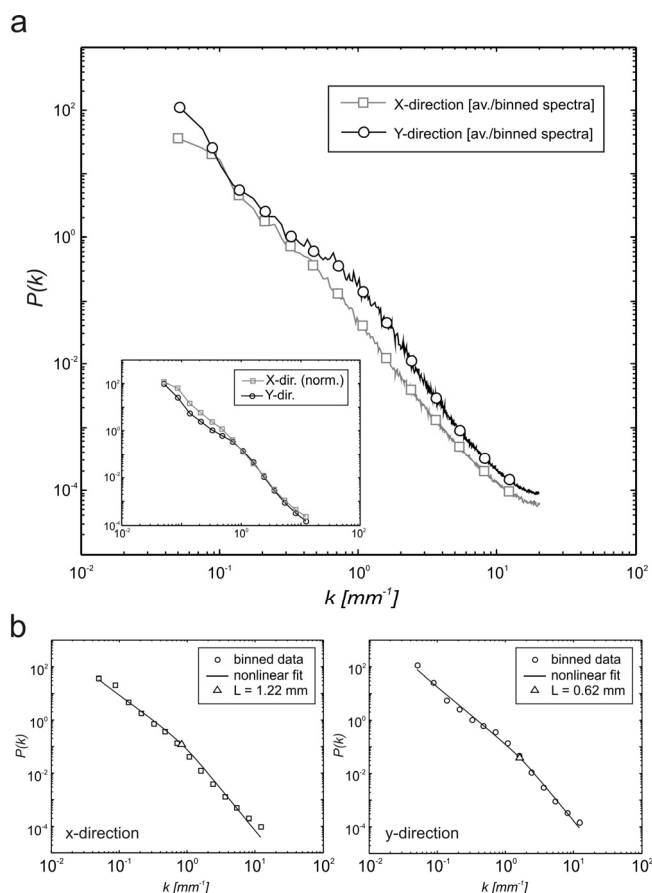


**Figure 3.5** 1D data-analysis of sample M4/3; **(a)** shows the averaged Power spectra  $P(k)$  (solid line) and the respective binned spectra (circles) plotted as a function of the wave number along the x and the y direction of the measured map. The inset in **(a)** again shows the power spectra for both directions but the x direction is now normalized with respect to the y direction  $P_x(k)/P_y(1\text{mm}^{-1})$ . This yields a collapse of the large  $k$ -values (small scales), notice that for the small  $k$ -values (large scales) the scaling functions deviate considerably **(b)** non-linear fit of the binned spectra for both directions used to estimate the crossover length  $L$  (triangle). Along the x-direction the crossover-lengths is larger ( $L=1.22$ ) than along the y-direction ( $L=0.62$ ). The branches slope of the non-linear model corresponds to Hurst exponents of 1.1 and 0.5 for small and large scales, respectively.

When we study the averaged 1D spectra of a tectonic stylolite along specific directions (Fig. 3.5 a) we see that the signal exhibits two slopes, which are separated by a crossover-length ( $L$ ) in agreement with observations on bedding parallel stylolites (Renard et al. 2004, Schmittbuhl et al. 2004, Ebner et al. 2009b).

The two observed scaling regimes have typical Hurst exponents of  $H_S \sim 0.5$  and  $H_L \sim 1.1$  for the small and large scale (large and small wave number), respectively. These observations indicate that the scaling of bedding parallel stylolites (Eq. 3.1) can be extended to tectonic stylolites (compare Fig. 3.5 a). To enable a more detailed comparison of the power spectra of our tectonic stylolites from two different (orthogonal) directions we normalize the power spectra along the x-direction with the power spectrum of the y direction at  $k=1[\text{mm}^{-1}]$  i.e.  $P_x(k)/P_y(1[\text{mm}^{-1}])$  as shown in the inset of Figure 3.5 a. This normalization yields a collapse of the large k-values (small scales), but a notable difference for the small k-values (large scales) of the scaling functions. This is basically the expression of the shift in cut-off between the two linear sub-branches, which is the crossover-length  $L$ . Figure 3.5 b shows that the calculated cut-off between the scaling regimes and thus crossover length differs between them. With 1.22 and 0.62 mm for the x and y-directions the crossover-length changes by 0.6 mm (Fig. 3.5 b). The non-linear fitting plotted as a solid line in both panels of Figure 3.5 b is a linear-by-parts least square fit in logarithmic space with a weighting function that changes from the small scale to the large scale fraction of the scaling law (for details compare Ebner et al., 2009b). This non-linear model uses a minimization algorithm to find the least square fit for the crossover-length. The differences found between the two directions also include a discrepancy in the scaling pre-factor, i.e. a vertical shift of the power spectra, which is clearly higher for all scales in the y-direction.

To fully quantify rough surfaces it is necessary to characterize this pre-factor of the scaling function and thus obtain a full description of the surface morphology. In the following we use the height-height correlation function, to calculate the scaling prefactor. The height-height correlation function (Barabasi & Stanley 1995), which is defined for a function  $h(x)$  over the spatial variable  $x$  by,  $C(\Delta x) = [\langle \{h(x) - h(x+\Delta x)\}^2 \rangle]^{1/2}$ , where  $\langle \rangle$  denotes average over the range of  $x$ , which estimates the average height difference between two points of the profile separated by a distance  $\Delta x$ . For a self-affine profile, the correlation-function follows a power-law such that  $C(\Delta x) \sim t^{1-H} \Delta x^H$ , where  $H$  is the Hurst exponent and  $t$  is the scaling prefactor. The prefactor can be designed as  $C(t) = t$ , and thus denotes a length scale, also known as the topothesy (Simonsen et al. 2000, Renard et al. 2006, Schmittbuhl et al. 2008). The topothesy corresponds physically to the length scale for which the slope of the rough profile is equal to 1. In other words,  $t$  is the theoretical length scale over which the rough profile has a mean slope of  $45^\circ$ . The smaller  $t$ , the flatter the profile appears on a macroscopic scale.

Figure 3.6 a shows a scaling of the correlation function with two linear sub-branches separated by a crossover-length similar to the scaling of the power spectra shown in Figure 3.5 a with only the slopes being different. The correlation function shows, similar to the power spectra, two linear sub-branches separated by a distinct crossover-length. To model our data we use the same linear by parts fit as for the power spectra (for explanation see above). We again fixed the slopes, which are equal to the Hurst exponents to values of 0.6 and 0.3 for small and large scale, respectively. This procedure was necessary to cope with the noise associated with individual 1D profiles extracted from the surface. The different scaling exponents compared to the power spectral approach is inline with reliability of self-affine

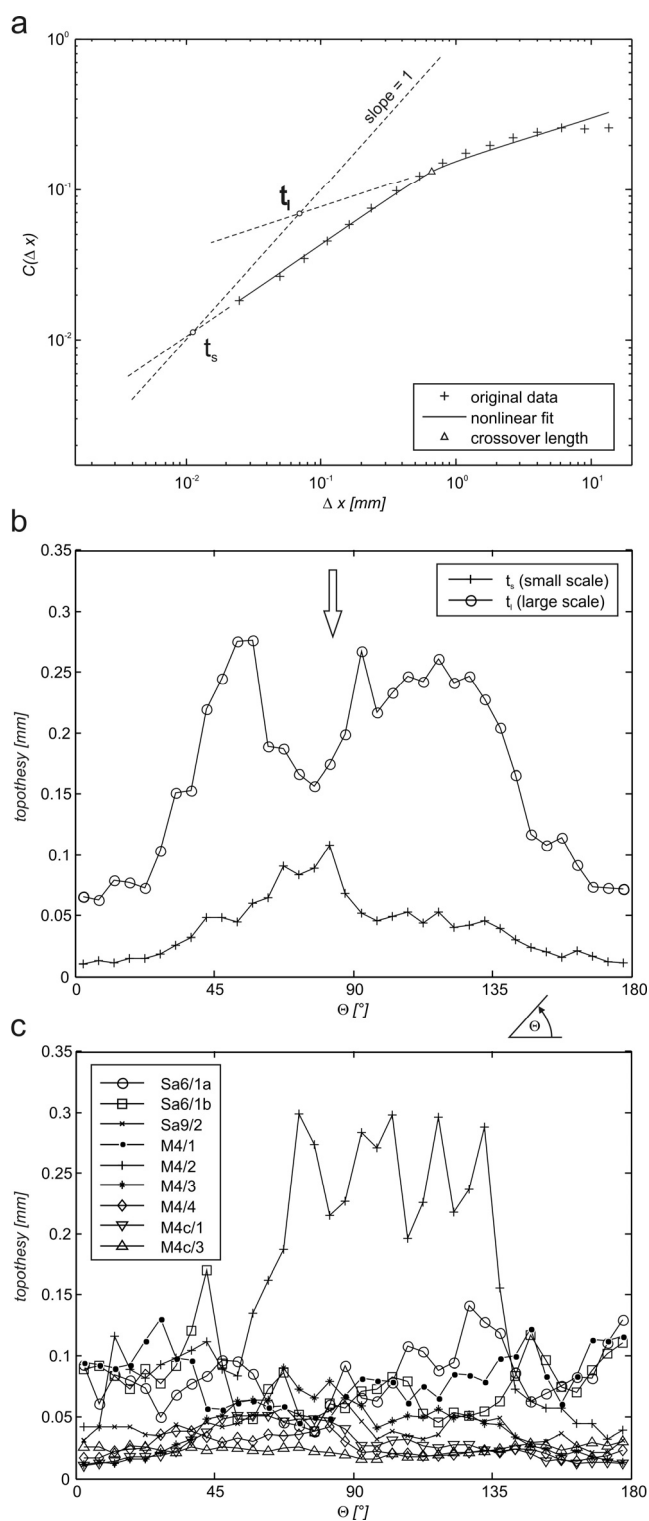


**Figure 3.6** 1D analysis of the scaling prefactor i.e. the topothesy of tectonic stylolites. **(a)** A log log plot of the correlation function  $C(\Delta x)$  of a 1D slice of sample M4/3 oriented parallel to the x direction of the analyzed surface with the nonlinear fit (compare text for details) and the topothesies  $t_s$  and  $t_l$  for small and large scale sub-branches. The topothesy is constructed from the intersection of the linear sub-branches with the 1/1 line. **(b)** The topothesies  $t_s$  and  $t_l$  of sample M4/3 plotted as a function of  $\theta$  i.e. the counter clockwise angle from the x-direction of the map. Note that the correlation functions are averaged over  $5^\circ$  intervals. Arrow indicates the vertical direction projected on the stylolite plane. Note that only the  $t_s$  shows a clear correlation with the sample orientation. **(c)** The small scale topothesy  $t_s$  for all samples plotted as a function of  $\theta$ .

measurements performed on synthetic signals (Schmittbuhl et al. 1995, Candela et al. 2009). These authors have demonstrated that the correlation function underestimates the input Hurst exponents. We thus conclude that the results are still comparable to the Hurst exponents obtained by the power spectral approach described above. The scaling prefactor and thus the topotheses  $t_s$  and  $t_l$  for the small and large scale regimes can be found by intersection of the two sub-branches of the scaling function with the 1/1 line (Fig. 3.6a). We estimated the topothesy for all orientations on the surfaces (Fig. 3.6 b & c) and found that there is an anisotropy in the scaling pre-factor, which shows a correlation with the highest topotheses being parallel to the horizontal direction in the sample orientation (Figure 3.6 b) for most samples (similar to the 2D anisotropy discussed in the following section; also compare Fig. 3.9). Only the topothesy for the small scale regime  $t_s$  shows a clear correlation with the vertical sample direction but the correlation of the large scale topothesy with the sample orientation is obscure. This observation is similar to what we found from investigation of the power spectra where the small scale regime is shows very consistent results but the large scale regime reveals a higher degree of variability e.g. compare inset in Figure 3.5 a. Hence we only show the small scale topothesy in Fig. 3.6 c. For sample Sa9/2 and M4/4 the signal to noise ratio (Fig. 3.6 c) is too high to observe anisotropy. Since the anisotropy in the (small scale) topothesy can not be shown without a doubt for all samples we give average topotheses for small and large scale regime of all samples (Table 3.1).

**Table 3.1** Topothesy for all samples calculated with fixed Hurst exponents.

Sample Nr.	small scale		large scale	
	Hurst exp.	Topothesy [mm] /std	Hurst exp.	Topothesy [mm] /std
Sa6/1a	0.6	0.08 ±0.02	0.3	0.29 ±0.04
Sa6/1b	0.6	0.08 ±0.03	0.3	0.28 ±0.04
Sa9/2	0.6	0.04 ±0.01	0.3	0.21 ±0.03
M4/1	0.6	0.08 ±0.02	0.3	0.25 ±0.04
M4/2	0.6	0.15 ±0.09	0.3	0.33 ±0.07
M4/3	0.6	0.04 ±0.02	0.3	0.17 ±0.07
M4/4	0.6	0.025 ±0.008	0.3	0.12 ±0.05
M4c/1	0.6	0.03 ±0.01	0.3	0.16 ±0.06
M4c/3	0.6	0.023 ±0.004	0.3	0.14 ±0.03

Both the power spectra (i.e. the cut-off length between the linear sub-branches) and topothesy of a 1D signal show a considerable degree of anisotropy which is often obscured due to the noise associated with an individual 1D profile. We conclude that to account for this in-plane variation a 1D signal fails to capture all scaling characteristics of tectonic stylolites and the choice of the investigated profile is not arbitrary as for bedding parallel stylolites. Hence, tectonic stylolites have a measurable in-plane anisotropy which we want to characterize in detail with a 2D approach.

### 3.4.2. 2D analysis

For the 2D analysis we used the processed data as described in section 3.4 (Fig. 3.3 c). First a 2D Fourier transform i.e. a discrete Fourier transform (DFT) was calculated from the data points of the 2D height-field with the Fast Fourier Transform (FFT) algorithm (Cooley & Tukey 1965) implemented in *Matlab*<sup>®</sup>. Then the DFT is shifted so that the zero-frequency component lies in the centre of the spectra and the 2D power spectrum  $P(k_x, k_y)$  is again calculated as the square of the absolute magnitude of the Fourier transform. Figure 3.7 a displays a map of the 2D power spectra  $P(k_x, k_y)$  in which the absolute magnitude squared is shown as grayscale values and  $k_x$  and  $k_y$  range from  $-((n/2)*\Delta x)^{-1}$  to  $((n/2)*\Delta x)^{-1}$  where  $n$  is the number of measurement points in one direction of the map and  $\Delta x$  is the step size. To investigate the power law behavior located in the 1D signals the 2D power spectra had to be transformed to a double logarithmic space originating from the centre of the map i.e. the zero frequency component or the smallest wave number. This is accomplished by translating every value pair  $(k_x, k_y)$  by  $\log[|(k_x^2 + k_y^2)^{0.5}|]$  along the direction defined by the direction cosine of the position vector  $(k_x, k_y)$  with the x-axis of the coordinate system and plotting  $\log(P(k_x, k_y))$  on the newly formed logarithmic grid.

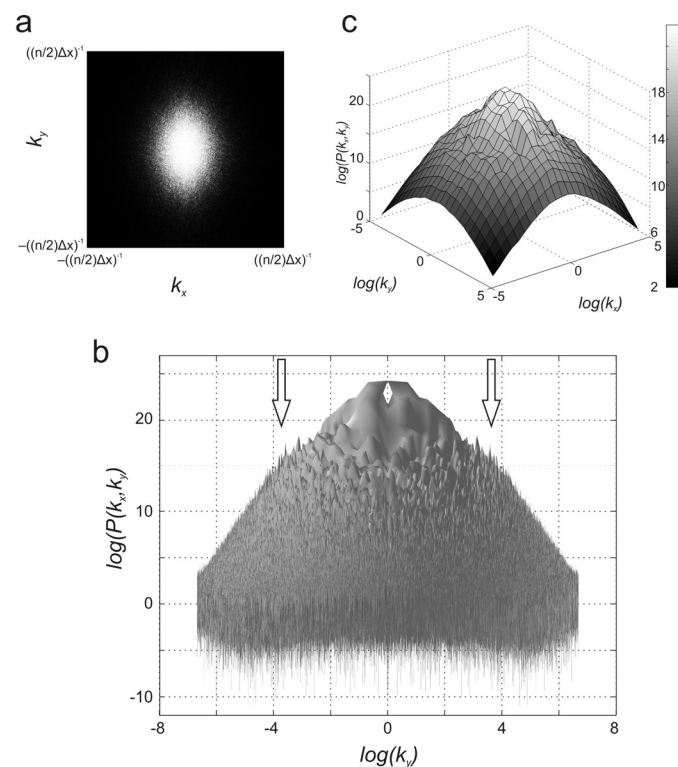


**Figure 3.7** 2D data-analysis of sample M4/3; **(a)** 2D Fourier transform plotted on a regular grid as a function of  $k_x$  and  $k_y$  which range from  $-((n/2)\Delta x)^{-1}$  to  $((n/2)\Delta x)^{-1}$  where  $n$  is the number of measurement points in one direction of the map and  $\Delta x$  is the step size. (notice that the zero frequency component lies in the centre of the map). A clear anisotropy of the data can be observed sub-parallel to the  $k_y$ -axis (vertical axis). To investigate the power law scaling exhibited by the 1D analysis the 2D Fourier transform is converted to a double log-space where  $\log(k_x, k_y)$  is plotted as a function of the logarithm of the power spectra **(b)**; the 2D power spectra are plotted as a surface whose height corresponds to  $\log(P(k_x, k_y))$ . The 3D surface is viewed along the  $k_x$ -direction and the arrow indicates the crossover-length  $L$ , which separates the two scaling regimes i.e. the two linear subparts of the slope of the cone. **(c)** Oblique 3D view of the binned 2D power spectra which were calculated to get a constant density of the data-points in logarithmic representation (for details see text).

The central point in this case corresponds to the system size, which imposes the smallest non-zero  $k$ . Figure 3.7 b illustrates such a double log-plot of sample M3/4, in which the power spectra are displayed as a 3D surface. Notice that the view direction is along the  $k_x$ -axis. The slopes of the surface, which roughly describe an elliptical cone clearly exhibit two linear branches and a distinct crossover region ( $L$ ) marked by the arrow in Figure 3.7 b. Thus the 3D representation is consistent with the scaling behavior found from the analysis of the 1D signal.

For further analysis of the anisotropy we resample the 3D representation (Fig. 3.7 b) with a 2D logarithmic binning (along  $k_x$  and  $k_y$  direction), to get a constant density of grid points in double-logarithmic representation (Fig. 3.7 c). For this reason a fixed grid that covers the 2D power spectra with a constant bin size ( $bs$ ) in logarithmic space ( $\log(bs) = 0.4$ ) in the x and y direction is used to find all  $k_x, k_y$ -value pairs that fall into a certain bin, and the mean of all power spectra that belong to these  $k_x, k_y$ -value pairs in this bin is then used to define the binned power spectrum. This procedure allows analyzing the data with an equal importance for the long and small scales, respectively. In addition this method smoothes the data by removing the local fluctuations without an alteration of the overall geometry of the 3D representation, that is characterized by the two scaling regimes and the distinct crossover.

We use isopach/contour maps of the binned 2D power spectra to quantify the degree of anisotropy. Isotropic signals should reveal concentric circular contour lines, which define the same  $\log(P(k_x, k_y))$  value. Concentric circular contour lines would imply that the crossover length, which separates the self-affine scaling regimes for small and large scales are the same in every direction. Figures 3.8 show that this is clearly not the case for tectonic stylolites (also compare Fig. 3.7 a) where the contour lines reveal an elliptical shape (Fig. 3.8 a & b). This shape is clearly different from the circular concentric contours found in bedding parallel stylolites (compare e.g. to Figure 4 of Schmittbuhl et al., 2004). We use a least square criterion to estimate the best fit ellipse of the individual contour lines. From the best fitted ellipse, we calculate the aspect ratio of the principal axis (i.e.  $a/b$ ; where  $a$  and  $b$  are the semi-major and semi-minor axis of the best fitting ellipse) to get a quantitative measure of the anisotropy of the 2D binned power spectra (Fig. 3.8 c). For the direction of the anisotropy we utilize the angle  $\Theta$  between the long axis ( $a$ ) of the fitted ellipse and the x-direction of the coordinate system (Fig 3.8 d). For all investigated samples we recognized an increased ellipticity toward the centre of the 2D power spectra but only a moderate or no significant change in orientation of the asymmetry with respect to the position in the power spectra. Note that in this representation (Fig. 3.8) high contour lines (small wave numbers) correspond to large physical length-scales whereas low contour lines (large wave numbers) correspond to small length-scales.

The fact that the large wave numbers display an isotropic power spectrum i.e. aspect ratio close to 1 (Fig. 3.8 c), whereas the small ones show an anisotropic one, is very consistent with the result of the 1D data analysis (see previous section). Beyond that this observation is also in agreement with the physical interpretation of the mechanism stylolite formation and morphogenesis (Renard et al. 2004, Schmittbuhl et al. 2004, Koehn et al. 2007, Ebner et al. 2009b): At small scales (large wave numbers), the balance between surface tension and disorder is controlling the shape of stylolites. Both are a priori isotropic along the stylolite. On contrary, the large scale morphologies (small wave numbers) are normally physically

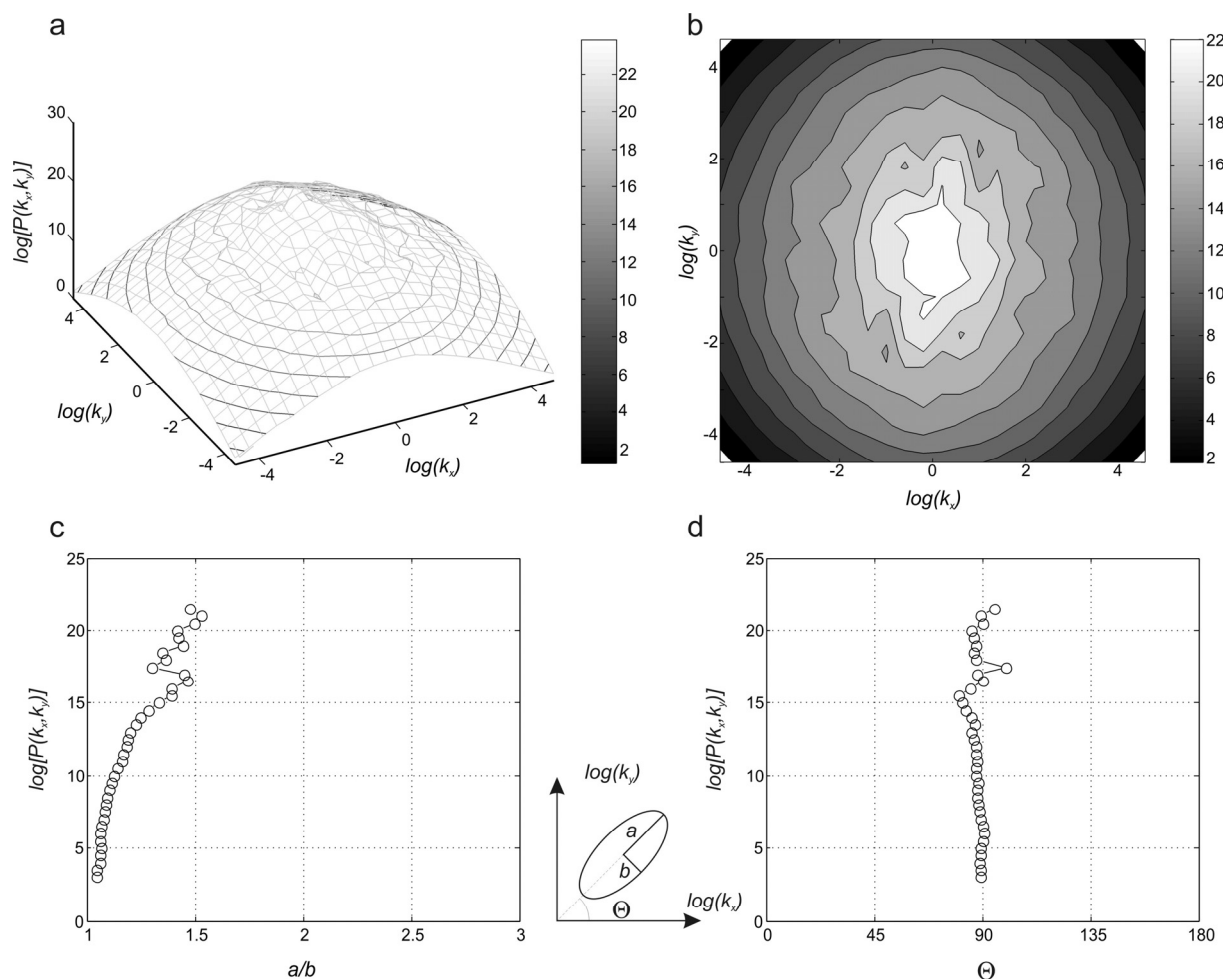


**Figure 3.8** Quantification of the 2D scaling anisotropy of sample M4/3; **(a)** oblique 3D view of the binned 2D power spectra (gray mesh) with an overlay of colored contour lines of constant  $\log(P(k_x, k_y))$ -values. **(b)** map view of the contours calculated from the conic 2D power spectra. These contours were utilized to calculate best-fitting ellipses using a least squares approach; **(c)** Aspect ratio ( $a/b$ ) of the fitted ellipse for every  $\log(P(k_x, k_y))$ -contour. An increasing aspect ratio towards the centre of the map is characteristic for all samples investigated. **(d)** Slope (i.e. the counter clockwise angle from the x-direction of the measured map) of the long axis of the fitted ellipse plotted for the contour intervals.

interpreted as resulting from a balance between the elastic field and the material disorder is controlling the shape of the stylolites. The fact that anisotropy is observed at large scales is thus the signature of an in-plane anisotropy of the stress. Since stylolites are normally perpendicular to largest stress direction associated to  $\sigma_1$ , this large scale anisotropy should be associated to a difference between the two principal values of the in-plane stress components,  $\sigma_2$  and  $\sigma_3$ .

The orientation of the long axis of the fitted ellipse relative to the x direction of the scanned maps is shown in rose diagrams (Fig. 3.9) for all samples. These long axes of the contours of the power spectrum are associated with a shorter crossover-length  $L$  (i.e. reciprocal to the wave number) between the large  $k$  isotropic scaling and the small  $k$  anisotropic one (Fig. 3.9 j). We will see in the next sections that this can be interpreted as arising from a larger difference between the largest principal stress (normal to the stylolite plane) and the one associated to this direction (in-plane), than for the perpendicular one. The principal stress associated to this long axis direction should thus be the smallest one, i.e.  $\sigma_3$ . Arrows show



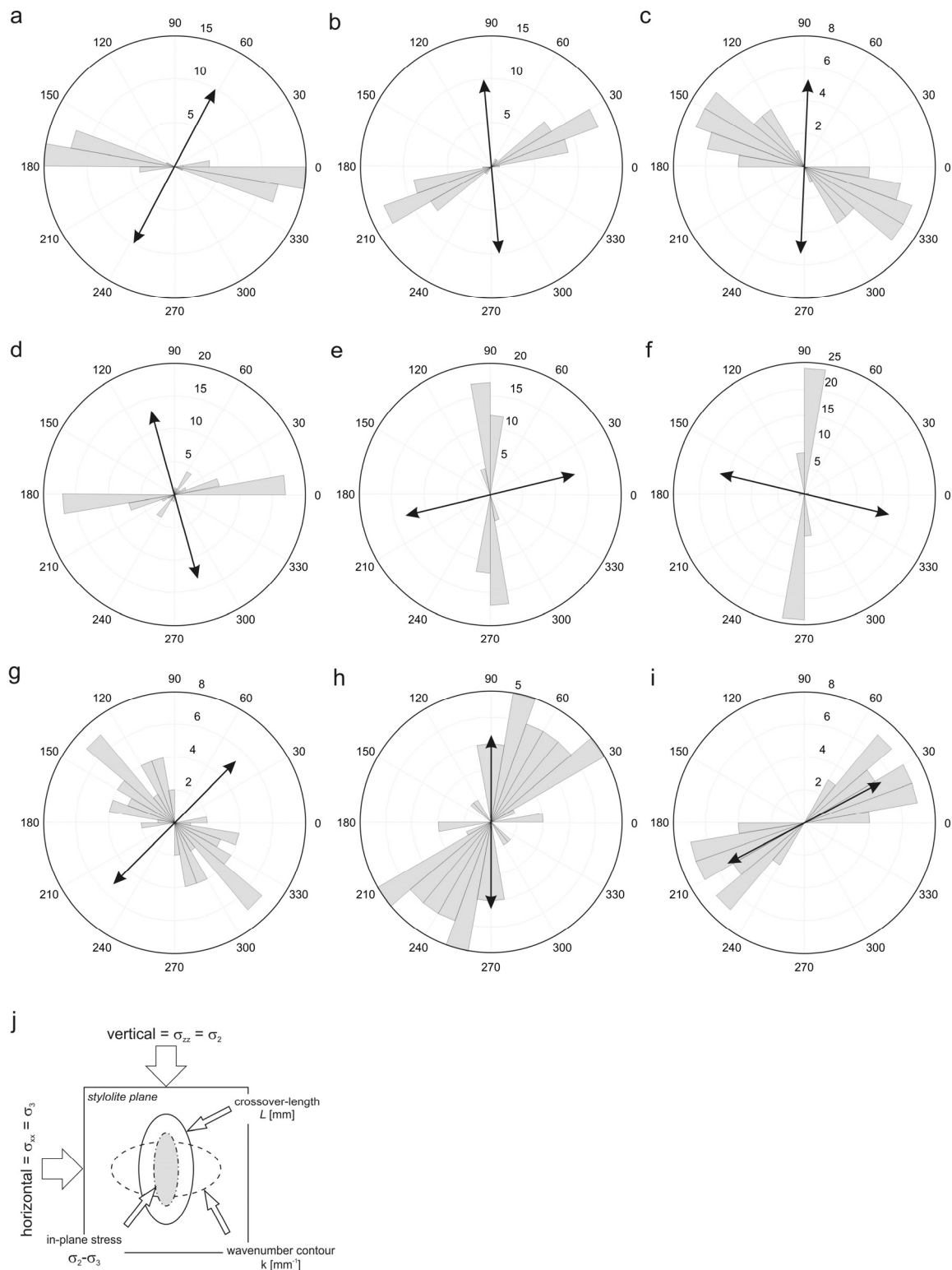
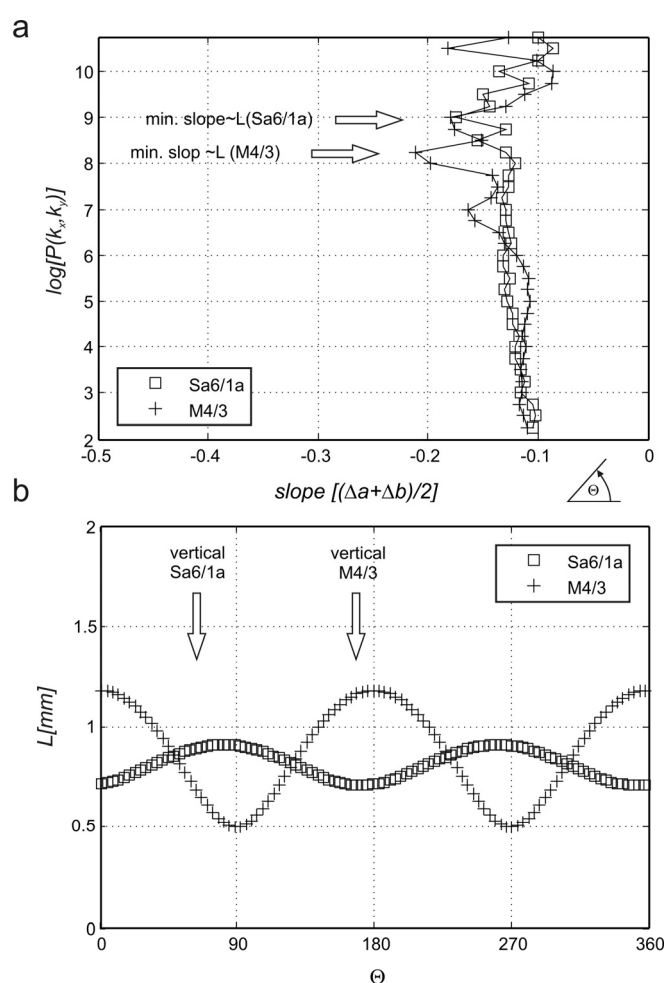


Figure 3.9 Rose diagrams of all samples i.e. a histogram with a constant bin size of  $10^\circ$  of the (counter-clockwise) angle of the long axis of the fitted ellipse to the x-axis of each sample. Arrow in each panel shows the intersection of the vertical direction of the oriented sample with the mean stylolite plane. **(a)** sample Sa6/1a, **(b)** sample Sa6/1b, **(c)** sample Sa9/2, **(d)** sample M4/1, **(e)** sample M4/2, **(f)** sample M4/3, **(g)** sample M4/4, **(h)** sample M4c/1, **(i)** sample M4c/3; Notice that for all samples the long axis and thus the direction with the smallest crossover length is roughly normal to the vertical direction (except for h & i; for explanation see text). This direction corresponds typically to the largest differential stress, which is also the smallest in-plane stress. **(j)** Schematic drawing of the relationship between the wave number contour [ $\text{mm}^{-1}$ ] (compare Fig. 3.8), the crossover-length  $L$  [mm], the principal in-plane stresses and the sample orientation i.e. horizontal and vertical direction. Revert to text for detailed explanation.

the orientation of a vertical line projected onto the stylolite plane in its original outcrop orientation. From this representation (Fig. 3.9) it is evident that the vertical direction is roughly normal to the long axis of the anisotropy for all samples except M4c/1 and M4c/3 that have a shallow dipping plane which is rotated due to folding (Fig. 3.9 h & i).

To estimate the crossover length ( $L$ ) and thus get quantitative information on the stresses during stylolite formation we again use the elliptical fit as a simplified representation of the 2D Fourier transform of our data. We assume that the crossover is located at the position of the biggest change in the local slope of the 2D Fourier transform (compare Fig. 3.7b). We calculate the local slope  $s$  as the difference between the long and short axis ( $a$ ,  $b$ ) of the best fitted ellipse for succeeding  $\log(P(k_x, k_y))$ -contours  $s = (\Delta a + \Delta b) / 2$ .



**Figure 3.10** Crossover length from the contour data of the maps for sample M4/3 and Sa6/1a. **(a)** Slope of the 2D power spectra calculated as the mean difference between the principal axis of the fitted ellipse ( $a$ ,  $b$ ). The biggest change in slope (arrow) is assumed to be the contour at which the crossover is located. **(b)** The crossover-length plotted as a function of the counter clockwise angle from the x-direction of the measured map. The vertical direction in the stylolite plane is indicated for both samples and roughly corresponds to the largest crossover-length i.e. the smallest differential stress as shown in Figure 3.1.

A plot of the  $\log(P(k_x, k_y))$ -contours as a function of the local slope  $s$  is shown in Figure 3.10 a. The crossover is defined to lie at the minimum local slope in this representation and the crossover is calculated from the principal axis of the best-fit ellipse at this minimum (Fig. 3.10 b). It can be noticed that the

maximum crossover-length coincides quite well with the vertical direction (indicated by arrow in Fig. 3.10 b) this is in agreement with our previous observations that the anisotropy of the power spectra is also oriented (normal) with respect to the sample vertical orientation (compare Fig. 3.9).

Before we discuss the orientation of the anisotropy and the determined crossover length-scales in relation to the stress tensor that was present during stylolite growth, we want to investigate the influence of tilted teeth on the scaling results.

### 3.4.3. Synthetic data analysis

It is important to prove that the large scale anisotropy we found in the investigated samples is really related to the stress field during formation and thus exclude the influence of other factors which might as well cause a scaling anisotropy. The second important characteristic of tectonic stylolites, as stated in the introduction, is the occurrence of inclined teeth i.e. slickolites. It is easy to imagine that the ridge and groove morphology of slickolites with highly inclined teeth can cause a difference in the scaling parallel or transverse to these elongated morphological features and thus an anisotropy. To systematically investigate the influence of a tilt of the asperities or teeth we construct synthetic isotropic self-affine surfaces and tilt the teeth around one axis. Tilted or inclined asperities are a common feature of slickolites (Simon 2007) and it is commonly assumed that these structures formed when a stylolite overprinted a pre-existing plane of anisotropy in the host-rock. In this case the principal stresses are oriented oblique to the pressure solution surface, which has recently been proven numerically by Koehn et al. (2007). Synthetic self-affine surfaces can be created following the approaches found in the literature (Turcotte 1997, Meheust & Schmittbuhl 2001). We follow the method described in Meheust and Schmittbuhl (2001) who construct square white noise maps of size  $n = 512$ . The self-affine correlation is then introduced by multiplying the modulus of the 2D Fourier transform of the white noise by the modulus of the wave number raised to the power of  $-1-H$ , where  $H$  is the roughness exponent. The self-affine surface is obtained from the inverse Fourier transform. The synthetic surface shown in Figure 3.11 a is constructed with a Hurst exponent of  $H=0.5$  and its 2D Fourier transform has a true isotropic self-affine behavior (compare inset in Fig. 3.11 a). A pre-defined tilt of the roughness is then attained from adding a linear trend along the x-axis of the map which corresponds to a tilt angle  $a$  and a subsequent back-rotation around  $a$  i.e. multiplying the data with a 3D rotation matrix of  $-a$ . Various tilt angles ranging from 1-50° were realized from the map shown in Figure 3.11 a. To analyze single valued functions (with no overhangs) the tilted surfaces are projected on a plane defined by the mean surface. The data were then analyzed as described in the previous chapter (section 3.4.2). The degree (aspect ratio) and orientation (slope) of the anisotropy is displayed in Figure 3.11 b & c. It is evident that the original data-set is isotropic with aspect-ratios for  $\log(P(k_x, k_y))$  contours close to 1.

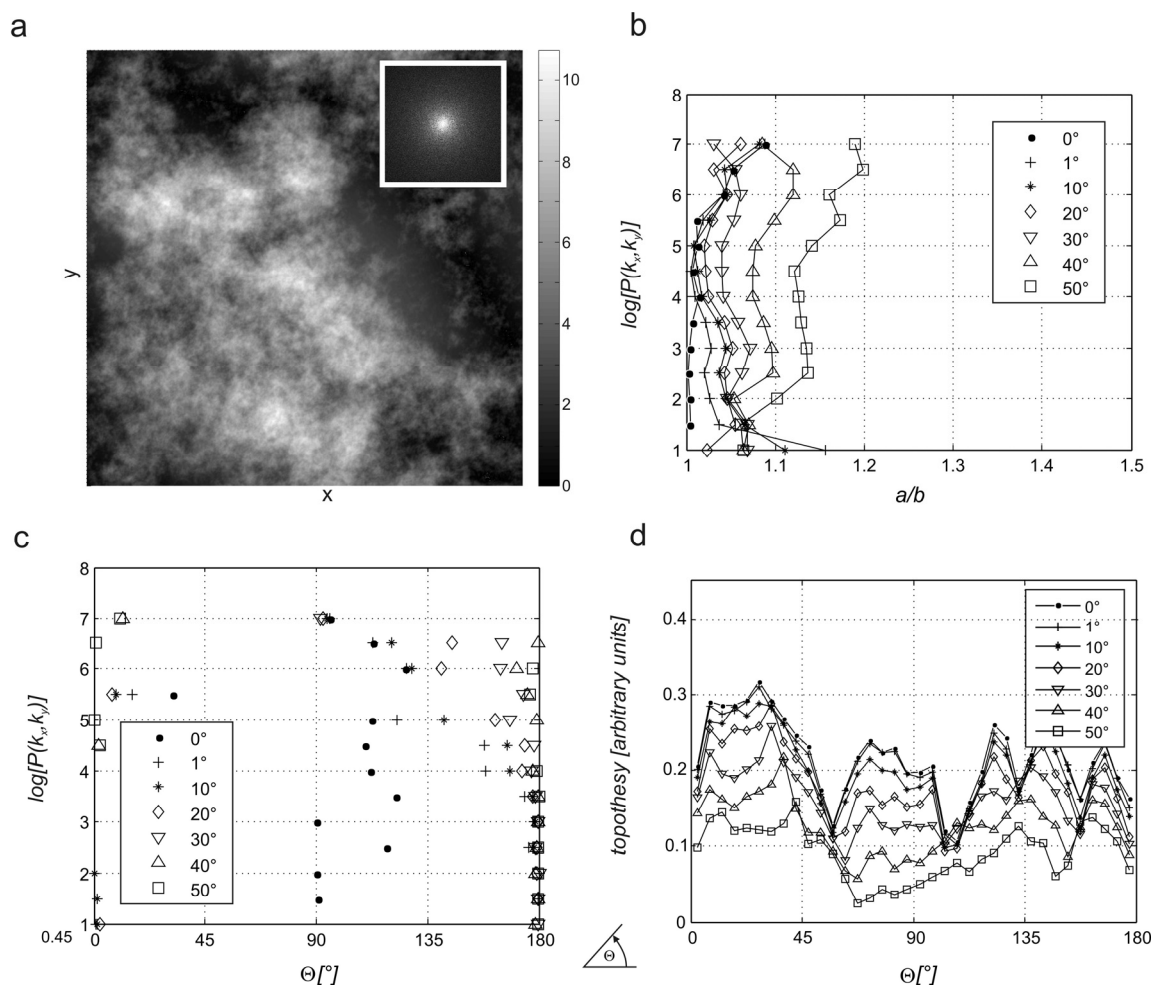


**Figure 3.11** Grayscale map (a) of a synthetic self affine square surface with a side-length of 512 and a Hurst exponent of 0.5. Inset displays a 2D Fourier transform of that map, which clearly exhibits isotropy with respect to its centre, similar to bedding parallel stylolites. This dataset is then utilized to construct slickolites i.e. stylolites with oblique teeth and asperities (see text), with various tilt angles (e.g.  $10^\circ$  correspond to oblique asperities that are rotated  $10^\circ$  counter clockwise around the x-direction with respect to the mean plane of the synthetic surface). (b) Aspect ratio of elliptical fit of synthetic data set (compare Fig. 3.7c). For small tilt angles an anisotropy on small scales (i.e. large wave numbers and low  $\log(P(k_x, k_y))$ -contours) can be observed. For large tilt angles a general increase of the aspect ratio over all scales can be found. (c) Orientation of the long axis of the fitted ellipse (compare Fig. 3.7 d). Notice an increasing alignment of the long axis of the fitted ellipse towards higher  $\log(P(k_x, k_y))$ -contours with increasing tilt angles.

With small tilt angles  $a < 10^\circ$  an anisotropy for the low  $\log(P(k_x, k_y))$  contours and thus large wave numbers and small scales exists, which decreases with increasing  $a$ . In addition there is a general increase in the anisotropy in all scales with tilt angles of  $a \geq 20^\circ$  (Fig. 3.11 b) whereas the orientation is more and more aligned with the rotation/tilt axis (Fig. 3.11 c) with increasing tilt angle. The topothesy of the synthetic surfaces do not exhibit a directional anisotropy (Fig. 3.11 d) but a general decrease as expected. Table 3.2 shows the averaged topothesies for all analyzed surfaces also showing a decrease of the topothesy with increasing tilt angle.

**Table 3.2** Topothesy for synthetic surfaces with various inclined teeth.

Data Set.	Hurst exp./std	Topothesy /std
orig. data	0.34 ±0.05	0.22 ±0.05
1°	0.34 ±0.05	0.21 ±0.05
10°	0.35 ±0.05	0.20 ±0.05
20°	0.35 ±0.05	0.18 ±0.05
30°	0.34 ±0.04	0.16 ±0.04
40°	0.34 ±0.04	0.13 ±0.04
50°	0.34 ±0.05	0.09 ±0.04

### 3.5. Discussion

We have shown that tectonic stylolites, i.e. stylolites which form when the principal compressive stress direction is horizontal, differ fundamentally from bedding parallel stylolites since they show anisotropic scaling relations. Two self affine scaling regimes (with Hurst exponents of  $\sim 0.5$  and  $\sim 1.1$  for the small and large scale, respectively), which are separated by a crossover-length at the millimeter scale can be found in bedding parallel and tectonic stylolites. The crossover-length  $L$  scales inversely with the formation stress  $L \sim \sigma^{-2}$  for bedding parallel stylolites (Ebner et al. 2009b). Utilizing the analytical solution of Schmittbuhl et al. [2004] that relates the crossover length ( $L$ ) to the stress-field during stylolite formation, with the stress term being a product of mean and differential stress, can be used to calculate the stress magnitudes in addition to the determination of principal stress directions. The analytical solution shows that

$$L = \frac{\gamma E}{\beta \sigma_m \sigma_d}, \quad (3.3)$$

where  $E$  is the Young's Modulus,  $\gamma$  is the solid-fluid interfacial energy,  $\beta = \nu(1-2\nu)/\pi$  is a dimensionless constant with  $\nu$  the Poisson's ratio,  $\sigma_m$  and  $\sigma_d$ , are the mean and differential stresses respectively. Since for bedding parallel stylolites perfect confinement can be assumed (that is uniaxial strain or zero horizontal displacement) the stresses and thus the crossover length  $L$  is independent of the orientation within the stylolite surface (Fig. 3.1 a). For a tectonic stylolite this scenario is different (Fig. 3.1 b) and it can be assumed that the in-plane stresses are dissimilar. One in-plane principal stress component should be dependent on the amount of overburden and should be oriented vertically whereas the second stress component should have a horizontal orientation. Since the crossover-length  $L$  scales inversely with the product of mean and differential stress and the mean stress should be constant, variations of the crossover should reflect variations of the differential stress  $|\sigma_1 - \sigma_{inplane}|$  [compare to Schmittbuhl et al., 2004]. Therefore the crossover-length has to increase from a minimum in the direction of the least

principal stress  $\sigma_3$  (x-axis in Fig. 3.1 b) and thus the direction of the largest differential stress  $|\sigma_1 - \sigma_3|$  to a maximum in an in-plane orientation normal to this direction, which corresponds to the direction of the largest inplane stress  $\sigma_2$  (the vertical direction in Fig. 3.1 b), and the smallest differential stress  $|\sigma_1 - \sigma_2|$ . In conclusion it can be assumed that the orientation of largest and smallest crossover-length coincide with the vertical and horizontal direction (i.e.  $\sigma_{xx} < \sigma_{zz}$ ) respectively.

Indeed we found a scaling anisotropy in our data, which shifts the crossover-length accordingly (Fig. 3.9). The 1D analysis (Fig. 5) and the 2D data analysis (Fig. 3.9 & 3.10) reveal that the long axis of the detected anisotropy is normal to the vertical direction with a crossover-length maximum in this direction implying that  $\sigma_2$  has a vertical orientation. This observation holds for both investigated areas although there is a slight deviation of up to  $\pm 10^\circ$  for some samples. Only the samples (M4c/1, M4c/3) from the overturned fold limb of the investigated outcrop (compare Fig. 3.2 b and Figure 3.9 h & i) differ significantly. This can be explained by the fact that the stylolite formation was prior to folding as can be concluded from the structural relationships in the field data. Thus the present orientation of the samples in the overturned fold limb does not coincide with the orientation during formation of the stylolites.

We noticed a small difference ( $< 10^\circ$ ) between the orientation of the stylolite teeth and the pole of the mean stylolite plane for the samples from north eastern Spain. This is due to the fact that the stylolites overprint a pre-existing joint set that is subnormal to the principal shortening direction, which influenced stylolite formation as stated above. To investigate the effect of the tilt of the stylolite teeth and its contribution to the observed scaling anisotropy we used synthetic self-affine surfaces which were systematically tilted to get slickolite similar structures as explained above (Fig. 3.11). The effect of the tilt of the teeth with respect to the mean plane of the stylolite can be characterized by (i) an anisotropy for the large wave numbers i.e. on the scale of individual teeth or asperities for small tilt angles ( $< 10^\circ$ ) and (ii) a general homogeneous increase of the anisotropy for all scales with an increase of the tilt angle for angles  $> 10^\circ$ . This anisotropy caused by the imposed tilt of the asperities differs significantly from the anisotropy of real stylolites. Therefore we conclude that the 3D formation stress is the dominant force that influences the scaling anisotropy of the investigated samples. However one has to note that tilted teeth imply that the principal stress components are not necessarily oriented within the stylolite plane. Therefore only tectonic stylolites with plane-perpendicular teeth should be used to recalculate principal stress orientations and magnitudes.

The analytical solution (Schmittbuhl et al. 2004) is only strictly valid for 2D stress cases where the principal stresses parallel to the stylolite plane are invariant along the third direction, which is truly the case for bedding parallel stylolites as discussed by Ebner et al. (2009b). But since a solution for the 3D case is not available we argue that the above equation (Eq. 3.3) could serve as an ersatz, of a first approximation to calculate the order of magnitude and the difference between the principal stresses for such tectonic stresses. We assume that the crossover-length in a specific direction is mainly a function of the stresses in the plane normal to the stylolite surface along the direction of investigation and that the out of plane stresses are invariant. This would imply that the differential stresses for the vertical and horizontal directions could be defined as  $\sigma_{dv} = \sigma_{yy} - \sigma_{zz}$  and  $\sigma_{dh} = \sigma_{yy} - \sigma_{xx}$  and Eq. 3.3 could be solved if

the depth of stylolite formation and the material properties during stylolite formation are known. For the stylolites from the Swabian Alb with a vertical crossover of 0.95 mm and a horizontal crossover of 0.7 mm, assuming a Poisson's ratio of 0.25, a surface free energy of calcite of  $0.27 \text{ J/m}^2$ , a Young's Modulus of 14 GPa (Ebner et al., 2009b) and a vertical stress component ( $\sigma_2$ ) of 6 MPa (assuming a vertical load of 220 m of sediments with a density of  $2.7 \text{ g/cm}^3$  in agreement with sedimentological constraints) the tectonic stress component ( $\sigma_1$ ) is about 17.7 MPa and the horizontal in-plane stress ( $\sigma_3$ ) component is 1.8 MPa. See appendix for details of the calculation.

### 3.6. Conclusions

Tectonic stylolites show a 1D scaling invariance that resembles those of bedding parallel stylolites investigated in previous studies (Renard et al. 2004, Schmittbuhl et al. 2004, Ebner et al. 2009b). They have a self-affine scaling invariance, which is characterized by a Hurst exponent of 1.1 for long and 0.5 for short scales and a distinct crossover-length at the millimeter scale that separates these two scaling regimes.

High resolution laser profilometry of tectonic stylolites provides quantitative 3D information of these pressure solution surfaces that enables a 2D analysis of the surface morphology. We demonstrate that tectonic stylolites have an anisotropic scaling that is not independent of the orientation of the investigated section within the plane of the stylolite. This anisotropy's main characteristic is a systematic shift of the crossover length that separates the scaling regimes. The presented analysis also confirms that the anisotropy is always oriented with respect to the horizontal and vertical direction and thus the principal stress directions within the stylolite plane for vertical stylolites. The long axis of the anisotropy and thus the smallest crossover length consistently coincides with the horizontal direction in the stylolite plane, whereas the largest crossover-length is found in a vertical section. This observation is consistent with the fact that the horizontal in-plane stress is generally smaller than the vertical in-plane stress for tectonic stylolites (Fig. 3.1 b). They are also both smaller than the normal stress, associated to the direction perpendicular to the stylolite plane, which for such tectonic stylolites lies horizontally. Therefore the crossover-length has to be smaller in a horizontal section than in a vertical section (Eq. 3.3) using analytical considerations (Schmittbuhl et al. 2004).

In addition we studied the influence of inclined teeth and asperities on the scaling behavior of stylolites. Using synthetic 'slickolites' with various tilt angles we found that the evolving anisotropy is negligible and clearly different from the stress dependent anisotropy of the investigated samples. We thus conclude that the scaling anisotropy of tectonic stylolites is mainly defined by the 3D formation stress.

## 3.7. Appendix: Stress Calculation

### 3.7.1. Part I

In this appendix we will show how the tectonic stress ( $\sigma_1$ ) and the smaller in-plane stress component ( $\sigma_3$ ) can be calculated if the vertical stress component can be approximated using vertical loading conditions. According to equation (3.3) the vertical and horizontal crossovers ( $L_v$  and  $L_h$ ) can be calculated by (Schmittbuhl et al., 2004)

$$L_v = \frac{\gamma E}{\beta} \frac{1}{\sigma_m \sigma_{dv}} \quad L_h = \frac{\gamma E}{\beta} \frac{1}{\sigma_m \sigma_{dh}} \quad (A1)$$

where  $E$  is the Young's Modulus,  $\gamma$  is the solid-fluid interfacial energy,  $\beta = \nu(1-2\nu)/\pi$  is a dimensionless constant with  $\nu$  the Poisson's ratio,  $\sigma_m$  and  $\sigma_{dv/h}$  are the mean and differential stresses respectively. Since the mean stress is the same for both directions we can reformulate equation A1 to

$$\sigma_m = \frac{\gamma E}{\beta} \frac{1}{L_v \sigma_{dv}}, \quad \sigma_m = \frac{\gamma E}{\beta} \frac{1}{L_h \sigma_{dh}} \quad (A2)$$

and join both equations so that

$$L_v \sigma_{dv} = L_h \sigma_{dh}. \quad (A3)$$

If we now define the differential stresses using the main principal stress components (as  $\sigma_{dv} = \sigma_{yy} - \sigma_{zz}$  and

$\sigma_{dh} = \sigma_{yy} - \sigma_{xx}$ ) equation A3 becomes

$$\frac{L_h}{L_v} = \frac{\sigma_{yy} - \sigma_{zz}}{\sigma_{yy} - \sigma_{xx}} \quad (A4)$$

and solving for the  $xx$  component

$$\begin{aligned} \sigma_{yy} - \sigma_{xx} &= \frac{L_v}{L_h} (\sigma_{yy} - \sigma_{zz}), \\ \sigma_{xx} &= \sigma_{yy} - \frac{L_v}{L_h} (\sigma_{yy} - \sigma_{zz}) = \sigma_{yy} - \frac{L_v}{L_h} \sigma_{yy} + \frac{L_v}{L_h} \sigma_{zz} \end{aligned} \quad (A5).$$

### 3.7.2. Part II

For simplification we substitute all material parameters of Equation 4 which are assumed to be constant, according to

$$a = \frac{\gamma E}{\beta}.$$

Then we use equation 4 for the horizontal cross-over

$$L_h = a \frac{1}{\sigma_m \sigma_{dh}}$$

or



$$\sigma_m \sigma_{dh} = \frac{\sigma_{xx} + \sigma_{yy} + \sigma_{zz}}{3} (\sigma_{yy} - \sigma_{xx}) = \frac{a}{L_h}$$

and

$$(\sigma_{xx} + \sigma_{yy} + \sigma_{zz})(\sigma_{yy} - \sigma_{xx}) = 3 \frac{a}{L_h} \quad (A6)$$

with the main principal stress components.

Now we include equation A5 into equation A6 and solve for  $\sigma_{yy}$

$$\left( 2\sigma_{yy} + \sigma_{zz} - \sigma_{yy} \frac{L_v}{L_h} + \sigma_{zz} \frac{L_v}{L_h} \right) \left( \sigma_{yy} \frac{L_v}{L_h} - \sigma_{zz} \frac{L_v}{L_h} \right) = 3 \frac{a}{L_h} \quad (A7)$$

and multiplying the components gives

$$2\sigma_{yy}^2 \frac{L_v}{L_h} - \sigma_{yy}^2 \left( \frac{L_v}{L_h} \right)^2 + 2\sigma_{yy}\sigma_{zz} \left( \frac{L_v}{L_h} \right)^2 - \sigma_{yy}\sigma_{zz} \frac{L_v}{L_h} - \sigma_{zz}^2 \frac{L_v}{L_h} - \sigma_{zz}^2 \left( \frac{L_v}{L_h} \right)^2 - 3 \frac{a}{L_h} = 0. \quad (A8)$$

Rearranging equation A8 in order to solve a binomial formula gives

$$\sigma_{yy}^2 + \sigma_{yy} \frac{2\sigma_{zz} \left( \frac{L_v}{L_h} \right)^2 - \sigma_{zz} \frac{L_v}{L_h} - \sigma_{zz}^2 \frac{L_v}{L_h} - \sigma_{zz}^2 \left( \frac{L_v}{L_h} \right)^2 - 3 \frac{a}{L_h}}{2 \frac{L_v}{L_h} - \left( \frac{L_v}{L_h} \right)^2} = 0 \quad (A9)$$

and the solution of the binomial formula is then

$$\sigma_{yy1,2} = -0.5 \frac{2\sigma_{zz} \left( \frac{L_v}{L_h} \right)^2 - \sigma_{zz} \frac{L_v}{L_h}}{2 \frac{L_v}{L_h} - \left( \frac{L_v}{L_h} \right)^2} \pm \sqrt{0.25 \left( \frac{2\sigma_{zz} \left( \frac{L_v}{L_h} \right)^2 - \sigma_{zz} \frac{L_v}{L_h}}{2 \frac{L_v}{L_h} - \left( \frac{L_v}{L_h} \right)^2} \right)^2 - \left( \frac{-\sigma_{zz}^2 \frac{L_v}{L_h} - \sigma_{zz}^2 \left( \frac{L_v}{L_h} \right)^2 - 3 \frac{a}{L_h}}{2 \frac{L_v}{L_h} - \left( \frac{L_v}{L_h} \right)^2} \right)} \quad (A10).$$

$\sigma_{xx}$  is than

$$\sigma_{xx} = \sigma_{yy} - \frac{L_v}{L_h} \sigma_{yy} + \frac{L_v}{L_h} \sigma_{zz}. \quad (A11)$$

### 3.8. References

- Barabasi, A. L. & Stanley, H. E. 1995. Fractal concepts in surface growth. Cambridge University Press.
- Bretz, J. H. 1940. Solution cavities in the Joliet limestone of northeastern Illinois. *Journal of Geology* 48(4), 337-384.
- Brouste, A., Renard, F., Gratier, J. P. & Schmittbuhl, J. 2007. Variety of stylolites' morphologies and statistical characterization of the amount of heterogeneities in the rock. *Journal of Structural Geology* 29(3), 422-434.
- Buxton, T. M. & Sibley, D. F. 1981. Pressure Solution Features in a Shallow Buried Limestone. *Journal of Sedimentary Petrology* 51(1), 19-26.
- Candela, T., Renard, F., Bouchon, M., Brouste, A., Marsan, D., Schmittbuhl, J. & Voisin, C. 2009. Characterization of fault roughness at various scales: Implications of three-dimensional high resolution topography measurements. *Pure and Applied Geophysics*.
- Capote, R., Munoz, J. A., Simon, J. L., Liesa, C. L. & Arlegui, L. E. 2002. The Alpine system north of the Betic Cordillera. In: *The geology of Spain* (edited by Gibbons, W. & Moreno, T.). Geological Society of London, London, 632.
- Casas, A. M., Casas, A., Perez, A., Tena, S., Barrier, L., Gapais, D. & Nalpas, T. 2000. Syn-tectonic sedimentation and thrust-and-fold kinematics at the intra-mountain Montalban Basin (northern Iberian Chain, Spain). *Geodinamica Acta* 13(1), 1-17.
- Cooley, J. W. & Tukey, J. W. 1965. An Algorithm for Machine Calculation of Complex Fourier Series. *Mathematics of Computation* 19(90), 297-&.
- Drummond, C. N. & Sexton, D. N. 1998. Fractal structure of stylolites. *Journal of Sedimentary Research* 68(1), 8-10.
- Dunnington, H. V. 1954. Stylolite development post-dates rock induration. *Journal of sedimentary Petrology* 24(1), 27-49.
- Ebner, M., Koehn, D., Toussaint, R. & Renard, F. 2009a. The influence of rock heterogeneity on the scaling properties of simulated and natural stylolites. *Journal of Structural Geology* 31(1), 72-82.
- Ebner, M., Koehn, D., Toussaint, R., Renard, F. & Schmittbuhl, J. 2009b. Stress sensitivity of stylolite morphology. *Earth and Planetary Science Letters*(277), 394-398.
- Etzold, A., Franz, M. & Villinger, E. 1996. Schwäbische Alb - Stratigraphie, Tektonik, Vulkanismus, Karsthydrogeologie. *Z. geol. Wiss.* 24(1/2), 175-215.
- Geyer, O. F. & Gwinner, M. P. 1991. *Geologie von Baden-Württemberg*. Schweizerbart'sche Verlagsbuchhandlung, Stuttgart.
- Goshtasby, A. 1986. Piecewise Linear Mapping Functions for Image Registration. *Pattern Recognition* 19(6), 459-466.
- Goshtasby, A. 1988. Image Registration by Local Approximation Methods. *Image and Vision Computing* 6(4), 255-261.

- Gratier, J. P., Muquet, L., Hassani, R. & Renard, F. 2005. Experimental microstylolites in quartz and modeled application to natural stylolitic structures. *Journal of Structural Geology* 27(1), 89-100.
- Guzzetta, G. 1984. Kinematics of Stylolite Formation and Physics of the Pressure-Solution Process. *Tectonophysics* 101(3-4), 383-394.
- Heald, M. T. 1955. Stylolites in Sandstones. *Journal of Geology* 63(2), 101-114.
- Karcz, Z. & Scholz, C. H. 2003. The fractal geometry of some stylolites from the Calcare Massiccio Formation, Italy. *Journal of Structural Geology* 25(8), 1301-1316.
- Kley, J. & Voigt, T. 2008. Late Cretaceous intraplate thrusting in central Europe: Effect of Africa-Iberia-Europe convergence, not Alpine collision. *Geology* 36(11), 839-842.
- Koehn, D., Renard, F., Toussaint, R. & Passchier, C. W. 2007. Growth of stylolite teeth patterns depending on normal stress and finite compaction. *Earth and Planetary Science Letters* 257(3-4), 582-595.
- Liesa, C. L. & Simón, J. L. Evolution of intraplate stress fields under multiple remote compressions: The case of the Iberian Chain (NE Spain). *Tectonophysics* In Press, Corrected Proof.
- Meheust, Y. & Schmittbuhl, J. 2001. Flow Enhancement of a Rough Fracture. *Geophys. Res. Lett.* 27.
- Park, W. C. & Schot, E. H. 1968. Stylolites: their nature and origin. *Journal of sedimentary Petrology* 38(1), 175-191.
- Press, W., H., Teukolsky, S., A., Vetterling, W., T. & Flannery, B., P. . 2007. *Numerical Recipes. The Art of Scientific Computing.* Cambridge University Press.
- Railsback, B. L. & Andrews, L. M. 1995. Tectonic stylolites in the 'undeformed' Cumberland Plateau of southern Tennessee. *Journal of Structural Geology* 17(6), 911-915.
- Railsback, L. B. 1993. Lithologic Controls on Morphology of Pressure-Dissolution Surfaces (Stylolites and Dissolution Seams) in Paleozoic Carbonate Rocks from the Mideastern United-States. *Journal of Sedimentary Research* 63(3), 513-522.
- Renard, F., Schmittbuhl, J., Gratier, J. P., Meakin, P. & Merino, E. 2004. Three-dimensional roughness of stylolites in limestones. *Journal of Geophysical Research-Solid Earth* 109(B3), -.
- Renard, F., Voisin, C., Marsan, D. & Schmittbuhl, J. 2006. High resolution 3D laser scanner measurements of a strike-slip fault quantify its morphological anisotropy at all scales. *Geophysical Research Letters* 33(4), -.
- Rutter, E. H. 1983. Pressure solution in nature, theory and experiment. *Journal of the Geological Society of London* 140(5), 725-740.
- Schmittbuhl, J., Vilotte, J. P. & Roux, S. 1995. Reliability of Self-Affine Measurements. *Physical Review E* 51(1), 131-147.
- Schmittbuhl, J., Renard, F., Gratier, J. P. & Toussaint, R. 2004. Roughness of stylolites: Implications of 3D high resolution topography measurements. *Physical Review Letters* 93(23), -.
- Schmittbuhl, J., Steyer, A., Jouniaux, L. & Toussaint, R. 2008. Fracture morphology and viscous transport. *International Journal of Rock Mechanics and Mining Sciences* 45(3), 422-430.

- Simon, J. L. 2007. Analysis of solution lineations in pebbles: Kinematical vs. dynamical approaches. *Tectonophysics* 445(3-4), 337-352.
- Simonsen, I., Vandembroucq, D. & Roux, S. 2000. Wave scattering from self-affine surfaces. *Physical Review E* 61(5), 5914.
- Stockdale, P. B. 1922. Stylolites: their nature and origin. *Indiana University Studies* 9, 1-97.
- Tada, R. & Siever, R. 1989. Pressure Solution during Diagenesis. *Annual Review of Earth and Planetary Sciences* 17, 89-118.
- Turcotte, D., L. 1997. *Fractals and Chaos in Geology and Geophysics*. Cambridge University Press, Cambridge.

## **4. The influence of localized pressure solution at & around stylolite interfaces: multi-scale quenched noise as roughness origin**

### **Abstract**

Rough pressure solution surfaces, like Stylolites, are one of the most evident deformation features in monomineralic rock-types. There is a general consensus that the development of these rough structures is a result of localized, stress enhanced dissolution of material along a fluid filled interface, but little is known on the initiation of this roughness. The aim of this article is to reveal the role of quenched noise i.e. heterogeneities initially present in the host-rock, on the initiation of this roughness. This should give insights on whether stylolite roughness is generated by a stress-induced instability or by the material disorder. We use a microstructural approach based on SEM/EBSD analysis combined with orientation contrast (OC) image analysis of stylolites in limestones. We found that stylolite roughness is induced by heterogeneities in the host rock (clay particles and detrital quartz grains in our case). In addition, around mature stylolite interfaces matrix modifications occur, which can be assigned to the compaction along the stylolite. The grain size decreases by 15% and a preexisting shape- and lattice-preferred orientation (SPO, LPO) are significantly modified in the vicinity of the stylolite. The results presented here imply that localized pressure solution along stylolites is not necessarily restricted to the actual interface but influences the adjacent matrix. Additionally the reported heterogeneity data might serve as a quantitative basis for elaborate numerical models.

### **4.1. Introduction**

Stylolites are localized pressure solution features distinguished by a characteristic multi-scale roughness that spans several orders of magnitude ranging from serrated grain contacts at the micron-scale up to decimeter-scale roughness amplitudes. The intriguing morphological characteristics of pressure solution surfaces have been the main focus of attention for many qualitative studies (Stockdale 1922, Dunnington 1954, Heald 1955, Park & Schot 1968, Alvarez et al. 1978, Buxton & Sibley 1981, Guzzetta 1984, Bayly 1986, Bathurst 1987), which in turn lead to more quantitative approaches (Railsback 1993, Andrews & Railsback 1997). In the last decade many workers employed statistical tools aiming to describe stylolite roughness in terms of fractal geometry showing that stylolites exhibit a fractal scaling over several orders of magnitude (Drummond & Sexton 1998, Karcz & Scholz 2003). Investigations of the 3D

morphology of natural stylolites in limestones (Renard et al. 2004, Schmittbuhl et al. 2004, Brouste et al. 2007, Ebner et al. 2009a), experimentally generated micro-stylolites (Gratier et al. 2005) and numerical simulations (Koehn et al. 2007, Ebner et al. 2009b) demonstrated that stylolite roughness reveals two self-affine scaling invariances, which are separated by a characteristic crossover-length at the millimeter scale. These scaling regimes have distinct Hurst or roughness exponents with 1.1 and 0.5 for small and large scales, respectively, which enable to describe the roughness of the entire surface in an unambiguous and quantitative fashion. It is important to notice that quasi universal scaling exponents were reported although bedding parallel stylolites from various different locations and lithological composition were investigated (Renard et al. 2004, Schmittbuhl et al. 2004, Brouste et al. 2007, Ebner et al. 2009a).

In contrary Railsback (1993) and Andrews and Railsback (1997) showed that the morphological appearance and/or abundance of stylolites changes with the gross lithology of the host rock. In addition the amount and intensity of dissolution seams was reported to correlate with the clay content in limestones and marls (Alvarez et al. 1978, Marshak & Engelder 1985). Nevertheless the cause for the roughness formation of both bedding parallel and tectonic (i.e. bedding normal) stylolites remains unclear.

Based on field observations, microstructural investigations, numerical and analytical considerations two main concepts for the roughening of stylolites prevail. In the first concept (termed *instability concept* in the following), a stress induced roughening instability exists along an initially flat solid-solid interface (Angheluta et al. 2008) or solid-fluid-solid interface (Bonnetier et al. 2009). Although the works of Angheluta et al. (2008) and Bonnetier et al. (2009) differ significantly, the roughening instability is induced by elastic stresses acting normal on the interface in both cases. In the second concept (Renard et al. 2004, Schmittbuhl et al. 2004, Koehn et al. 2007, Ebner et al. 2009b), the quenched noise, i.e. heterogeneities initially present in the host rock that remain constant over time and thus during deformation, is the destabilizing term responsible for roughening of the interface (and therefore termed *heterogeneity concept*). It is either surface or elastic energy which acts against these so-called pinning particles in the heterogeneity concept as a stabilizing term on small and large length-scales, respectively. It is therefore important to note that both concepts differ fundamentally, since in the first concept the applied external stress causes the roughening, whereas in the second concept the heterogeneities in the material induce the roughening, due to different dissolution rates, and the normal stress balances the effect of the roughening. Numerical simulations based on the heterogeneity concept show that it is capable to fully reproduce the complex scaling observed on natural stylolites (Koehn et al. 2007, Ebner et al. 2009b). In addition the simulations reveal that the exact composition, amount and size of the heterogeneities introduced in the system does not modify the scaling of the developing stylolite morphology significantly. On the other hand, the instability concept, while able to explain the roughening of an initially flat interface due to a stress induced instability, fails to reproduce natural stylolitic morphologies (Angheluta et al. 2008) and utilizes boundary conditions which are questionable for real rocks (Bonnetier et al. 2009).

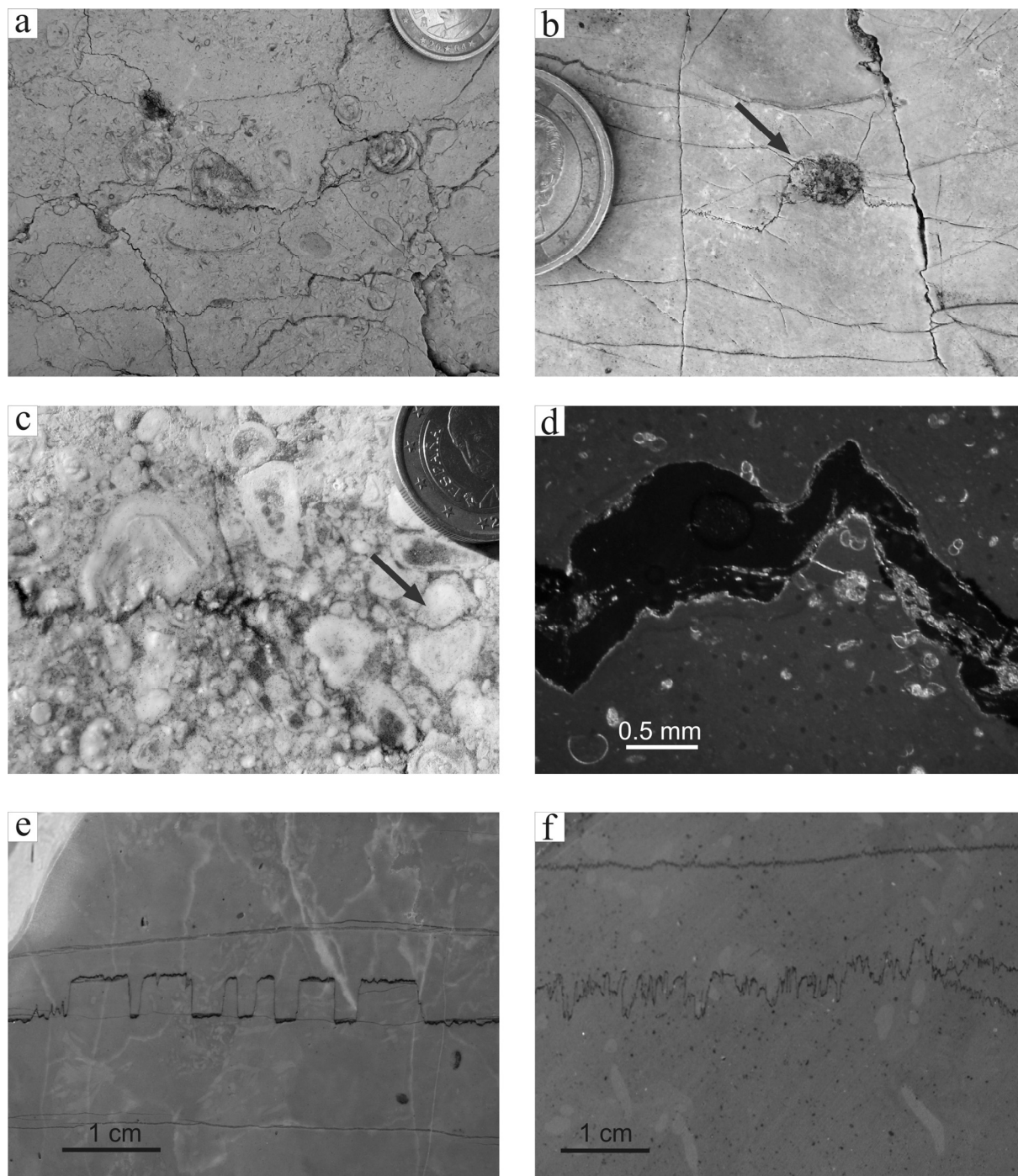


**Figure 4.1** Photographs of stylolites in limestones and their relationship to a macro and microscopic pinning components. **(a) – (d)** Biogenic clasts, i.e. mollusks, foraminifera, which often do not register in roughness. Particles which do register in the roughness are indicated with an arrow. **(e)** Stylolite which is inhibited by a horizontal calcite vein and thus forms a columnar morphology. **(f)** Small clay particles in the matrix around a stylolite. Note that macroscopic clay particles are larger than the smallest amplitudes of the stylolite.

Models using heterogeneities as roughness origin have successfully generated synthetic surfaces in numerical simulations and analytical considerations that resemble the scaling features of natural stylolites (Renard et al. 2004, Schmittbuhl et al. 2004, Gratier et al. 2005, Brouste et al. 2007, Koehn et al. 2007, Ebner et al. 2009b). Although the importance of material disorder and composition on the stylolite morphology has been stressed in previous contributions investigating the rock hosting the stylolite

(Railsback 1993, Andrews & Railsback 1997), so far no study quantitatively characterized the composition of the quenched disorder that initiates the distinct roughness of stylolite interfaces. This is indeed a difficult task in the field (Fig. 4.1) since pinning particles only rarely consist of macroscopically distinguishable rock-fragments (Fig. 4.1 b) or bioclasts, but often do not register in the roughness scaling macroscopically.

In the present contribution we report direct evidence based on SEM and EBSD investigations of multi-scale quenched noise in limestones as an agent for the formation of stylolite roughness. In addition we describe microstructures of the matrix around mature stylolite interfaces that accumulated considerable amount of strain.

## 4.2. Dataset and Methods

The following chapter provides a brief summary of the geological context of the sampling localities and a short description of the samples in the first part. In addition, the working conditions for the SEM and EBSD analysis are reported in the second part of this chapter. Procedures of data analysis are reported in chapter 4.3 in combination with the results.

### 4.2.1. Stylolite dataset

In the current work we report the microstructural analysis of 5 limestone samples from three different locations and geological settings. The oriented samples were selected to cover the following range of stylolite characteristics: (i) initial to mature interfaces; (ii) different rock-types hosting the stylolites e.g. Mudstone to Packstone and (iii) bedding parallel and tectonic stylolites.

The first locality, Cirque de Navacelles (Larzac), is located 50 km NW of Montpellier in southern France (*UTM 31T E 0539704 m; N 4860040 m*), exposing a flat-lying upper Jurassic limestone succession (Bodou 1976, Rispoli 1981). The outcrop is part of an external shelf deposit of the Vocontian Basin and consists mainly of fine-grained mudstones and wackestones. The top part of the succession is made up of massive Kimmeridgian limestones, whereas the lower part exposes well-bedded Oxfordian mudstones where a slight secondary dolomitization is reported (Bodou 1976). Although both sub horizontal bedding parallel and vertical tectonic stylolites, due to Eocene N–S directed compression from the Pyrenean, can be found in the area (Rispoli 1981, Petit & Mattauer 1995, Ebner et al. 2009a), only bedding parallel stylolites were used for this study. The lithology of both investigated samples (N2 & Nava N7) can be classified as well-bedded Oxfordian mudstone.

The second investigated locality is sited 10 km south of Tübingen (Swabian Alb, southern Germany) and comprises upper Jurassic (Oxfordian to Kimmeridgian) limestones (Geyer & Gwinner 1991). The Swabian Alb of southern Germany forms a region of flat-lying mainly marine Jurassic deposits. The investigated outcrop (*UTM 32U; E 0521508 m; N 5370938 m*) is made up of bedded Oxfordian limestones



(Geyer & Gwinner 1991, Etzold et al. 1996), with a (sub-) horizontal orientation of the bedding, slightly dipping ( $<5^\circ$ ) towards the SE. The investigated sample (*Sa7b/1*) exhibits a vertical set of tectonic stylolites, which trends WNW-ESE with teeth (amplitudes of up to 1.2 cm) pointing parallel to the surface normal direction, hence recording a NNE-SSW compression. This NNE-SSW directed shortening is related to late Cretaceous compression in central Europe (Geyer & Gwinner 1991, Kley & Voigt 2008). The stylolite itself is hosted in a fine-grained calcite mudstone.

The third locality, Gorge due Nan, is situated 20 km East of Grenoble (SE France) in the Vercors Plateau. The surrounding of the examined outcrop (*UTM 31TE 0690591 m; N 5004233 m*) belongs to the so-called Urgonian carbonate platform (Moss & Tucker 1995) mid-Cretaceous in age, upper Barremian to lower Aptian (Arnaud-Vanneau & Arnaud 1990). The stratigraphy of the Urgonian platform consists of a Barremian bioclastic limestone Formation (Borne and Glandasse Formations) in the lower part and in the upper part of a upper Barremian to mid-Aptian Urgonian Limestone Formation (Arnaud-Vanneau & Arnaud 1990, Moss & Tucker 1995). The sample (Nan1) investigated in this study belongs to the lower Orbitolina Beds (Apt) and represents a packstone-grainstone with grains consisting of foraminifera and ooids.

#### 4.2.2. Methodology (EBSD and OC settings)

For microstructural analysis all samples were investigated using optical and scanning electron microscopy (SEM) with electron backscatter diffraction (EBSD) coupled with forescatter orientation contrast (OC) imaging. Forescatter detectors provide orientation contrast and phase (atomic number /  $z$ ) contrast of samples (Prior et al. 1996, Prior et al. 1999). The analysis was performed on polished thin-sections that remained uncoated. To reduce charging of conductive material during the analysis we applied a conductive double sided adhesive carbon tape around the investigated thin-sections. The EBSD and OC data were collected at Stockholm University with a *Phillips XL-30 FEG-ESEM* in combination with a *Nordlys* detector and the *HKL Channel5* acquisition software (Flamenco). The samples were oriented with a high tilt angle of  $70^\circ$  and the SEM was operating at 20 kV and a 10 nA current at a working distance of 20 mm. To analyze the resulting electron back scatter pattern (EBSP) we set the indexing limit to a band detection of 6 (min) -7 (max) of 72 [hkl] theoretical reflectors. The acquisition speed was between 0.1 and 0.03 seconds/measurement point (sample *N7* 0.095s/pt; *Nan1* 0.0047s/pt & *Sa7b* 0.003s/pt). The EBSD maps were constructed from a step size of 0.2  $\mu\text{m}$  (*Nan1*) and 0.4  $\mu\text{m}$  (*N7*, *Sa7b*) and usually contain a minimum of some several hundred up to some 70000 grains. The average indexing was around 50-70%. Using the *HKL Channel5* analysis software we processed the raw data by replacing non-indexed pixels with more than 5 neighbors with an orientation of the neighboring pixels. In addition we removed wild spikes i.e. isolated pixels with a  $60^\circ$  misorientation with respect to its neighbors were considered misindexed, and again replaced them with an orientation of the neighboring pixels. For grain reconstruction we use the *HKL Channel5* software, which combines individual EBSD measurements into a grain if neighboring measurements have a crystal lattice misorientation which is smaller than a user

defined value. We define boundaries to have misorientations of  $>2^\circ$  for subgrain boundaries and  $>10^\circ$  for high angle grain boundaries (these values are used in the following chapters).

### 4.3. Data Analysis & Results

The results of our data analysis are grouped generically according to the major findings of the noise around initial and mature interfaces. First we describe observational evidence in individual subchapters (chapter 4.3.1 and 4.3.2), which we attempt to corroborate by a more quantitative analysis of the matrix (including crystallographic orientation, grain size and shape analysis) and the identified quenched disorder (grain size and shape analysis). In the third part (chapter 4.3.3) we focus on matrix adjustments around a mature pressure solution interface of a tectonic stylolite.

#### 4.3.1. Noise around initial interfaces

Initial interfaces, which are here defined as interfaces that have not developed a continuous residual layer i.e. a through going clay parting, are considered crucial to understand the origin of the roughness along stylolite interfaces. As a matter of fact it is also a prerequisite for the understanding of more complex and more mature stylolite interfaces which we will examine later in this chapter. Figure 4.2 shows a series of orientation contrast (OC) images of sample *Nan1* which all contain an initial microstylolite running roughly E-W in all images. The gray matrix is made up of calcite crystals. Individual grains can be distinguished by different gray-scale levels which reflect a change of the lattice orientation between adjacent grains (Prior et al. 1996). The bright spots in the OC image are clay minerals of various sizes. Only limited amount of charging (i.e. white halos around grains with a high relief) occurs along single grains. The microstylolite itself represents a thin black line (Fig. 4.2 a), i.e. a depression which is not hit by the electron current due to the high sample tilt.

The most obvious observation is the alignment of clay particles atop pronounced asperities i.e. on the convex side along these microstylolites (indicated by white arrows in Fig. 4.2 a-c). Although there is a roughness along Calcite -Calcite contacts (e.g. Fig. 4.2 a), each of the most prominent asperities along the interface is occupied with a clay particle. Looking at slightly higher strains (Fig. 4.2 d-f), increasingly more clay particles align along the stylolite interface. In addition the amplitude of roughness is large compared to the grain size of the clay particles. The difference in calcite grain size (compare Fig. 4.2 d & f) is the expression of sparitic cement filling the pore space of this grainstone and fine-grained biogenic calcite in bioclasts and onkoids. Localized pressure solution can either occur along grain size variation (Fig. 4.2 d) or within zones of homogeneous grain size (Fig. 4.2 e & f). Grain size variation is thus not a coercive prerequisite for stylolite formation.

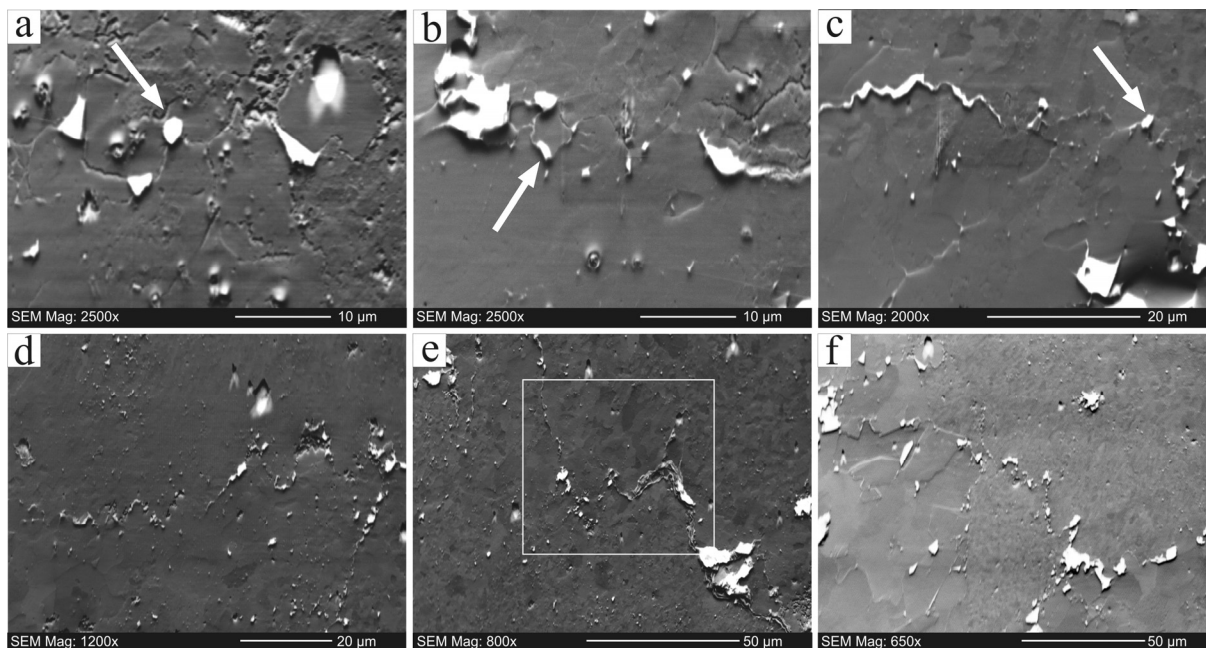


**Figure 4.2** Orientation contrast (OC) images of initial stylolites in fine grained calcite limestones (sample Nan1). White spots resemble clay particles and the dark grain groundmass is calcite **(a) – (c)** Clay particles are located at the topmost part of the asperities along microstylolites (white arrow). **(d) – (f)** Microstylolites which have accumulated more residual clay and thus indicate higher strains. The white frame in e) indicates the area analyzed with EBSD shown in Figure 4.4 a. Note that microstylolites trend E-W in all images. See text for detailed description and explanation.

In addition, we noticed that also the grain size of the so-called pinning particles, i.e. the clay particles, changes along individual microstylolites (Fig. 4.2 f). In the regions of sparitic calcite cement the grain size of the clay minerals is usually bigger than in the fine-grained bioclastic domains where the particle-size of the clay is smaller.

The grain size analysis of calcite around the stylolite and in the host rock is based on EBSD measurements using the *Channel5 bkl* processing software for grain reconstruction (see above). In addition to the grain size we analyzed the grain shape of the reconstructed grains obtained from EBSD analysis. The results of the grain size and shape analysis of sample *Nan1* (number of grains: 1676) are shown in Figure 4.3 a. This Figure shows the relative frequencies or grain area [ $\mu\text{m}^2$ ] and circle equivalent diameter [ $\mu\text{m}$ ], i.e. the diameter of a circle that corresponds to the grain area, in the top row. In the following we will use the grain area as the characteristic feature for the grain size. The mean (arithmetic) grain-area is  $3.1 \mu\text{m}^2$  with a standard deviation of  $\pm 9.6 \mu\text{m}^2$ . It was pointed out that a grain size distribution that resembles the one shown in Figure 4.3 is better represented by the geometric mean if the geometric mean equals (or is very close to) the natural logarithm of the median of the grain area (Mingard et al. 2007). Since this is the case, we will use the geometric mean  $1.0 \mu\text{m}^2$  to represent the mean grain area.

To characterize the grain shape we utilize best fitting ellipses calculated of individual grains. We calculate the aspect ratio  $a/b$  with  $a$  and  $b$  being the major and minor axis of the ellipse and  $\theta$ , the counterclockwise angle of the map base and the long ellipse axis  $a$ . For the grain shape analysis we only use grains with an area  $> 1.5 \mu\text{m}^2$ . This procedure allows reducing artifacts introduced by the square size of the grid and a resolution of  $0.4 \mu\text{m}$ . Otherwise the resulting histogram is strongly biased since bins in

the region of  $45^\circ$ ,  $90^\circ$  and  $135^\circ$  are overrepresented. Arithmetic mean (median) of the aspect ratio is 1.85 (1.73) and  $\theta$  is  $76^\circ$  ( $70^\circ$ ). This moderate shape preferred orientation with grains aligned in a direction  $76^\circ$  from the map base is not related to pressure solution (which should orient the grains parallel to the base i.e.  $\theta$  of  $0^\circ$  or  $180^\circ$ ) but can be attributed to a preferred radial growth direction in spherulitic calcite particles. Figure 4.3 b shows the same results for sample N7 (number of grains: 9583) mean (arithmetic) grain area is  $2.0 \mu\text{m}^2$  with a standard deviation of  $\pm 13.9 \mu\text{m}^2$  and a geometric mean grain area of  $0.35 \mu\text{m}^2$ , and an arithmetic mean (median) of the aspect ratio is 1.72 (1.58) and  $\theta$  is  $89^\circ$  ( $88^\circ$ ).

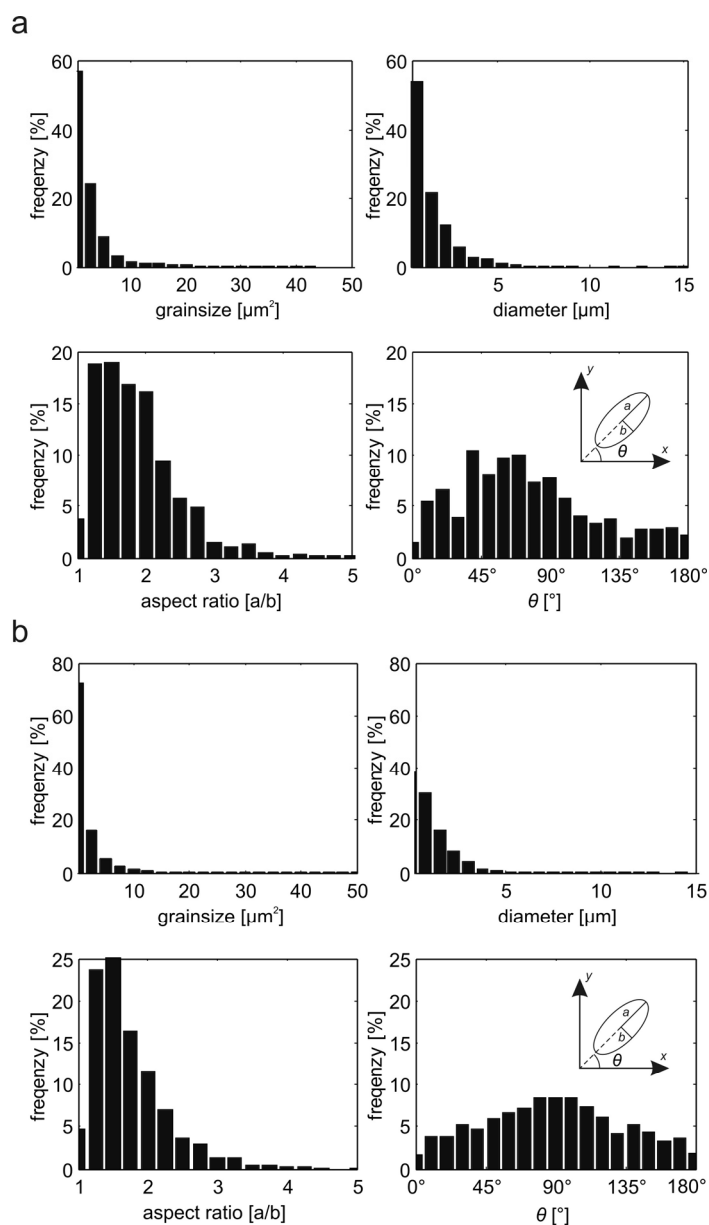


**Figure 4.3** Graphs showing relative frequencies of (crosssectional) *grain area* ( $\mu\text{m}^2$ ), *circle equivalent diameter* ( $\mu\text{m}$ ), *aspect ratio* ( $a/b$ ),  $\theta$  ( $^\circ$ ) from individual calcite grains reconstructed from EBSD measurements (compare text). Small inset shows how *aspect ratio* and  $\theta$  are calculated from best fitting ellipses of individual grains. Reference frame refers to the orientation of the EBSD map. Note that for *aspect ratio* and  $\theta$  only grains  $\geq 1.5 \mu\text{m}^2$ . **(a)** Sample Nan1, (number of grains 1676) mean grain area  $3.1 \mu\text{m}^2$ . **(b)** Sample N7, (number of grains 9582) mean grain area  $2.1 \mu\text{m}^2$ .

Analysis of the lattice preferred orientation (LPO) of calcite around pressure solution surfaces utilizes EBSD measurements. The LPO data of the samples Nan1 (Fig. 4.4 a; corresponds to the area indicated by the white frame in Fig. 4.2 e) and N7 (Fig. 4.4 b) is represented in equal area upper hemisphere pole figures of the  $c\{0001\}$ ,  $r\{10-14\}$ ,  $a\{11-20\}$  and  $f\{01-12\}$  poles. For sample Nan1 the stylolitic compaction direction is roughly N-S (in the investigated map; compare Fig. 4.2) and for sample N7 the compaction direction is E-W. The pole figures of Nan1 do not show a preferred orientation of any of the shown crystal planes that could be attributed to this compaction. But distinct maxima of the c-poles correspond to preferred orientation of biogenetic calcite. Sample N7 shows a very weak LPO, which defines a great circle normal to the compaction direction for the c-poles. The stylolite compaction direction of N7 is parallel to the sedimentary compaction imposed by the layer normal overburden.

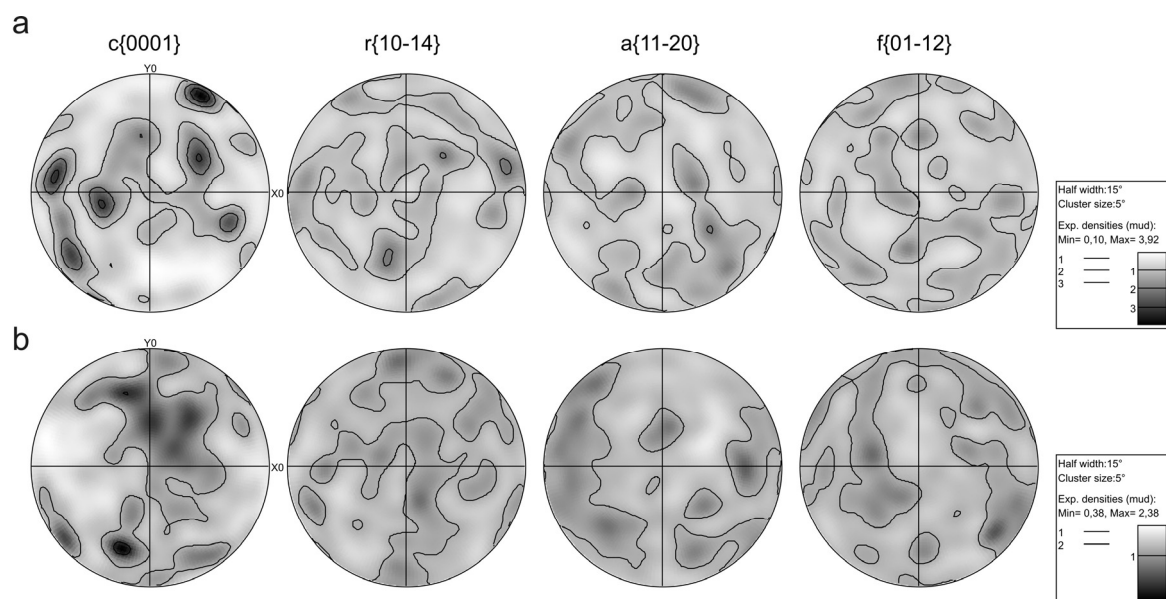


**Figure 4.4** Lattice preferred orientation (LPO) of calcite from EBSD analysis. Contoured pole figures of  $c\{0001\}$ -,  $f\{10-14\}$ -,  $a\{11-20\}$ - and  $r\{01-12\}$ -poles in equal area (upper hemisphere) projection. Contouring parameters: half width  $15^\circ$  and cluster size  $5^\circ$ . **(a)** Sample Nan1 compare Figure 4.2 e, (compaction direction N-S); **(b)** Sample N7 (compaction direction E-W). Both samples do not show a LPO which can be attributed to the compaction direction.

In a third step we will quantitatively analyze the quenched noise i.e. the heterogeneities initially present in the host-rock, which we have identified qualitatively (see above). We observed that the clay particles distributed in the host-rock are sites where asperities along the stylolite interface form primarily (Fig. 4.2). We will thus analyze the grain size, shape and distribution of these clay particles in the vicinity of stylolites with a digital image analysis approach that is widely used (Panozzo 1983, Heilbronner 1992, Heilbronner & Keulen 2006). For that purpose we use the bitmaps of the OC-images (compare Fig. 4.2). These images suite our approach since the clay particles are bright white and easily separable from the medium gray-values of the calcite matrix. For the analysis we use the freely available public domain software *ImageJ*. In a first step the grayscale bitmaps were segmented by a gray level slicing, i.e. converting the images to BW-bitmaps by setting a threshold which separates the (white) clay from the (gray) calcite

(Fig. 4.5 a). The separated clay particles (dark spots in Fig. 4.5 a) are then analyzed with the built-in *Analyze Particles* routine in *ImageJ* and the resulting grain area, circle equivalent diameter, aspect ratio and  $\theta$  are shown in Figure 4.6. Sample *Nan1* (Fig. 4.6 a; analyzed area ca 26000  $\mu\text{m}^2$  with a pixel size of 0.125  $\mu\text{m}$ ) contains 3.0 % of clay material with an average area of 0.86  $\mu\text{m}^2$  (geometric mean 0.15  $\mu\text{m}^2$ ). Sample *N7* (Fig. 4.6 b; analyzed area ca 97000  $\mu\text{m}^2$  with a pixel size of 0.4  $\mu\text{m}$ ) contains 5.9 % of clay material with an average area of 1.0  $\mu\text{m}^2$  (geometric mean 0.25  $\mu\text{m}^2$ ). The orientation of the clay particles ( $\theta$ ) in both samples is strikingly similar compared to the orientation of the calcite grains (compare Fig. 4.3).

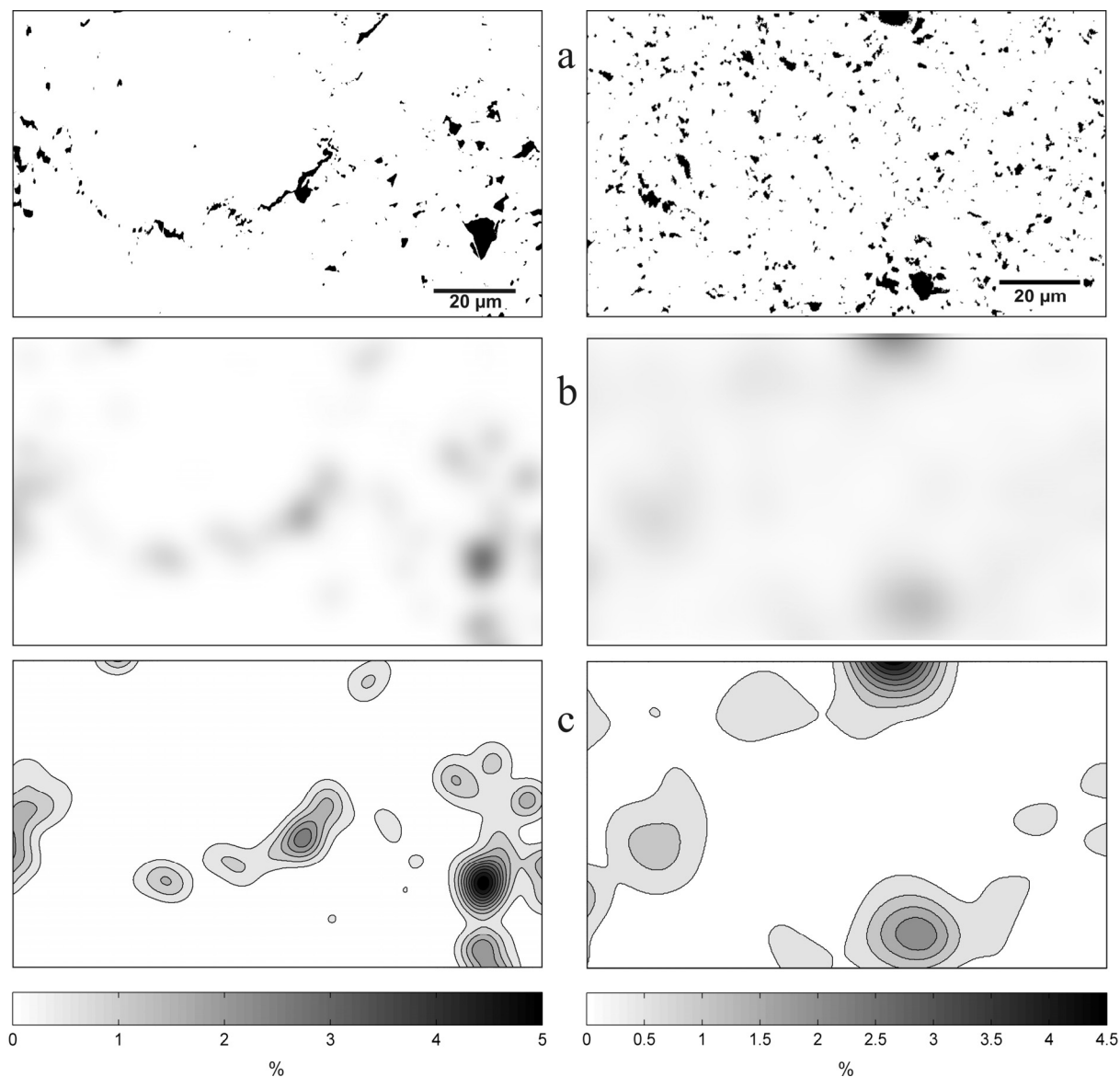


**Figure 4.5** Distribution analysis of clay particles in the host-rock surrounding the stylolite from samples *Nan1* (left column) and *N7* (right column). **(a)** Segmented clay particles (black dots) from OC images. **(b)** Grayscale image with a Gaussian filter (kernel size 25 pixels) applied to the BW-bitmap in **a** to produce a density image. **(c)** density image contoured for % clay particles. No significant relationship between the distribution of the particles and the compaction direction can be seen. Compaction direction is N-S for *Nan1* (left column) and E-W for *N7* (right column).

In addition we investigated the distribution of the clay particles following the approach of Heilbronner & Keulen (2006). The quenched noise density image (Fig. 4.5 b) is calculated by the use of a Gaussian filter with a square kernel size of 25 pixels. The Gaussian filter ensures that the average density of the filtered image (Fig. 4.5 b) is the same as that of the original bitmap (Fig. 4.5 a). The filter kernel size defines the level of detail. Figure 4.5 c shows the contours in % crosssectional area of clay particles. We do not observe a clear relationship with neither the compaction direction nor the calcite orientation for both samples (Nan1 & N7). This means that the heterogeneities (clay particles) are distributed quasi random.

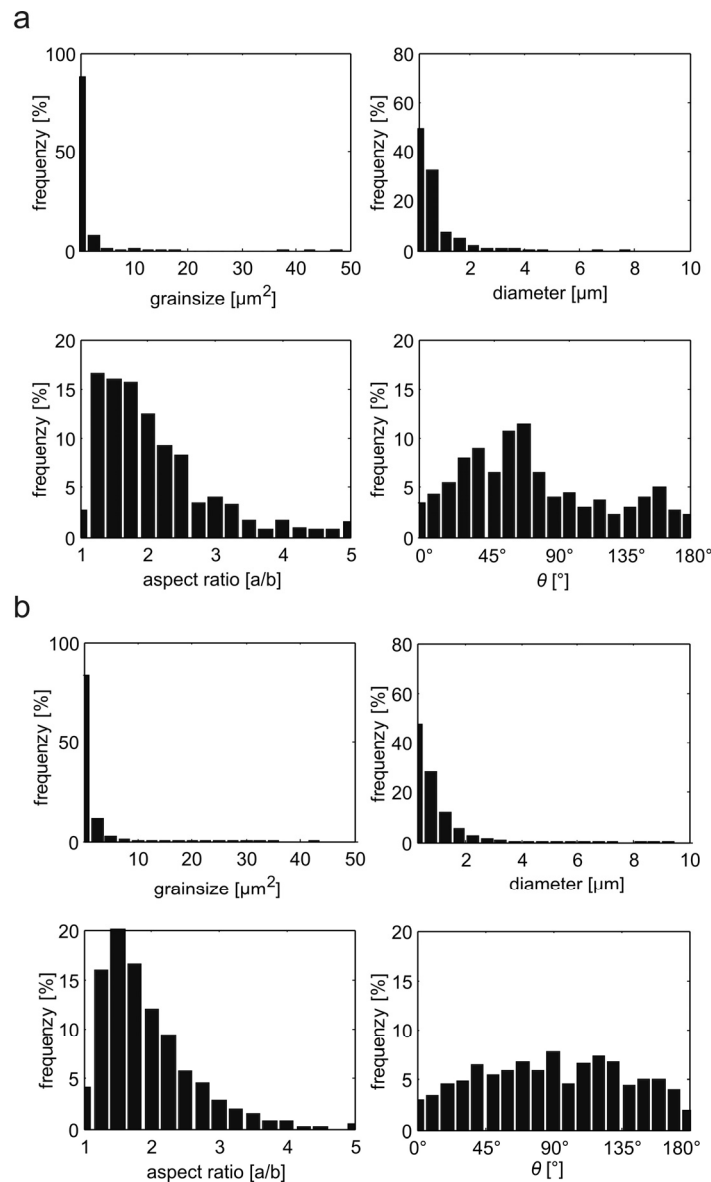


**Figure 4.6** Graphs showing relative frequencies of (crosssectional) *grain area* ( $\mu\text{m}^2$ ), *circle equivalent diameter* ( $\mu\text{m}$ ), *aspect ratio* ( $a/b$ ),  $\theta$  ( $^\circ$ ) of the individual clay particles analyzed with *ImageJ* similar to the data shown in Figure 4.3. **(a)** Nan1, 3.0 % of clay material with an average area of  $0.86 \mu\text{m}^2$  (geometric mean  $0.15 \mu\text{m}^2$  pixel size 0.15). **(b)** N7 contains 5.9 % of clay material with an average area of  $1.0 \mu\text{m}^2$  (geometric mean  $0.25 \mu\text{m}^2$  pixel size 0.4). Note that for the aspect ratio and  $\theta$  only grains with an area of more than 10 pixel are used.

### 4.3.2. Noise around mature interface

Mature stylolite interfaces, which have accumulated a continuous residual clay layer, generally exhibit higher strains and a more developed roughness (Koehn et al. 2007). Sample *Sa7b*, a fine-grained Jurassic limestone, contains a tectonic (bedding normal) stylolite which reveals a NNE-SSW directed compression for which a Cretaceous age is assumed (Kley & Voigt 2008). Figure 4.7 a shows OC image of a characteristic segment of the stylolite interface the dark gray groundmass is calcite and the bright white material is clay material/particles. Note that the accumulated residual clay layer has a thickness of up to 250  $\mu\text{m}$  measured parallel to the compaction direction. It is interesting to notice that the top boundary of the residual clay layer is defined by a rather smooth outline with straight segments connected by narrow bends, whereas the lower boundary is jagged with a characteristic columnar or teeth-like outline.

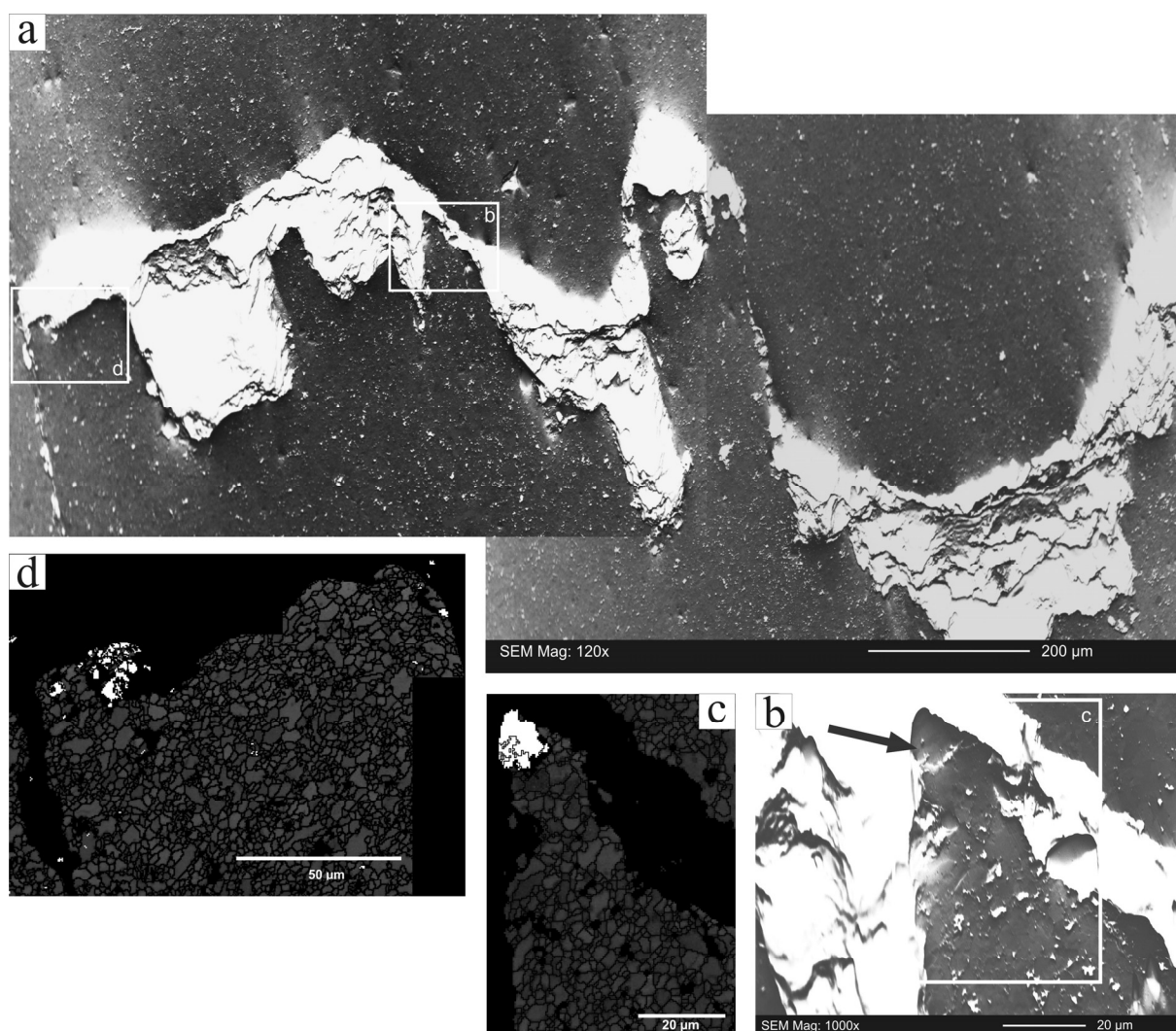


**Figure 4.7** OC images and EBSD maps of mature tectonic stylolite (sample *Sa7b*). **(a)** OC image showing a mature stylolite interface with significant thickness variation of the residual clay layer. Note that the topography changes from one side to the other. Frames indicated the enlargements in b & d. **(b)** Enlargement of panel a showing the indentation in the residual clay layer. Arrow points to a grain with a high relief indicative for a different resistance to polishing. **(c)** & **(d)** EBSD maps of the enlarged areas in panel a and b showing the grain outline and a color-coding for the material (grey – calcite; white – quartz). Quartz grains occupy all positions with a clear thickness variation of the residual clay layer.



This thickness variation can not be explained with the abrupt changes in abundance of clay particle variation along the interface (compare Fig. 4.7 a; examined below). In addition also across the interface a qualitative change in the distribution of the clay particles can not be observed. We noted that along these indentations along the interface grains with high relief can be found indicative of a different resistance to the polishing of the thin-section (Fig. 4.7 b; arrow). EBSD analysis of these areas (Fig. 4.7 c & d) revealed the presence of quartz grains at these indentations in the residual clay layers.

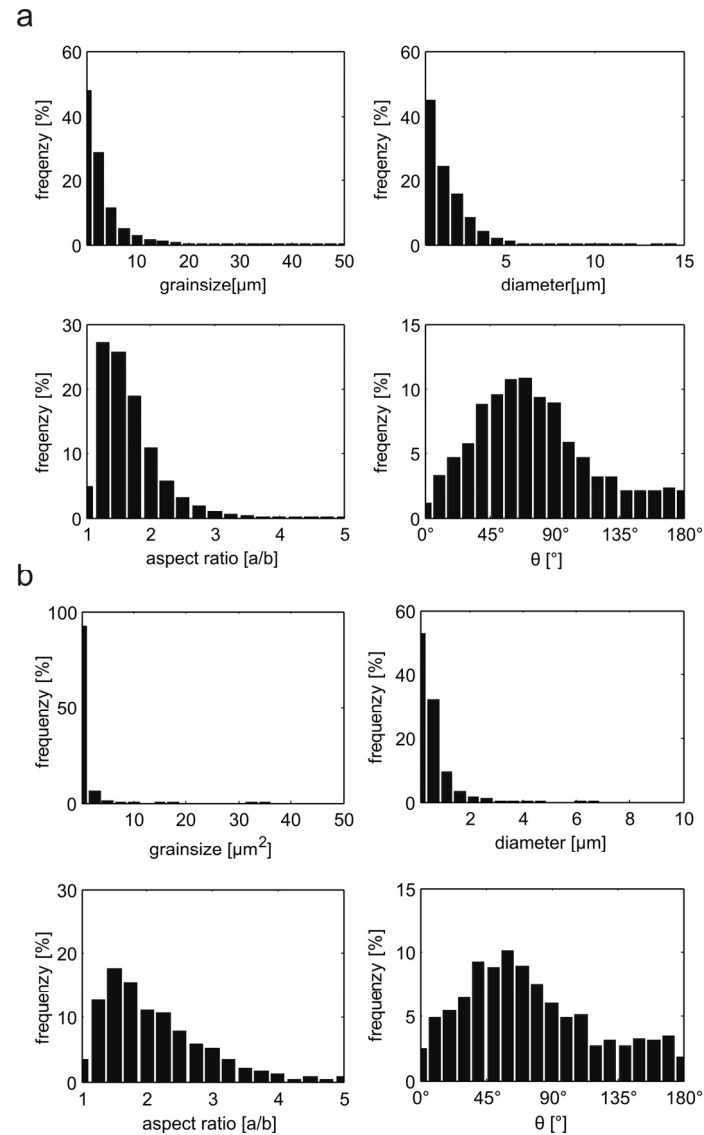


**Figure 4.8** Grain size and shape data set for the matrix around a mature stylolite interface (sample Sa7b) of **(a)** calcite and **(b)** clay particles (same representation as in Fig. 4.3 and Fig. 4.6). Note that the grain area of the clay particles is approximately one order of magnitude smaller than that of calcite (geometric mean of  $0.12\mu\text{m}^2$  and  $1.2\mu\text{m}^2$ , respectively). The aspect ratio of the clay particles is significantly higher than that of the calcite grains but the SPO ( $\theta$ ) of both fractions is quite similar.

The quantitative investigation of the mature stylolitic interface follows the same procedure as for initial interfaces but the LPO description is postponed to the next chapter. Figure 4.8 shows the quantitative data for the calcite grains (Fig. 4.8 a; 65000 analyzed grains), which is again based on the grain

reconstruction from the EBSD measurements, and the clay particles (Fig. 4.8 b; 3650 analyzed grains) based on image analysis of OC-images. Mean (arithmetic) grain area is  $2.9 \mu\text{m}^2$  (standard deviation of  $\pm 5.1 \mu\text{m}^2$ ) and a median of  $1.28 \mu\text{m}^2$  the geometric mean is  $1.2 \mu\text{m}^2$ . A clear shape preferred orientation of the long axis of the grains exist ( $\theta$ ) with a mean of  $76^\circ$  and a median value of  $70^\circ$ . The clay particles make up an area of 4.5 % and have a mean grain area of  $0.42 \mu\text{m}^2$  (standard deviation  $\pm 12.62$ ) and a geometric mean of  $0.12 \mu\text{m}^2$ . The mean aspect ratio aspect ratio is 2.1 and mean and median  $\theta$   $76^\circ$  and  $67^\circ$ , respectively.

Although there is a striking similarity between the SPO of calcite and clay particles, it is important to notice that the grain size of the clay particles is almost an order of magnitude smaller and has a higher aspect ratio than the calcite grains (probably owing to the fact that clay minerals are generally platy). We also analyzed the distribution of the clay particles (not shown) but did not observe a correlation with the thickness variation of the interface or compaction direction (compare above; Fig. 4.5). The quartz grains (identified by their EBSP) are analyzed using image analysis. The outlines of the quartz grains were digitized manually using *ImageJ* and the grain area was calculated following the method described above. We were able to identify 38 quartz grains in an area of  $860 \times 650 \mu\text{m}$  with an average area of  $106 \mu\text{m}^2$  (geometric mean  $62.1 \mu\text{m}^2$ ) per particle, which corresponds to 0.7 % of quartz in the sample.

### 4.3.3. Matrix adjustments around mature interfaces

To investigate the adjustments of the matrix around stylolite interfaces we examine a large map of Sample *Sa7b*. The selected map contains a stylolite peak with an amplitude of several hundred microns. Figure 4.9 a shows an OC image of the stylolite peak with a frame outlining the lower part of the EBSD map shown (Fig. 4.9 b). The EBSD map with a size of  $300 \times 865 \mu\text{m}$  and a resolution of  $0.4 \mu\text{m}$  contains some 1.6 million EBSD measurements. The inset in Figure 4.9 b shows the location of investigated subsets above the interface (relative to the base of the image) *a-j* and below the interface *-a* & *-b*. The location and shape of the subsets was chosen to be located parallel to the local topography of the interface to investigate possible effects of the distance to the interface on grain size, shape (SPO), lattice preferred orientations (LPO) and compression direction. Opposing arrows in Figure 4.9 b show the tectonic compression direction inferred from the stylolite teeth orientation, which is a reliable indicator of the compression direction (Koehn et al. 2007).

The grain size and shape analysis was again based on EBSD measurements as outlined in the previous chapter. Mean (arithmetic) grain area is  $2.9 \mu\text{m}^2$  (standard deviation of  $\pm 5.1 \mu\text{m}^2$ ) and a median of  $1.28 \mu\text{m}^2$  the geometric mean is  $1.2 \mu\text{m}^2$ . A clear SPO exist ( $\theta$ ) with a mean of  $76^\circ$  and a median value of  $70^\circ$  (for the complete dataset refer to Fig. 4.8 a). Analyzing the individual subsets and plotting the grain area (Fig. 4.9 c) and  $\theta$  (Fig. 4.9 d) as a function of the distance to the interface reveal considerable variations of these parameters.

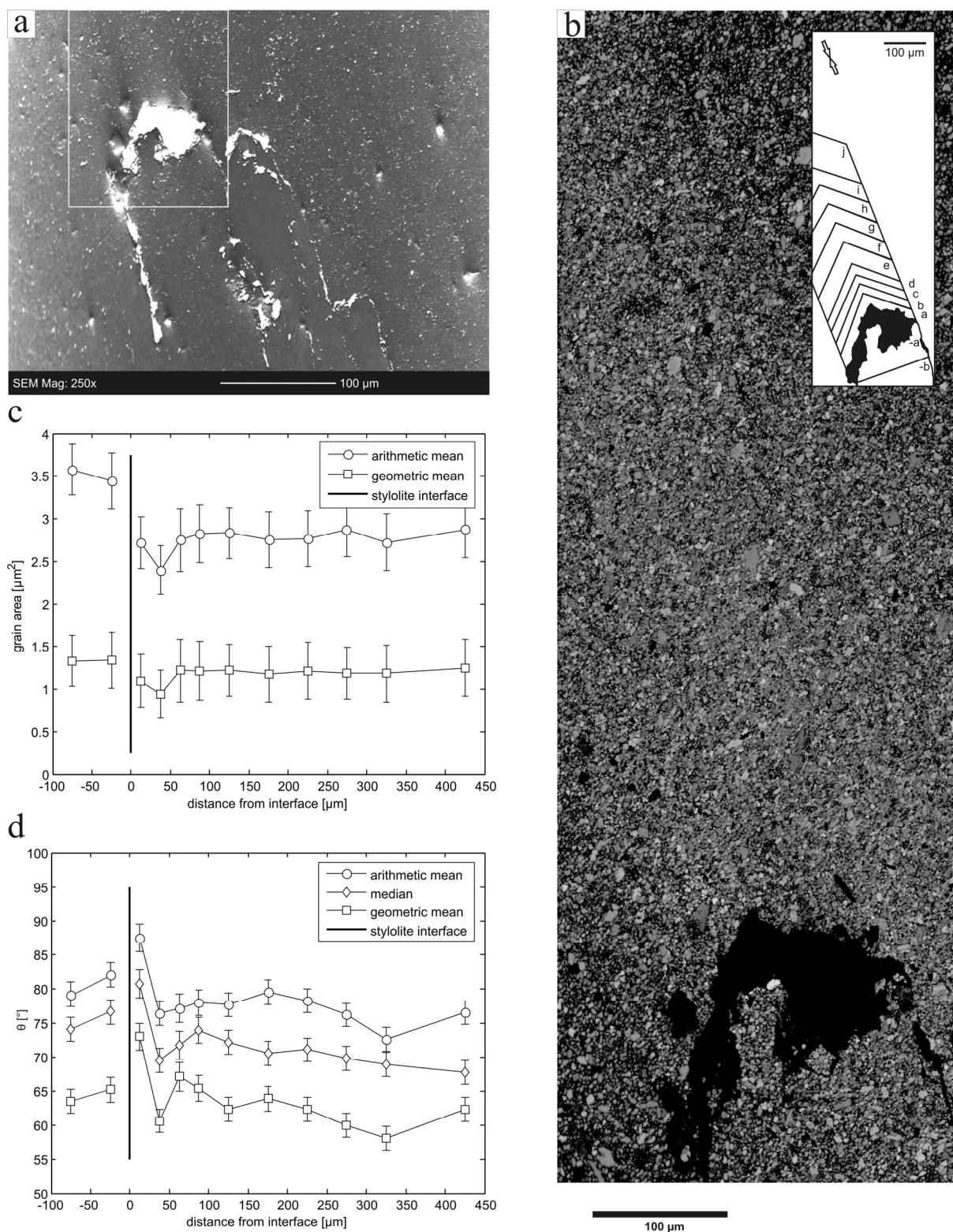


**Figure 4.9** Detailed investigation of the matrix as a function of the distance to the mature interface. **(a)** OC image of the large asperity investigated along the tectonic stylolite of sample Sa7b. **(b)** EBSD Band contrast of the entire map showing the outlines of individual grains and the stylolite peak in the lower part of the map. Inset shows the tectonic compaction direction (opposing arrows) and the position and outline of the investigated subsets labeled a-j (above the interface) and -a & -b (below the interface). **(c)** Graph of the (arithmetic and geometric) mean area (μm<sup>2</sup>) plotted as a function of the distance to the stylolite interface. **(d)** The SPO i.e.  $\theta$  plotted as a function of the distance to the interface. The coefficient of variance is indicated by the error bars shown in c and d.

Figure 4.9 c shows the arithmetic (circle) and geometric mean grain areas ( $\mu\text{m}^2$ ) of individual subsets the coefficient of variation is plotted as error-bars around the mean values. It is important to notice that the grain size remains constant in a range of 75-500  $\mu\text{m}$  above the stylolite interface. But the grain size drops from an average of 1.2 to 0.9  $\mu\text{m}^2$  (geometric mean) in a region 25-75  $\mu\text{m}$  and increases again to 1.2  $\mu\text{m}^2$  in a region  $<25$   $\mu\text{m}$  from the interface. Below the interface the grain area is significantly larger for both, arithmetic and geometric mean. The strong SPO (Fig. 4.9 d; compare Fig. 4.8 a for complete dataset) of the sample is also modified toward the interface. The mean (arithmetic and geometric) and median exhibit a slight counter clockwise rotation of the SPO ( $5\text{-}10^\circ$ ) over a distance range of 100-500, which is followed by a clockwise rotation of  $5^\circ$  in the next 75  $\mu\text{m}$ . In the region adjacent to the interface (distance  $<25$   $\mu\text{m}$ ) the SPO rotates  $10^\circ$  counterclockwise. Additionally the strength of the SPO, i.e. the kurtosis, generally decreases towards the interface.

The LPO of the sample (compare Fig. 4.9 & 4.10) is represented in equal area upper hemisphere pole figures of the  $c(0001)$ ,  $r(10\text{-}14)$ ,  $a(11\text{-}20)$  and  $f(01\text{-}12)$  poles. The complete dataset shows a weak LPO with the  $c$  poles being oriented in a great circle roughly normal and the  $a$ -poles exhibit small circles oriented parallel to the sedimentary compaction direction. In the subsets e-j (defined in Fig. 4.9 b) this orientation is more or less evident. In the vicinity of the stylolite interface (i.e. subsets a-d) the LPO changes. The  $c$ -poles show a localized single maximum parallel to the tectonic shortening/compression direction and the  $a$ -poles show very weakly defined small circles normal to this shortening direction. The orientation of the  $c$ - and  $a$ -poles is similar to reported uniaxial compression experiments (Wenk 1985, Wenk et al. 1987). Across the interface the LPO has a different orientation, with  $c$ -poles defining a great circle which is not aligned with neither the sedimentary compaction nor the tectonic compression direction. We do not observe an effect of twinning of calcite e.g.  $e$  or  $r$ -twins, in the sample which is supposed to be the dominant low grade deformation mechanism in calcite polycrystals (Passchier & Trouw 2005, Lacombe 2007).

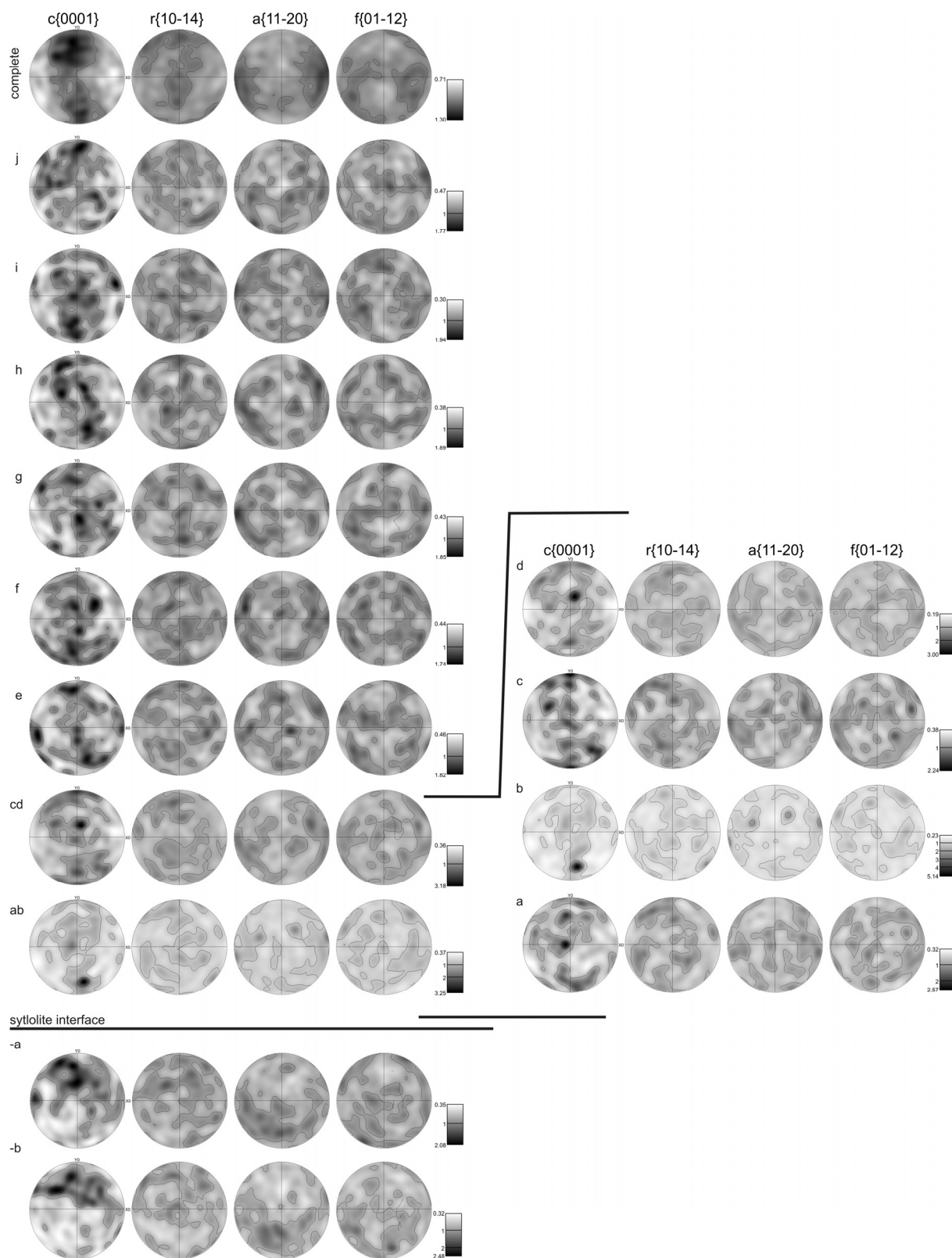


**Figure 4.10** Contoured pole figure plots of the LPO of calcite from the map in Figure 4.9 b (same representation as in Fig. 4.4). Topmost row shows the complete data set. The following rows represent the subset indicated in the inset of Figure 4.9 b (labeling refers to these subsets)

## 4.4. Discussion

In the previous chapter we presented direct observational evidence of the heterogeneities initially present in the matrix surrounding both initial and mature stylolites. In addition we illustrated the influence of mature stylolites on the adjacent matrix. Thus, we will first discuss the implication of heterogeneities and then focus on the matrix adjustments and its significance for stylolite development.

### 4.4.1. Quenched noise around stylolites

The work of Railsback (1993) and Andrews & Railsback (1997) demonstrated that a series of parameters of stylolite morphology can be related to the host rock lithology. They also argue that “lithologic heterogeneity” influences the morphology of stylolites e.g. more heterogeneous grainstones and packstones form more serrate morphologies than wackestones and mudstones. But they do not characterize heterogeneity nor do they investigate the heterogeneities which initiate the roughness of stylolites. Based on thorough statistical analysis Brouste et al. (2007) showed that stylolites interfaces can become non-stationary signals i.e. the scaling properties of stylolites change along the interface, which they argue is due to a variation of the quenched disorder in the material. In addition analytical (Renard et al. 2004, Schmittbuhl et al. 2004) and numerical (Koehn et al. 2007, Ebner et al. 2009b) approaches have successfully used heterogeneities as a cause for the roughness. The results of the works cited above all indicate that a quenched disorder plays an important role in the formation of stylolite roughness. Nevertheless none of the above studies directly proved the existence nor did they show the composition or distribution of these heterogeneities.

In the present work we analyzed bedding parallel and tectonic stylolites hosted in limestones of varying lithology and geological setting. We found strong evidence that heterogeneity e.g. clay particles, plays a crucial role in the formation of the distinctive roughness of stylolites. The fact that virtually all stylolite peaks contain a clay particle on their convex side implies that these heterogeneities form some kind of pinning particles which tend to inhibit dissolution on the respective side of the interface (Fig. 4.2). In general the clay particles are more than one order of magnitude smaller than the calcite grains. This clearly rules out that stylolite roughness is a function of the host rock grain size which underlines the results of Karcz & Scholz (2003). We also noticed that calcite-calcite contacts show irregular grain boundaries without any clay particles between them. This indicates that a different heterogeneity (e.g. chemical) possibly influences the roughening without the aid of clay particles. In addition we found detrital quartz grains along thickness variations in the residual clay layer of stylolite interfaces (Fig. 4.7). Since we could not attribute the thickness variation to a change in the distribution or abundance of the clay surrounding the interface we argue that these quartz grains form a different class of pinning particles, which are resistant to dissolution. Beyond that the quartz grains might indent into the residual clay layer as soon as they hit the pressure solution surface and thus cause this columnar morphology evident from Figure 4.7.

In our opinion it is these heterogeneities that we presented in this study (clay particles and quartz grains), which, due to a different resistance to dissolution, cause the roughening of stylolites. These heterogeneities may span several orders of magnitude in size and vary in abundance and composition to form a multi-scale, polymict quenched noise. Furthermore we do not argue that heterogeneities are limited to the range of scales we have investigated ( $\mu\text{m}$  to  $\text{dm}$ ) but are convinced that heterogeneities will be found on even smaller scales. The rough calcite-calcite contacts imply that there has to be a different (smaller) heterogeneity which might be a chemical variation i.e. integration of Mg instead of Ca in the atomic lattice or a change in the elastic properties due to lattice defects. To resolve this issue submicron scale chemical mapping and/or TEM analysis would be necessary. The pinning particles identified in this study might only be a small portion of the variety of heterogeneity that induces stylolite roughness. For example in stylolites in other lithologies, e.g. quartzite, other heterogeneities (such as small micas or oxides) might form the dominant disorder. The identification and quantification of this quenched disorder in rocks hosting stylolites can be achieved with an approach presented in this study. The results presented here could potentially provide a quantitative basis and prerequisite for more sophisticated numerical models of pressure solution (Koehn et al. 2007, Ebner et al. 2009b). We thus argue that the general idea of a vague ‘lithologic heterogeneity’, which influences the stylolite morphology put forward by Railsback (1993), is in its respect correct but go further by demonstrating that the heterogeneities presented cause the characteristic roughness to develop and thus generate the stylolite. Consequently the current work offers strong arguments that supports a *heterogeneity concept* for the initiation of the stylolite roughness.

#### 4.4.2. Matrix modifications around stylolite interfaces

The matrix around stylolites was mainly investigated in terms of porosity reduction and its influences on fluid flow in sandstones (Harris 2006, Baron & Parnell 2007, Mørk & Moen 2007) and limestones (Carrio-Schaffhauser et al. 1990, Raynaud & Carrio-Schaffhauser 1992), which form a reservoir for hydrocarbon. There is a general agreement among previous workers that pressures solution along stylolites provides a local source for cement around them. Low porosity haloes of up to several cm in width are reported (Harris 2006, Baron & Parnell 2007), but close examination under the SEM demonstrated that the porosity in the vicinity of the stylolite increases (within a few microns) which is termed the ‘process zone’ by Carrio-Schaffhauser et al. (1990), which transforms into a low porosity zone around this ‘process zone’. Microstructural investigations of experimentally compacted sandstones (van Noort et al. 2008) and drilled sandstone samples from North Sea (Mørk & Moen 2007), demonstrated that plastic deformation occurs around intergranular and localized pressure solution features. These authors report the occurrence of micro-cracks and dauphiné twins from grain-grain contacts and dauphine twins localized around stylolites. This demonstrates that localized pressure solution features have a large impact on the surrounding matrix and thus have to be carefully investigated to understand the dynamic evolution of stylolite formation from an initial interface with undisturbed matrix to a mature interface with a modified

host rock matrix, which will in turn modify the pressure solution process. We have not investigated the porosity around stylolites but our results on the matrix adjustments will complement the published data.

To distinguish between the effect of soft sediment compaction structures and pressure solution imposed features we investigated a tectonic stylolite which trends normal to the sedimentary compaction direction. This high angle difference in the sedimentary and tectonic compaction direction allows us to discern the effects of both events. Sedimentary compaction caused a strong SPO (Fig. 4.8 a) and a weak LOP (Fig. 4.9) of the fine-grained calcite matrix surrounding the tectonic stylolite. Both SPO and LOP indicate a sedimentary compaction direction which is roughly horizontal in Figure 4.9 b. Approaching the stylolite interface we found that in the matrix the (i) grain size (ii) SPO and (iii) LPO are modified.

The average grain size i.e. grain area of  $\sim 3.0 \mu\text{m}^2$  decreases some 15% ( $2.5 \mu\text{m}^2$ ) in a region 25-75  $\mu\text{m}$  away from the stylolite and finally increases to  $\sim 3.0 \mu\text{m}^2$  in the direct vicinity of the stylolite. Comparison to other common measures of the grain size (Humphreys 2001) like linear intercept method or circle equivalent diameter reveal the same results. Our results are quite similar to the data reported by Raynaud & Carrio-Schaffhauser (1992). But compared to a region of 1-2  $\mu\text{m}$  around the stylolite of reduced grain size and increased porosity which they termed 'process zone', the region of reduced grain size we have identified is 1-2 orders of magnitude larger.

The sedimentary SPO (Fig. 4.7 a), i.e. the average orientation of the long axis of calcite grains ( $\theta$ ), trending roughly N-S (due to E-W sedimentary compaction) is very well defined. Evidence for N-S directed tectonic compaction that influences a broader zone around the stylolite would be indicated by a gradual decrease from high  $\theta$  to low  $\theta$  values. In fact we observed the opposite, the  $\theta$  values slightly increase toward the interface. Only in the region of reduced grain size 25-75  $\mu\text{m}$  away from the interface  $\theta$  decreases some 5-10°. It is interesting to notice that the kurtosis, a measure for the strength or 'peakedness' of a probability distribution, decreases towards the interface. This is an indication that the SPO gets obliterated toward the interface.

The weak sedimentary LPO is defined by c-axis being oriented in a great circle normal to the compaction direction (Fig. 4.10). In the vicinity of the stylolite (25-75  $\mu\text{m}$  away) this sedimentary LPO is overprinted by a relatively well defined single maximum of c-axis parallel to the tectonic compaction direction. Numerical simulations (Bons & den Brok 2000) showed that solution-precipitation creep can indeed play a role in the formation of an LPO. The model of Bons & den Brok (2000) is based on the observation that Quartz has a directional anisotropy in the dissolution rate i.e. c-axis exhibit the smallest amount of dissolution and grains which have an orientation of 50° between the c-axis and the shortening direction the highest amounts of dissolution (Becker 1995, den Brok 1996). This suggests a preferential dissolution of grains with the c-axis inclined 50° away from the compaction direction and in turn favors the development of a LPO. LPO measurements of uniaxial compaction experiments and theoretical considerations show c-axis maxima parallel to the compaction direction (Wenk 1985, Wenk et al. 1987), which is in line with our findings. We are thus convinced that the LPO in the vicinity of the stylolite can be addressed to the tectonic compaction.



As a last point we have to discuss the features in the matrix adjacent to the stylolite (<25  $\mu\text{m}$  away from the interface). We observe that in this region the grain size increases 15 % and the SPO changes 15-20° and the LPO shows a quasi random pattern. To explain these characteristics of the matrix two scenarios seem possible. First a late stage fluid flow that post dates pressure solution along the interface could have deposited calcite cement in the intergranular pore space. This could account for the grain size increase and the change in the SPO since more isometric grains would have a SPO which will resemble a Gaussian distribution with a high variance and thus show a mean around 90°. The obliteration of the LPO is harder to explain with this hypothesis since cements often show overgrowth which has a similar crystallographic orientation as the host grain (Mørk & Moen 2007). A second possibility could be a process similar to Ostwald ripening (Morse & Casey 1988) in the fluid filled vicinity of the stylolite interface. Ostwald ripening is a process which leads to preferential grain growth (i.e. large grains grow on the expense of small grains) to minimize the surface to volume ration and thus the surface free energy. Such a surface minimization process could account for the grain size increase and, due to the preferential dissolution of the small grains, to a destruction of the SPO and LPO.

We hypothesize that that mature interfaces form a ‘mechanical layer’ which is able to transmit stresses which in turn induces intergranular pressure solution in a region around the stylolite, either due to an undercutting mechanism (Lehner 1995), free face dissolution (Tada et al. 1987, Tada & Siever 1989) or a combination of both. Such a conceptual model would self induce localized pressure solution and would be able to explain the grain size reduction and a perturbation of the preexisting sedimentary SPO and LPO, which we have observed.

## 4.5. Conclusion

In the present work we report a detailed qualitative and quantitative microstructural analysis based on EBSD/SEM and OC image analysis of stylolites in limestones. Our study sheds new light on the role of heterogeneities (in our case clay particles and detrital quartz grains) and matrix adjustments around mature stylolite interfaces. The importance of heterogeneities for the morphological development was stressed in previous work (Railsback 1993, Andrews & Railsback 1997) and successfully applied in analytical (Renard et al. 2004, Schmittbuhl et al. 2004) and numerical models (Koehn et al. 2007, Ebner et al. 2009b). But the data presented here provide direct observational evidence for a roughening of stylolites induced by heterogeneities on various scales. We conclude that this multi-scale quenched noise is responsible for the initiation of roughness along stylolites. In addition we demonstrate that around mature stylolite interfaces significant matrix modifications occur. By the investigation of tectonic stylolites with a bedding normal orientation we were able to discern the effects of sedimentary and tectonic compaction. This implies that localized pressure solution around stylolites imposes a halo with reduced grain size, and a perturbed SPO and LPO.

Both findings are important to future research on pressure solution surfaces. First, it provides a quantitative basis for the development of more sophisticated numerical models and secondly it implies that localized pressure solution is not necessarily restricted to the actual interface.

## 4.6. References

- Alvarez, W., Engelder, T. & Geiser, P. A. 1978. Classification of solution cleavage in pelagic limestones. *Geology* 6(5), 263-266.
- Andrews, L. M. & Railsback, L. B. 1997. Controls on stylolite development: Morphologic, lithologic, and temporal evidence from bedding-parallel and transverse stylolites from the US Appalachians. *Journal of Geology* 105(1), 59-73.
- Angheluta, L., Jettestuen, E., Mathiesen, J., Renard, F. & Jamtveit, B. 2008. Stress-Driven Phase Transformation and the Roughening of Solid-Solid Interfaces. *Physical Review Letters* 100(9), 096105.
- Arnaud-Vanneau, A. & Arnaud, H. 1990. Hauterivian to Lower Aptian carbonate shelf sedimentation and sequence stratigraphy in the Jura and northern Subalpine Chains (southeastern France and Swiss Jura). In: *Carbonate Platforms* (edited by Tucker, M. E., Wilson, J. L., Crevello, P. D., Sarg, J. F. & Read, J. F.) 9. Spec. Publ. Int. Ass. Sediment. , 203-233.
- Baron, M. & Parnell, J. 2007. Relationships between stylolites and cementation in sandstone reservoirs: Examples from the North Sea, U.K. and East Greenland. *Sedimentary Geology* 194(1-2), 17-35.
- Bathurst, R. G. C. 1987. Diagenetically Enhanced Bedding in Argillaceous Platform Limestones - Stratified Cementation and Selective Compaction. *Sedimentology* 34(5), 749-778.
- Bayly, B. 1986. A Mechanism for Development of Stylolites. *Journal of Geology* 94(3), 431-435.
- Becker, A. 1995. Quartz pressure solution: influence of crystallographic orientation. *Journal of Structural Geology* 17(10), 1395-1397.
- Bodou, P. 1976. Importance of the stylolitic joints in the compaction of limestones. *Bull. Centre Rech. Pau - SNPA* 10(2), 627-644.
- Bonnetier, E., Misbah, C., Renard, F., Toussaint, R. & Gratier, J. P. 2009. Does roughening of rock-fluid-rock interfaces emerge from a stress-induced instability? *The European Physical Journal B - Condensed Matter and Complex Systems* 67(1), 121-131.
- Bons, P. D. & den Brok, B. 2000. Crystallographic preferred orientation development by dissolution-precipitation creep. *Journal of Structural Geology* 22(11-12), 1713-1722.
- Brouste, A., Renard, F., Gratier, J. P. & Schmittbuhl, J. 2007. Variety of stylolites' morphologies and statistical characterization of the amount of heterogeneities in the rock. *Journal of Structural Geology* 29(3), 422-434.

- Buxton, T. M. & Sibley, D. F. 1981. Pressure Solution Features in a Shallow Buried Limestone. *Journal of Sedimentary Petrology* 51(1), 19-26.
- Carrio-Schaffhauser, E., Raynaud, S., Latiere, H. J. & Mazerolle, F. 1990. Propagation and localization of stylolites in limestones. In: *Deformation Mechanics, Rheology and Tectonics* (edited by Knipe, R. J. & Rutter, E. H.) 54. Geological Society Special Publications, 193-199.
- den Brok, B. 1996. The effect of crystallographic orientation on pressure solution in quartzite. *Journal of Structural Geology* 18(6), 859-860.
- Drummond, C. N. & Sexton, D. N. 1998. Fractal structure of stylolites. *Journal of Sedimentary Research* 68(1), 8-10.
- Dunnington, H. V. 1954. Stylolite development post-dates rock induration. *Journal of Sedimentary Petrology* 24(1), 27-49.
- Ebner, M., Koehn, D., Toussaint, R., Renard, F. & Schmittbuhl, J. 2009a. Stress sensitivity of stylolite morphology. *Earth and Planetary Science Letters* 277(3-4), 394-398.
- Ebner, M., Koehn, D., Toussaint, R. & Renard, F. 2009b. The influence of rock heterogeneity on the scaling properties of simulated and natural stylolites. *Journal of Structural Geology* 31(1), 72-82.
- Etzold, A., Franz, M. & Villinger, E. 1996. Schwäbische Alb - Stratigraphie, Tektonik, Vulkanismus, Karsthydrogeologie. *Z. geol. Wiss.* 24(1/2), 175-215.
- Geyer, O. F. & Gwinner, M. P. 1991. *Geologie von Baden-Württemberg*. Schweizerbart'sche Verlagsbuchhandlung, Stuttgart.
- Gratier, J. P., Muquet, L., Hassani, R. & Renard, F. 2005. Experimental microstylolites in quartz and modeled application to natural stylolitic structures. *Journal of Structural Geology* 27(1), 89-100.
- Guzzetta, G. 1984. Kinematics of Stylolite Formation and Physics of the Pressure-Solution Process. *Tectonophysics* 101(3-4), 383-394.
- Harris, N. B. 2006. Low-Porosity Haloes at Stylolites in the Feldspathic Upper Jurassic Ula Sandstone, Norwegian North Sea: An Integrated Petrographic and Chemical Mass-Balance Approach. *Journal of Sedimentary Research* 76(3), 444-459.
- Heald, M. T. 1955. Stylolites in Sandstones. *Journal of Geology* 63(2), 101-114.
- Heilbronner, R. & Keulen, N. 2006. Grain size and grain shape analysis of fault rocks. *Tectonophysics* 427(1-4), 199-216.
- Heilbronner, R. P. 1992. The autocorrelation function: an image processing tool for fabric analysis. *Tectonophysics* 212(3-4), 351-370.
- Humphreys, F. J. 2001. Review - Grain and subgrain characterisation by electron backscatter diffraction. *Journal of Materials Science* 36(16), 3833-3854.
- Karcz, Z. & Scholz, C. H. 2003. The fractal geometry of some stylolites from the Calcare Massiccio Formation, Italy. *Journal of Structural Geology* 25(8), 1301-1316.
- Kley, J. & Voigt, T. 2008. Late Cretaceous intraplate thrusting in central Europe: Effect of Africa-Iberia-Europe convergence, not Alpine collision. *Geology* 36(11), 839-842.

- Koehn, D., Renard, F., Toussaint, R. & Passchier, C. W. 2007. Growth of stylolite teeth patterns depending on normal stress and finite compaction. *Earth and Planetary Science Letters* 257(3-4), 582-595.
- Lacombe, O. 2007. Comparison of paleostress magnitudes from calcite twins with contemporary stress magnitudes and frictional sliding criteria in the continental crust: Mechanical implications. *Journal of Structural Geology* 29(1), 86-99.
- Lehner, F. K. 1995. A model for intergranular pressure solution in open systems. *Tectonophysics* 245(3-4), 153-170.
- Marshak, S. & Engelder, T. 1985. Development of Cleavage in Limestones of a Fold-Thrust Belt in Eastern New-York. *Journal of Structural Geology* 7(3-4), 345-359.
- Mingard, K. P., Roebuck, B., Bennett, E. G., Thomas, M., Wynne, B. P. & Palmiere, E. J. 2007. Grain size measurement by EBSD in complex hot deformed metal alloy microstructures. *Journal of Microscopy-Oxford* 227(3), 298-308.
- Mørk, M. B. E. & Moen, K. 2007. Compaction microstructures in quartz grains and quartz cement in deeply buried reservoir sandstones using combined petrography and EBSD analysis. *Journal of Structural Geology* 29(11), 1843-1854.
- Morse, J. W. & Casey, W. H. 1988. Ostwald Processes and Mineral Paragenesis in Sediments. *American Journal of Science* 288(6), 537-560.
- Moss, S. & Tucker, M. E. 1995. Diagenesis of Barremian-Aptian platform carbonates (the Urgonian Limestone Formation of SE France): near-surface and shallow-burial diagenesis. *Sedimentology* 42(6), 853-874.
- Panozzo, R. H. 1983. Two-dimensional analysis of shape-fabric using projections of digitized lines in a plane. *Tectonophysics* 95(3-4), 279-294.
- Park, W. C. & Schot, E. H. 1968. Stylolites: their nature and origin. *Journal of sedimentary Petrology* 38(1), 175-191.
- Passchier, C. W. & Trouw, R. A. J. 2005. *Microtectonics*. Springer, Berlin.
- Petit, J. P. & Mattauer, M. 1995. Palaeostress superimposition deduced from mesoscale structures in limestone: the Matelles exposure, Languedoc, France. *Journal of Structural Geology* 17(2), 245-256.
- Prior, D. J., Trimby, P. W., Weber, U. D. & Dingley, D. J. 1996. Orientation contrast imaging of microstructures in rocks using foreshatter detectors in the scanning electron microscope. *Mineralogical Magazine* 60(6), 859-869.
- Prior, D. J., Boyle, A. P., Brenker, F., Cheadle, M. C., Day, A., Lopez, G., Peruzzi, L., Potts, G., Reddy, S., Spiess, R., Timms, N. E., Trimby, P., Wheeler, J. & Zetterstrom, L. 1999. The application of electron backscatter diffraction and orientation contrast imaging in the SEM to textural problems in rocks. *American Mineralogist* 84(6), 1741-1759.
- Railsback, L. B. 1993. Lithologic Controls on Morphology of Pressure-Dissolution Surfaces (Stylolites and Dissolution Seams) in Paleozoic Carbonate Rocks from the Mideastern United-States. *Journal of Sedimentary Research* 63(3), 513-522.

- 
- Raynaud, S. & Carrio-Schaffhauser, E. 1992. Rock Matrix Structures in a Zone Influenced by a Stylolite. *Journal of Structural Geology* 14(8-9), 973-980.
- Renard, F., Schmittbuhl, J., Gratier, J. P., Meakin, P. & Merino, E. 2004. Three-dimensional roughness of stylolites in limestones. *Journal of Geophysical Research-Solid Earth* 109(B3), -.
- Rispoli, R. 1981. Stress-Fields About Strike-Slip Faults Inferred from Stylolites and Tension Gashes. *Tectonophysics* 75(3-4), T29-T36.
- Schmittbuhl, J., Renard, F., Gratier, J. P. & Toussaint, R. 2004. Roughness of stylolites: Implications of 3D high resolution topography measurements. *Physical Review Letters* 93(23), -.
- Stockdale, P. B. 1922. Stylolites: their nature and origin. *Indiana University Studies* 9, 1-97.
- Tada, R., Maliva, R. & Siever, R. 1987. A new mechanism for pressure solution in porous quartzose sandstone. *Geochimica et Cosmochimica Acta* 51(9), 2295-2301.
- Tada, R. & Siever, R. 1989. Pressure Solution during Diagenesis. *Annual Review of Earth and Planetary Sciences* 17, 89-118.
- van Noort, R., Spiers, C. J. & Pennock, G. M. 2008. Compaction of granular quartz under hydrothermal conditions: Controlling mechanisms and grain boundary processes. *J. Geophys. Res.* 113.
- Wenk, H. R. 1985. Preferred orientation in deformed metals and rocks: An introduction to modern texture analysis. Academic Press, Orlando (FL).
- Wenk, H. R., Takeshita, T., Bechler, E., Erskine, B. G. & Matthies, S. 1987. Pure shear and simple shear calcite textures. Comparison of experimental, theoretical and natural data. *Journal of Structural Geology* 9(5-6), 731-745.



## 5. The influence of rock heterogeneity on the scaling properties of simulated and natural stylolites

### Abstract

Stylolites are among the most prominent deformation patterns in sedimentary rocks that document localized pressure solution. Recent studies revealed that stylolite roughness is characterized by two distinct scaling regimes. The main goal of the present study is to decipher whether this complex scaling behavior of stylolites is caused by the composition of the host rock, *i.e.* heterogeneities in the material, or is governed by inherent processes on respective scales, namely the transition from a surface energy to an elastic energy dominated regime, as theoretically predicted. For this purpose we have developed a discrete numerical technique, based on a lattice spring model, to simulate the competition between stress, strain, and dissolution during stylolite roughening. We varied systematically the quenched noise, initially present in the material, which controls the roughening. We also changed the size, amount, and dissolution rate of the heterogeneities introduced in our model and evaluated the influence on the scaling exponents. Our findings demonstrate that the roughness and growth exponents are independent of the exact nature of the heterogeneities. We discovered two coinciding crossover phenomena in space and time that separate length and timescales for which the roughening process is either balanced by surface or elastic energies. Our observations are consistent with analytical predictions and with investigations quantifying the scaling laws in the morphology of natural stylolites. The findings presented here can further be used to refine volume loss (compaction) estimates from the finite strain pattern of stylolites.

*(\*) This chapter was published as:*

*Ebner, M., Koehn, D., Toussaint, R. & Renard, F. 2009. The influence of rock heterogeneity on the scaling properties of simulated and natural stylolites. Journal of Structural Geology 31(1), 72-82.*

### 5.1. Introduction

Pressure solution in sedimentary rocks results in either intergranular or localized dissolution of material (e.g. Tada and Siever, 1989). The latter is responsible for the formation of stylolites, a frequent deformation pattern in sedimentary rocks (e. g. Stockdale, 1922; Dunnington, 1954; Heald, 1955; Park & Schot, 1968; Buxton & Sibley 1981; Rutter, 1983; Railsback, 1993). Stylolites are rough interfaces that contain insoluble material (Fig. 5.1), which is considered to be the residuum of the dissolved rock

(Railsback, 1993; and references cited therein). Stylolite initiation is still highly debated (e.g. Tada and Siever, 1989) but several mechanisms have been proposed that are in agreement with field observations: Formation (I) along preexisting anisotropies (Bathurst, 1987) (II) as anticracks (Fletcher and Pollard, 1981) that propagate due to stress concentrations at anticrack tips (even though this idea was challenged recently by Katsman et al., 2006) and (III) by stress induced self-organization (Merino, 1992, Railsback, 1998; Merino et al., 2006).

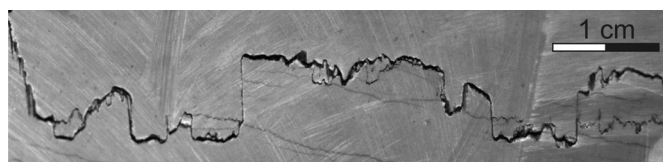


**Figure 5.1** Plane section of a bedding parallel stylolite in a Jurassic limestone from Cirque de Navacelles (southern France). The rough interface is accentuated by a thin clay layer that is considered to be the residuum of the dissolved rock mass.

In the present study we quantify the roughness of simulated stylolites and study their dynamic development independent of the process leading to the localization of dissolution along a plane. Based on recent quantitative methods of stylolite roughness characterization (Renard et al., 2004; Schmittbuhl et al., 2004; Koehn et al., 2007; Ebner et al., 2009) we use statistical tools to compare simulated and natural stylolites. In particular we study the influence of initial heterogeneity concentration in the host-rock on a) stylolite roughness, b) dynamic roughness growth and c) the correlation of crossover phenomena in space and time. To integrate the results of our study in the context of quantitative characterization we will first review the basic principles of our approach.

The exact classification of stylolites in the field is a difficult task because there is a wide range of geometries (e.g. Park and Schott, 1968) that are often transitional even within a single outcrop. Many previous studies (Park and Schot, 1968; Buxton and Sibley, 1981; Guzzetta, 1984; Tada and Siever, 1989; Railsback, 1993) used classification schemes that were based on visual descriptions of macroscopic features of stylolites. These classification schemes are not quantitative and they are hard to compare since these studies focused on a variety of different aspects of stylolite formation. Recent studies, however (Drummond and Sexton, 1998; Karcz and Scholz, 2003) took a more quantitative approach using fractal concepts to describe the stylolite roughness in a statistical sense. They could describe stylolite roughness with a fractal scaling over several orders of magnitude, which means that their roughness is not dominated by a certain wavelength.

Renard et al. (2004) and Schmittbuhl et al. (2004) demonstrated that bedding parallel stylolite surfaces show a self-affine scaling invariance with characteristic Hurst exponents (also called roughness exponents). A self-affine rough surface is characterized statistically by the fact that points along the surface separated by a distance  $\Delta x$  from each other are typically distant in the direction transverse to the surface by  $\Delta h = \Delta x^\alpha$ , where  $\alpha$  is the roughness exponent. It was further noticed that two distinct scaling regimes exist that were characterized by two different Hurst or roughness exponents separated by a crossover-length ( $L$ ), around the millimeter scale for the analyzed natural stylolites. Above this crossover,



all investigated stylolites exhibit a Hurst exponent of about 0.5 meaning that they change relatively fast from being flat features on larger scale to being rough features on the smaller scale. Below the crossover-length the Hurst exponent is about 1.0, which means that the slope, or aspect ratio  $\Delta z/\Delta x$ , stays more or less constant. Schmittbuhl et al. (2004) and Renard et al. (2004) established from first principles of mechanics and chemistry a model for stylolite growth under the form of a stochastic partial differential equation (called in this case a generalized Langevin equation). This equation simulates the roughening of a stylolite surface as a competition between stabilizing forces (that keep the surface flat), which are controlled by long range elastic and local surface tension effects, and destabilizing forces (that roughen the interface) that are induced by pinning effects of material heterogeneities. The analytical solution of Schmittbuhl et al. (2004) reproduced the observed scaling behavior of natural stylolites and demonstrated that the two scaling regimes (characterized by the two different Hurst exponents) correspond to two thermodynamic regimes that are dominated by either surface or elastic energies on small and large scales, respectively (Renard et al., 2004; Schmittbuhl et al., 2004; Gratier et al., 2005). Based on the work of Schmittbuhl et al. (2004) it was demonstrated for the first time by Ebner et al. (2009) that the crossover-length of natural stylolites, which should be a function of the stress during stylolite growth, can be used to determine stress magnitudes and burial depth in sedimentary basins. The discrete numerical simulation technique of Koehn et al. (2007) enabled to study the dynamics of the roughening process through time revealing that the stylolite interface width  $w$  (defined in detail below) grows as a power law with time ( $w \sim t^\beta$ ) with a growth exponent  $\beta$  of 0.5 in the surface energy dominated regime and a growth exponent of 0.8 in the elastic energy dominated regime. In addition the roughness growth may saturate so that the stylolites lose their memory for compaction or finite strain. It is important to notice that the roughness of simulated stylolites in this contribution is produced by heterogeneities in the material that pin the stylolitic interface due to slower dissolution rate constants, which are in competition with the surface and elastic energies which tend to flatten the surface (Koehn et al., 2007). Therefore the obvious question to ask is whether a variation of the quenched noise changes the scaling properties of the stylolitic interface?

Thus, in the present contribution we investigate the influence of different heterogeneities (namely the percentage of pinning particles, their pinning factor (defined below), and their size) on the scaling behavior, dynamic growth, and determined crossover length of simulated stylolites.

## 5.2. Numerical model setup

The numerical technique that we use to simulate stylolite roughening is based on a lattice-spring model coupled with a dissolution routine (Koehn et al., 2004, 2006, 2007). The model itself is embedded as a module in the “*Elle*” modeling-platform (Bons et al., 2008).

For computational reasons, to access large systems and analyze scaling laws over a large system size - resolution ratio, we will consider situations spatially invariant along one of the directions tangential to the stylolite – and effectively treat systems with two spatial dimensions. For the same reasons, we assume that the heterogeneity in the rock as well as the statistical properties of the stylolite surface can be represented

in a 2D model, as shown in Figure 5.2 a, which contains a predefined flat interface filled with a confined fluid. Two blocks of particles are separated by a fluid pocket. Such a configuration is expected for example, in the case of a fluid pocket embedded between two low permeability sedimentary layers. This model system represents two solids or rocks that are pressed together by inward moving top and bottom boundaries, whereas the side boundaries remain fixed (uniaxial strain). A quenched noise (denoted by darker particles in Fig. 5.2 a & b) is introduced by assigning a lower dissolution rate constant to a certain fraction of the particles (= pinning particles) and represents material heterogeneities initially present in the host rock of natural stylolites.

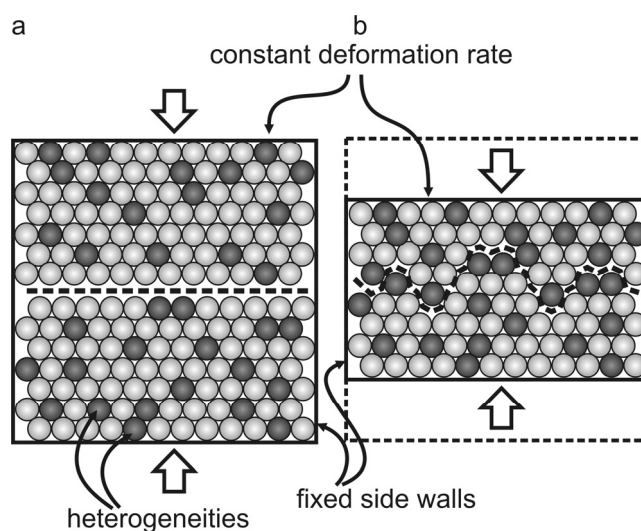


**Figure 5.2** Simplified sketch of the setup of the numerical model (modified after Koehn et al., 2007). The top and bottom walls of the box are moved inwards simultaneously to stress the system and initiate dissolution along the interface. **(a)** Initial configuration of the setup showing a flat interface (dashed line). **(b)** Configuration after a certain amount of compaction. The interface (dashed line) has developed a distinct roughness, note that the heterogeneities (darker spheres) accumulate along the interface.

### 5.2.1. Theory

This section provides only a cursory review on the governing equations of the dissolution process used in the model. For a detailed description and implementation the reader is referred to Koehn et al. (2007) and Bons et al. (2008).

The pressure solution process is discretized in steps of dissolution of entire particles, following a linear rate law (Koehn et al., 2007 and references cited therein) according to

$$D = kV \left[ 1 - \exp \left( - \frac{\{\Delta\psi + \Delta\sigma_n\}V}{RT} \right) \right], \quad (5.1)$$

where  $D$  is the dissolution velocity of the interface ( $\text{m s}^{-1}$ ),  $k$  a dissolution kinetics rate constant ( $\text{mol m}^{-2} \text{s}^{-1}$ ),  $V$  the molecular volume of the solid ( $\text{m}^3 \text{mol}^{-1}$ ),  $R$  the universal gas constant ( $8.314 \text{ J mol}^{-1} \text{ }^\circ\text{K}^{-1}$ ),  $T$  the temperature ( $^\circ\text{K}$ ),  $\Delta\psi$  (Pa) the changes in Helmholtz free energy density (i.e. the sum of the elastic and

surface energy of particles in the discrete network.), which accounts for the variations in elastic and surface energies of the solid during dissolution of a solid element, and  $\Delta\sigma_n$  (Pa) the differences between the average normal stress along the interface and the local normal stress at a specific location which is due to the repulsion of the solids (Koehn et al., 2007). We assume that the dissolution process is reaction controlled and that the dissolved matter is transported out of the system. This implies that the diffusion may control the absolute time scale of the stylolite growth, but has no local influence on the reaction process and the roughening, which are a function of the amount of compaction and the number of dissolved particles (Koehn et al., 2007). We are not interested in absolute time scales in this contribution.

Surface energies ( $E^s$ ) of particles are calculated from the local curvature of the interface around each particle, which can be expressed as

$$E^s = \frac{\gamma}{\rho}, \quad (5.2)$$

where  $\gamma$  is the surface free energy and  $\rho$  is the local radius of curvature of the interface. We consider a plane strain situation, i.e. an invariance along the third spatial dimension, so one radius along the 2D plane investigated entirely characterizes the curvature of the interface – the radius of curvature along the direction of invariance is infinite, and no surface energy is associated to this direction. The surface energies of individual particles are averaged over their neighbors to avoid artifacts from the discreteness of the model (for details see Koehn et al., 2007).

In the lattice spring model every particle ( $i$ ) is connected to its neighbors ( $j$ ) via a triangular linear elastic spring network. The elastic energy ( $E^{el}$ ) of a single element is given by

$$E^{el} = \frac{1}{4} \sum_{(j)} \kappa (|x_i - x_j| - l)^2, \quad (5.3)$$

where the sum is over all neighbors ( $j$ ),  $\kappa$  is a spring constant and  $l$  is the equilibrium distance between elements  $i$  and  $j$ .

### 5.2.2. Basic numerical step

The constitutive equations stated above are implemented as follows:

1. Top and bottom walls are moved inwards simultaneously at a given time/deformation step.
2. For every deformation step the rate law (Eq. 5.1) is used to calculate if individual particles at the interface can dissolve in the given time as soon as the two solids meet.
3. When elements dissolve they are removed completely and the system can relax. Relaxation is accomplished by an over-relaxation algorithm that finds the new equilibrium configuration

for the lattice. Dissolution of particles can take place as long as the given time for the individual deformation step is not consumed.

4. If the deformation time is used up or no particles can dissolve within the given time the system is stressed again by a deformation step.

### 5.2.3. Parameters, boundary conditions, limitations

The material parameters we use resemble those of a limestone (e.g. Clark, 1966) and are in line with values used in Renard et al. (2004) and Schmittbuhl et al. (2004): a molar volume of  $0.00004 \text{ m}^3/\text{mol}$ , a Young's Modulus of 80 GPa, a Poisson's ratio of 0.33 (this number is given by the triangular lattice configuration), a surface free energy of  $0.27 \text{ J/m}^2$ , a temperature of 300 K and a dissolution rate constant of  $0.0001 \text{ mol}/(\text{m}^2\text{-s})$ . In addition, the displacement rate of the upper and lower boundaries are fixed at a constant value corresponding to a velocity of  $10^{-10} \text{ m s}^{-1}$ .

The boundary condition can be seen as equivalent to a constant load boundary condition since the dissolution process is fast enough to relax the stresses that build up during a single deformation step. The sidewalls remain fixed during the model runs and there is no wrapping of particles in the x-direction of the model.

We use three basic model setups for which we systematically vary the heterogeneities in the structure. All boxes used have the same number of particles (400 particles) in the x-direction but three different particles-sizes were used 0.01 mm, 0.1 mm and 1mm, which corresponds to absolute box-sizes of 4, 40 and 400 mm.

To introduce the quenched noise in the simulations a pseudorandom algorithm is used to create a spatial Gaussian distribution of particles that dissolve slower (pinning particles). We varied three parameters of the quenched noise in this study: (i) number of pinning particles in a range from 1-20%, (ii) dissolution rate constant of pinning particles (from 0.1-0.99 normalized to the dissolution rate constant of the matrix, which is 1), which determines the pinning factor and (iii) the absolute size of the heterogeneities which varies with the particle size in the range of 0.01-1 mm.

## 5.3. Data analysis & results

The individual model runs are grouped with respect to the particle-size of the model and are termed *surface*, *intermediate* and *elastic class* according to the dominance of the energy regime during the roughening process (Koehn et al., 2007). The *surface class* has a particle size of 0.01 mm (box size of 4 mm), the *intermediate class* a particle size of 0.1 mm (box size of 4 cm) and the *elastic class* a particle size of 1mm (box size of 40 cm). These three classes allow the investigation of a broad range of scales in a sufficient resolution. In nature the particles may resemble actual grains so that the grain size of the rock varies between the different classes. A single simulation with 400 particles in the x-direction may run from 10 to 15 days on 4 cores of a recent workstation, thus limiting the extent of our runs. Figure 5.3 shows the

roughening of stylolites of these three classes, each with identical quenched noise (5 % pinning particles with half the dissolution rate of the matrix) to demonstrate the influence of the absolute box/particle size. The differences in the roughness and the roughness growth can easily be seen when individual steps of different classes are compared and also by following the growth of individual stylolite peaks with time.

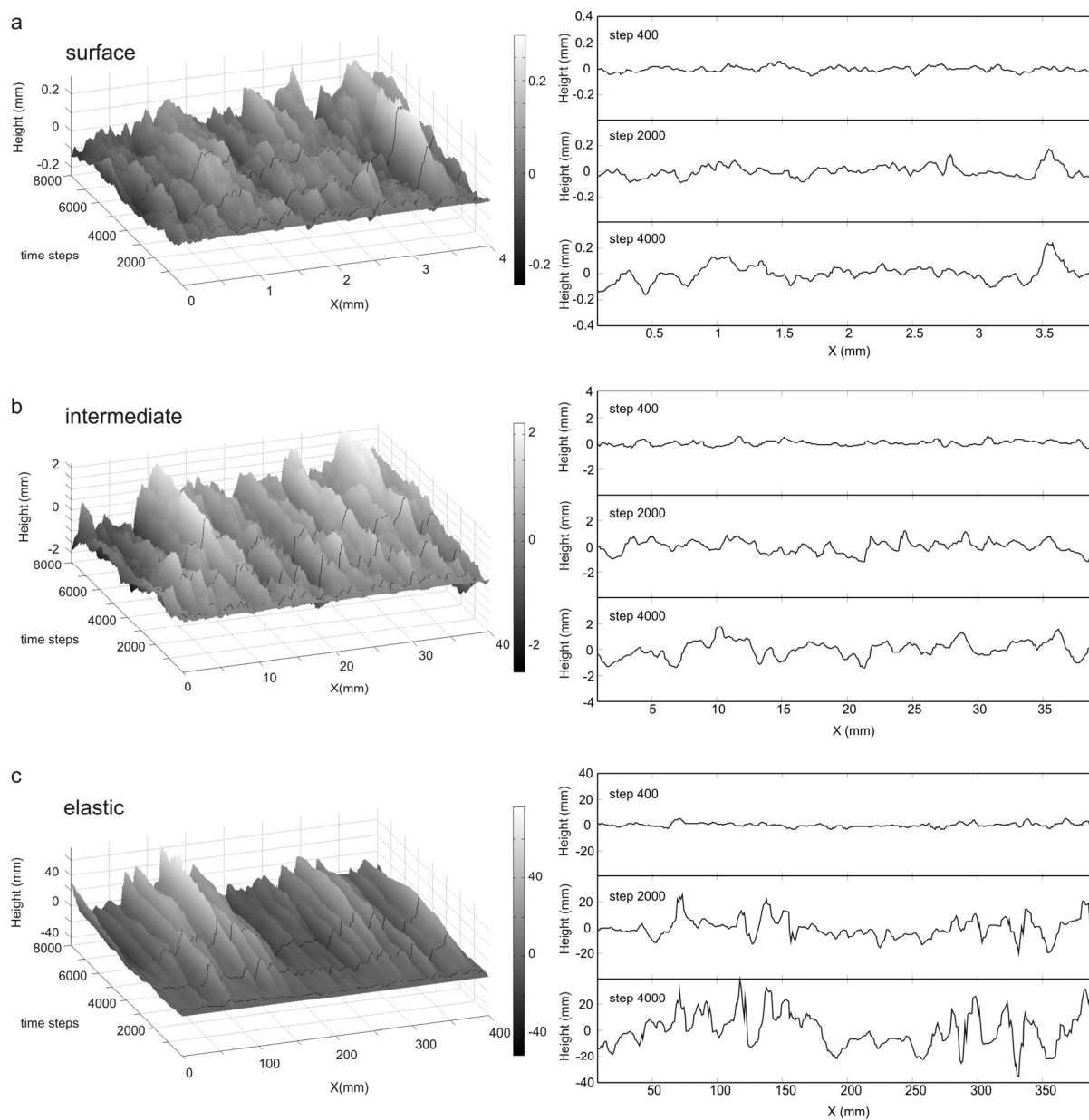


**Figure 5.3** Growth of three stylolites with similar heterogeneities but different lengths and discretization resolution. Left panels show 3D plots of the stylolite growth from a flat interface until the end of the experiment. Right panels show 3 individual deformation steps (step 400, 2000 & 4000) corresponding to the solid lines in the 3D plot **(a)** surface class (box size=0.4 cm) **(b)** intermediate class (box size =4 cm) **(c)** elastic class (box size =40 cm); Notice the disrupted growth of the surface class whereas the elastic class exhibits very continuous growth and pronounced peaks and teeth.

In the *elastic class* individual peaks grow very continuously whereas in the *surface class* the growth is often disrupted, due to dissolution of pinning particles as a result of high surface energies along pronounced peaks.

In the following sections we concentrate on the influence of the noise (amount and pinning factor of the noise particles) on 1) the roughness exponents, 2) the growth exponents and 3) the crossover length.

### 5.3.1. Roughness exponents

To quantitatively characterize the roughness of an individual 1D profile of a stylolite we used concepts from statistical physics (Barabasi and Stanley, 1995), which are briefly introduced in the first part of this section. The methods used here are the same as those of previous studies of natural stylolites (Renard et al., 2004; Schmittbuhl et al., 2004; Gratier et al., 2005; Ebner et al., 2009), which facilitates comparison.

The prerequisite for the application of these scaling methods is that the 1D signal of the numerical stylolite obeys a self-affine scaling invariance, which is given by (e.g. Barabasi and Stanley, 1995)

$$f(bx) \sim b^a f(x), \quad (5.4)$$

where  $f(x)$  is a single valued function and the power-law exponent  $a$  is called *roughness* or *Hurst* exponent and provides a quantitative measurement of the roughness of the signal. A self-affine function must be rescaled differently in  $x$  and  $y$  directions to obtain a scaling invariance i.e. horizontal rescaling of the form  $x \rightarrow bx$ ,  $b$  being a dilation factor, has to be rescaled in the vertical direction by  $y \rightarrow b^a y$  to obtain a scaling invariance. Different statistical methods can be used to evaluate the self-affine character of a signal and to determine the associated roughness exponent. We apply two independent methods in this contribution, the *Fourier method* and the *Average Wavelet Coefficient method*.

The *Fourier method* (e.g. Barabasi and Stanley, 1995; Schmittbuhl et al., 1995) is based on a Fourier transform of the original 1D signal (Fig. 5.4 a). For every 1D signal (every deformation step) the Fourier power spectrum  $P(k)$  i.e., the square of the modulus of the Fourier transform, was calculated as a function of the wave-number  $k$ . Plotting  $P(k)$  as a function of  $k$  in log-log space reveals a linear trend for a self-affine function (Fig. 5.4 b), and the slope is a function of the Hurst exponent through (Renard et al., 2004; Schmittbuhl et al., 2004):

$$P(k) \sim k^{-1-2a} \quad (5.5)$$

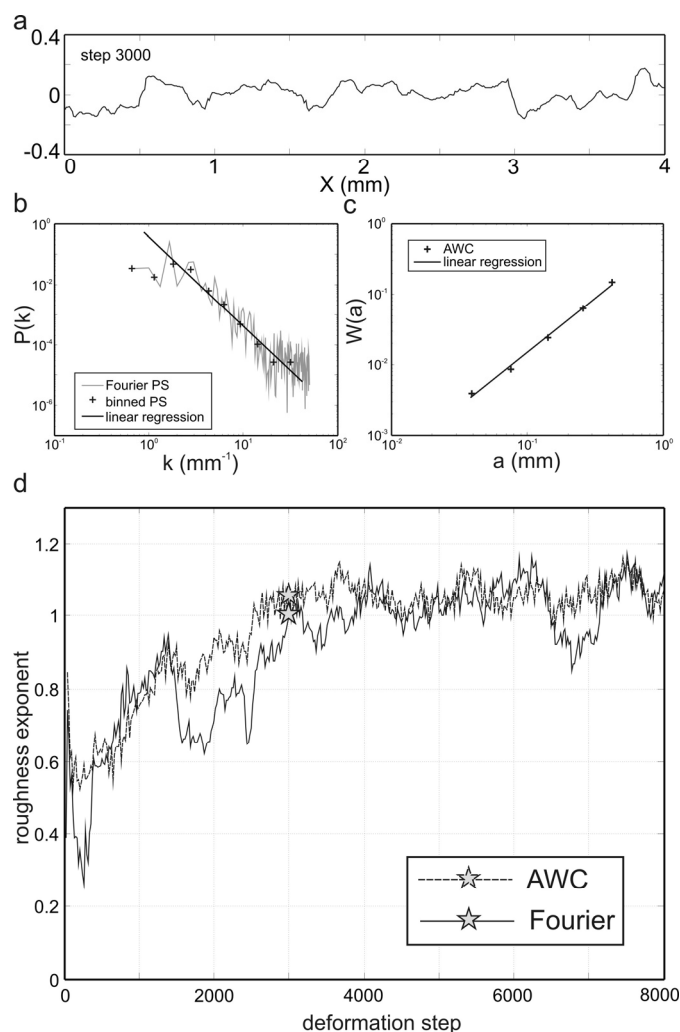


**Figure 5.4** Roughness characterization of single deformation steps by means of the Hurst exponent. **(a)** 1D profile (deformation step 3000) of the surface class with 5% pinning particles and a dissolution rate constant of  $k=0.4$ ; **(b)** Fourier power spectrum  $P(k)$  of the signal from Figure 5.4 a plotted as a function of the wave number  $k$ . Linear regression (solid line) is calculated from the binned spectra (crosses), the slope of the regression is a function of the Hurst exponent, see section 5.3.1 for detailed description. **(c)** Wavelet spectra  $W(a)$  plotted (crosses) as a function of the scaling parameter  $a$  (see average wavelet coefficient-method in section 5.3.1). The slope of the linear regression (solid line) is again a function of the Hurst exponent. **(d)** Evolution of the Hurst exponent in the course of an entire experiment for the Fourier and AWC methods. Stars indicate the Hurst exponent of the 1D signal shown in Figure 5.4 a for the two methods used. Notice the leveling off at a specific Hurst exponent (plateau value) which is characteristic for all simulations.

The *Average wavelet coefficient method* (AWC) was used as a second independent method to confirm the scaling results (Simonsen et al., 1998; Hansen et al., 2000). This method is again based on a decomposition of the 1D signal into wavelets, whose amplitude depends on scale and the position. The wavelet transform is defined after Simonsen et al. (1998) by

$$W_{a,b} = \frac{1}{\sqrt{a}} \int_{-\infty}^{\infty} \varphi\left(\frac{x-b}{a}\right) f(x) dx, \quad (5.6)$$

where  $\varphi$  is the wavelet basis (Daubechies wavelet of order 12), which is parameterized by a scale parameter  $a$  and a translation parameter  $b$ , and  $f$  is the single-valued original function. Finally the wavelet coefficients are averaged over the translation parameter  $b$  for every  $a$  to obtain the average wavelet coefficient  $W(a)$ . If the input signal is self-affine, the wavelet transform verifies that the average wavelet coefficient  $W(a)$  scales as (Simonsen et al., 1998)

$$W(a) \sim a^{\alpha+1/2} \quad (5.7)$$

Plotting the average wavelet coefficients as a function of the scale parameter  $a$  in log-log space (Fig. 5.4 c), the slope of the linear regression through the data is again a function of the Hurst exponent.

Using these two statistical methods, we first study the dynamics of the roughness exponents through time during stylolite growth, and then concentrate on their stability with respect to variations of the noise. The roughness exponents increase relatively quickly in the course of a simulation run (Fig. 5.4 d) and become stable after model step 3000 with only minor fluctuations. The *Fourier-* as well as the *AWC-method* show consistent evolutions and similar values of the roughness exponents. Averages of the plateau values reached (after step 3000) for individual model runs are used as a characteristic value for the roughness exponent for a specific setup. Error bars underline the standard deviation around this average (Fig. 5.5).

The *surface class* is characterized by consistently high values for the Hurst exponent, i.e.  $\alpha \sim 0.9-1.1$ , independent of the pinning factor (i.e. the dissolution rate constant  $\kappa$  in Eq. 5.1; cp Fig. 5.5 a) or the amount of pinning particles (Fig. 5.5 b).

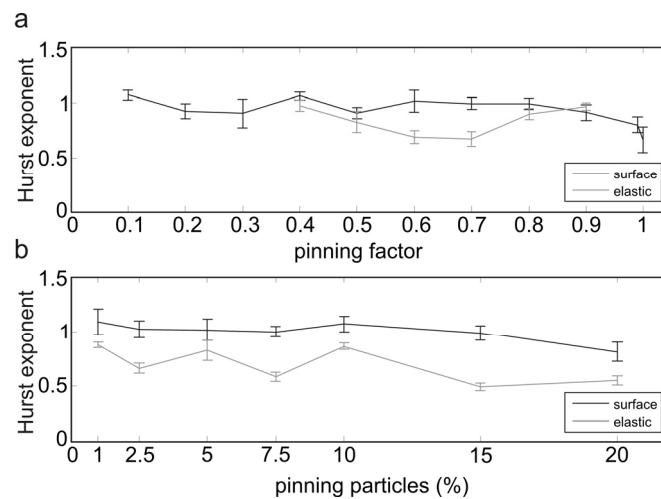


**Figure 5.5** Composite plots showing the plateau roughness (Hurst exponents) for the surface and elastic classes. **(a)** Hurst exponent plotted versus dissolution rate constants  $\kappa$  with a fixed amount of pinning particles of 5% (where  $\kappa=1$  is the dissolution rate of the matrix). **(b)** Hurst exponent plotted versus amount of pinning particles with a dissolution rate constant of  $\kappa=0.5$  for all experiments. The error bars correspond to the standard deviation given by the fluctuation around the plateau values, compare Figure 5.4 d.



The exponents only decrease when the pinning factor of particles is very low (dissolution rate constant  $> 0.9$ ) and the rock becomes homogeneous. The most stable roughness exponents for the surface class are reached in the range 0.1 to 0.8 for the pinning factor and 1 to 20 % of pinning particles.

The *elastic class* reveals lower Hurst exponents ( $\alpha \sim 0.6$  to 0.9) than the *surface class*. If the pinning factor of particles is very strong i.e. particles are very resistant to dissolution (below the value 0.4 for the relative dissolution rate constant in Fig. 5.5 a) stress concentrations are locally too high once two pinning particles meet and artifacts develop (usually anticracks that grow laterally emerge from these concentrations, hence modifying the surface topography) in the numerical model within the *elastic class*. Therefore we did not include values below 0.4 from elastic simulations in Figure 5.5 a. Generally the roughness exponents in the elastic class show stronger fluctuations than those of the surface class. They are relatively stable within a pinning factor range of 0.5 to 0.8 (Fig. 5.5 a) and 1 to 20 % of pinning particles.

The *surface* and *elastic classes* correspond well to the two scaling regimes found in natural stylolites (Renard et al., 2004; Schmittbuhl et al., 2004) that are separated by a crossover-length at the millimeter scale. The roughness exponents of the surface class ( $\alpha \sim 1.1$ ) are in good agreement with analytical predictions and experimental observations (e.g. Gratier et al., 2005). The *elastic class* displays values for the Hurst exponent ( $\alpha \sim 0.6-0.9$ ) that are higher than exponents from natural examples (Renard et al., 2004; Schmittbuhl et al., 2004; Ebner et al., 2009) or analytical predictions, which are generally around 0.5. These analytical predictions are usually based on linear approximations, which are strictly speaking valid as long as the surface morphology is not too developed. The present model does not present any such limitations, and the fully developed situation can thus present a different Hurst exponent from the initial one. The discrepancy with natural data may arise from the large particle (or grain) size that we use in the setup for the elastic class. In nature the grain size is much smaller and corresponds to the values that we use in the surface class.

### 5.3.2. Interface growth

In addition to the dynamic development of the roughness exponents the simulations allow us to study how fast the amplitude of the stylolite roughness grows through (model-) time or as a function of the finite strain. First we concentrate on different growth regimes of stylolites, the associated growth exponents and prefactors of scaling functions and then study the variation of these factors as a function of host-rock heterogeneities. In order to quantify the amplitude of the roughness we use the *interface width* ( $w$ ) that is defined as the root-mean-square fluctuation of the height of the interface for a given time-step (Barabasi and Stanley, 1995)

$$w(L, t) \equiv \sqrt{\frac{1}{L} \sum_{i=1}^L [h(i, t) - \bar{h}(t)]^2}, \quad (5.8)$$

where  $w$  is the interface width as a function of system size  $L$  and time  $t$ ,  $h$  is the height of point  $i$  on the interface at time  $t$  and  $\bar{h}$  the average height of the interface at time  $t$  given by

$$\bar{h}(t) \equiv \frac{1}{L} \sum_{i=1}^L h(i, t). \quad (5.9)$$

In our simulations, the system size  $L$  is defined as the number of elements in the x-direction, which is constant for all simulations, i. e. 400 particles. Roughening processes of interfaces in a wide range of fields have been demonstrated to follow a power law in time (e.g. Barabasi and Stanley, 1995) defined by a growth-exponent  $\beta$  (given by,  $w(L, t) \sim t^\beta$ ). This initial phase of interface growth is usually followed by a second regime during which the interface width reaches a saturation value,  $w_{sat}$ , which is directly related to the system-size.

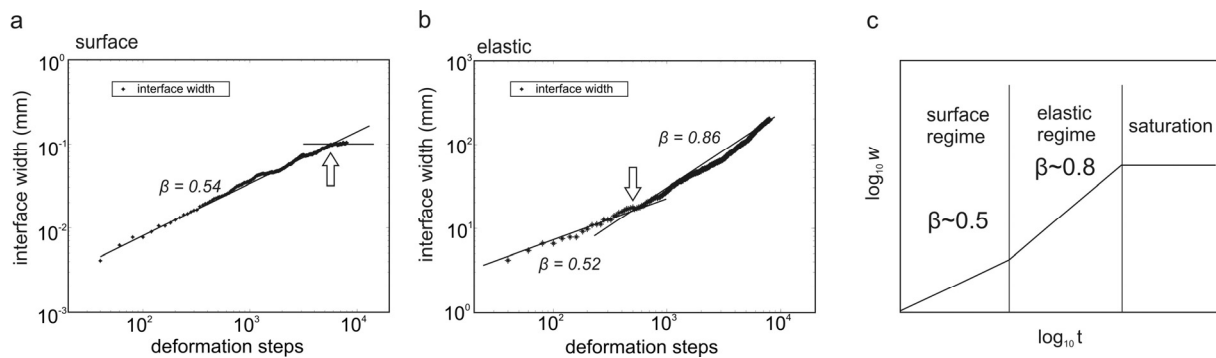


**Figure 5.6** Interface growth depicted by the interface width (Eq. 5.8). **(a)** Log-log plot of the interface width as a function of time in the surface class (5% pinning particles & dissolution rate constant of 0.4). Growth exponent  $\beta=0.5$  is given by the slope of the linear regression (solid line). Notice the saturation point (indicated by arrow) i.e. interface width remains constant during ongoing deformation. **(b)** Log-log plot of the interface width as a function of time in the elastic class (5% pinning particles & dissolution rate constant of 0.4). Notice the two successive growth regimes characterized by an initial growth exponent of  $\beta=0.5$  up to a crossover width (indicated by arrow) followed by an exponent of  $\beta=0.8$ ; no saturation can be observed within the given simulation time. **(c)** Proposed composite graph of the interface growth of simulated stylolites. Two successive growth regimes separated by a narrow crossover width that are dominated either by surface or elastic energies are followed by a saturation of the interface growth due correlation introduced by finite size effects.

Both growth and saturation regimes can be seen in Figure 5.6 a for an experiment of the surface class with a characteristic growth exponent of  $\beta \sim 0.5$ . The arrow in Figure 5.6 a marks the transition from the power law growth regime to the regime where the interface width saturates and stays constant. The *intermediate class* simulations show a similar growth exponent (around 0.5) but do not saturate in the given deformation time. The *elastic class* (Fig. 5.6 b) shows two successive growth regimes, the first being defined by a growth exponent of  $\beta \sim 0.5$  up to a crossover interface width followed by a second regime with  $\beta \sim 0.8$  without reaching the saturation regime. We suggest the following schematic growth regimes (Fig. 5.6 c) for stylolites: (i) growth in the surface energy dominated regime with an exponential growth defined by

$\beta \sim 0.5$  followed by (ii) growth in the elastic energy dominated regime with  $\beta \sim 0.8$  and finally reaching (iii) a saturation regime where the interface width stays constant.

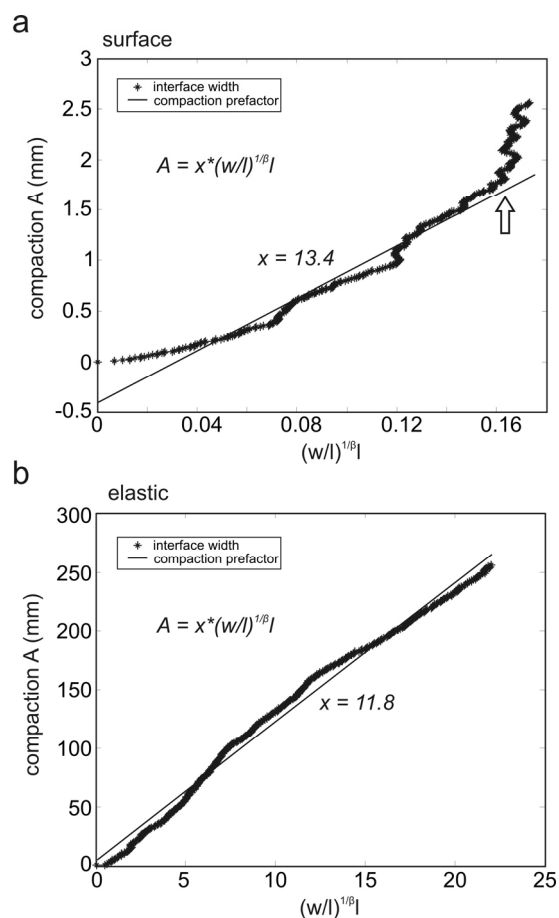


**Figure 5.7** Total compaction displacement expressed as a linear function (solid line) of the interface width and the compaction prefactor (compare Eq. 5.10). **(a)** Surface class experiment (5% pinning particles & dissolution rate constant of  $k=0.4$ ) demonstrates that the relationship is only valid as long as the interface is not saturated i.e. strong deviation from linear trend (compare Figure 5.6 a). **(b)** Elastic class experiment (5% pinning particles & dissolution rate constant of 0.4) reveals an accurate reproduction of the linear relationship (solid line) stated in Equation 5.10. No saturation was observed in the given simulation time.

This strict non-linearity of the interface growth in our simulations suggests that estimated amounts of compaction (here used as synonymous with volume/area loss due to pressure solution) from stylolite amplitude heights (e.g. Tada and Siever, 1989; and references cited therein) only capture a small part of the actual compaction. To cope with this problem, Koehn et al. (2007) demonstrated that the actual displacement can be expressed for the elastic or surface energy dominated growth regimes as a function of the interface width and the growth exponent (as long as the critical saturation time is not reached), given by

$$A \sim (w/l)^{1/\beta} l \quad (5.10)$$

where,  $\mathcal{A}$  is the compaction displacement,  $w$  the interface width,  $\beta$  the growth exponent (for a certain class) and  $l$  the particle size. The slope of this function gives a prefactor for the scaling relation which should remain constant until the saturation time is reached. We call the slope of this relation here and in the subsequent sections *compaction prefactor* because it relates the interface width to the total compaction (Fig. 5.7). As soon as the saturation time is reached the relation does not hold any more and the function deviates from the linear trend. This effect can be observed in Figure 5.7 a where the arrow marks the onset of interface width saturation, where compaction continues through but the interface width (x-axis) remains constant. However, if the saturation is not attained (Fig. 5.7 b) the actual compaction can be calculated accurately from the interface width and the growth exponent using Equation 5.9.

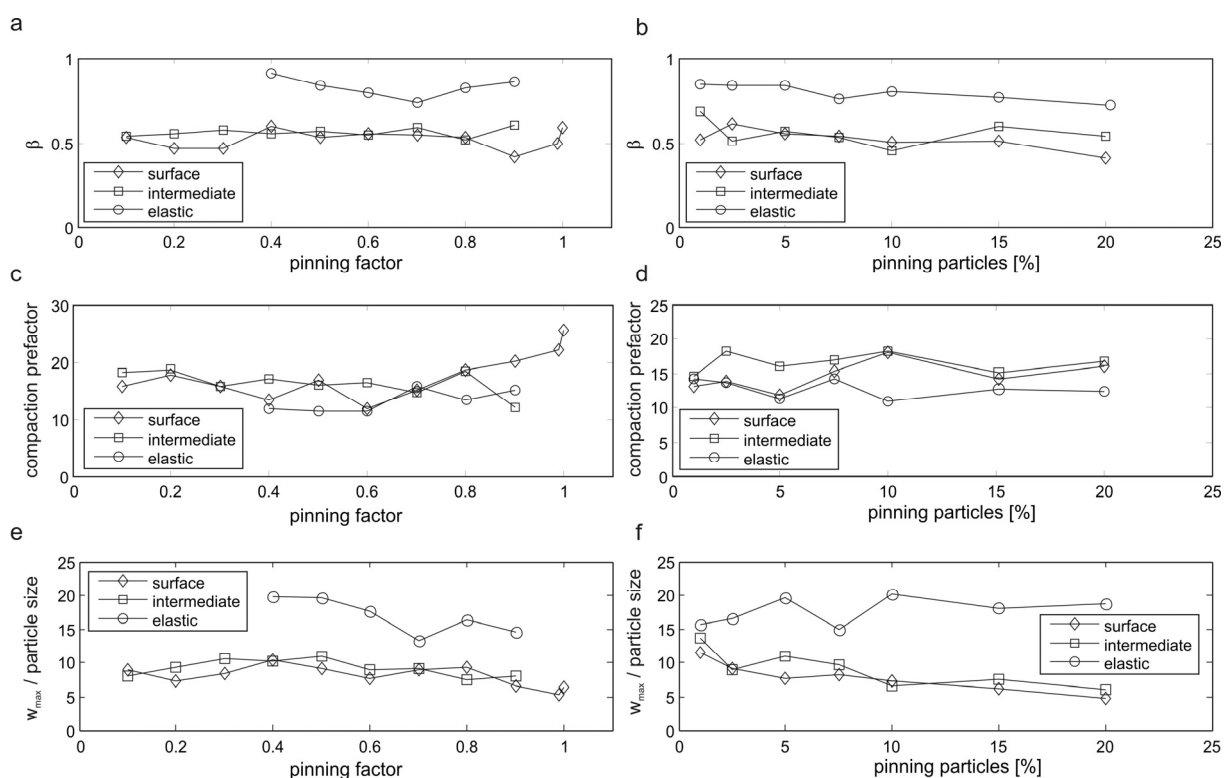


**Figure 5.8** Cumulative data for the surface, intermediate and elastic classes for: **(a)** Growth exponent versus dissolution rate constant (pinning particles fixed at 5%); **(b)** Growth exponent versus amount of pinning particles (dissolution rate constant fixed at  $k=0.5$ ); **(c)** Compaction prefactor versus dissolution rate constant (pinning particles fixed at 5%); **(d)** Compaction prefactor versus amount of pinning particles (dissolution rate constant fixed at  $k=0.5$ ). Maximum interface width normalized by the particle size attained during experimental runs for the *surface*, *intermediate* and *elastic* class **(e)** with changing dissolution rate constant (with 5% pinning particles); **(f)** with changing amount of pinning particles (dissolution rate constant is fixed at 0.5).

Figure 5.8 a demonstrates that neither pinning factor nor amount of pinning particles have a strong effect on the growth exponent. The values for the growth exponent cluster around  $\beta \sim 0.5$  for the *surface* and *intermediate* classes and around  $\beta \sim 0.8$  for the *elastic* class. The compaction prefactors display a higher variability than the growth exponents but no systematic trend can be seen that relates this variation to the pinning factor or amount of pinning particles in the host-rock. Figures 5.8 c & d show that there is no significant difference between the three classes of particle sizes used with values for the compaction prefactor in a range between  $\sim 12$  and  $\sim 25$ . Finally, we compare the maximum interface width normalized

by the particle size ( $w_{max}$ ) that develops during simulations with different heterogeneities (Fig. 5.8 e & f). The largest interface widths are achieved in the *elastic class* with  $w_{max} \sim 20$  in contrast to  $w_{max} \sim 10$  reached in the *intermediate* and *surface class*. Hence the interface growth displays twice the displacement in the *elastic class* in the given simulation time due to the larger growth exponents than those of the *intermediate* or *surface class*, respectively. For the *surface*, *intermediate* and *elastic classes* the variation of the pinning factor of particles (Fig. 5.8 e) have no considerable influence on the maximum interface width. However the amount of pinning particles has a significant influence on the *surface* and *intermediate class* (Fig. 5.8 f). Both classes show an evident decrease in the maximum interface width with increasing amount of pinning particles. This trend cannot be observed in the *elastic class* (Fig. 5.8 f).

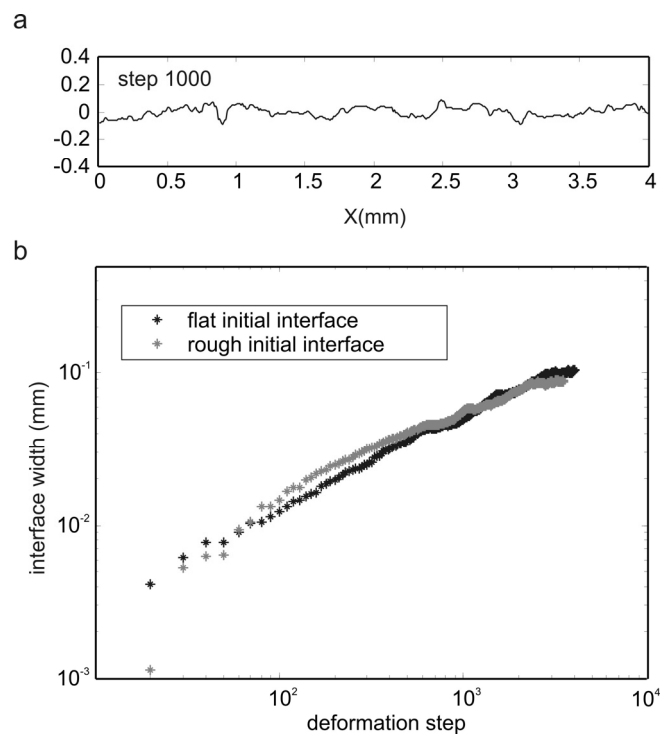


**Figure 5.9** The influence of the topography of the initial predefined interface on the dynamic roughness evolution. **(a)** Rough initial interface used as starting point to evaluate the interface width evolution on top of this roughness for a *surface class* simulation with 5% pinning particles and a pinning factor of 0.5 (for details see text). **(b)** Comparison of the interface width evolution of an initially flat and rough (see Fig. 5.9a) interface. Both interfaces show a similar evolution with growth exponents of 0.54 and 0.51 for the flat and rough initial interface respectively. Notice that both growth and the roughness exponents (not shown) are independent of the initial topography of the predefined interface.

We also tested the influence of the initial shape of the predefined interface separating the two blocks that are pressed together during an experimental run (compare Fig. 5.2a), which is flat in all the simulation data shown in the preceding sections. To investigate the dynamic roughness evolution of an already rough interface we arbitrarily choose a time/deformation step ( $t_n$ ) of a simulation run (Fig. 5.9 a) and subtracted the topography ( $h$ ) of this step from the subsequent time steps similar to  $h(t) = h(t_n + m \cdot \Delta t) - h(t_n)$ . This procedure allows investigation of the dynamic evolution of a rough interface by statistically evaluating the difference of the evolving roughness from time  $t_n$  onwards (Fig. 5.9 b). Departing from an already rough

interface does not change the scaling parameters (growth and roughness exponent) as depicted in Figure 5.9. Hence the model setup we choose in this work (i.e. a flat initial interface) can also account for complex initial topographies.

### 5.3.3. Crossover length scales

The crossover-length of stylolite roughness that separates the surface energy dominated regime from the elastic energy dominated regime is a function of the stress during stylolite growth and can be used as paleo-stress gauge (Renard et al., 2004; Schmittbuhl et al., 2004; Ebner et al., 2009). It is of fundamental importance to know if this crossover is constant when the heterogeneities in the host-rock vary, because this knowledge would facilitate the use of the crossover-length as a quantitative measure of the stress during formation (compare Ebner et al., 2009). In the following section we want to explore how sensitive the crossover-length scale is to variations in the amount and strength of pinning particles. The crossover-length between the two well characterized regimes (i.e., surface energy- and elastic energy- dominated) can be found in the *intermediate class* of our simulations that exhibits two distinct roughness exponents and hence the transition between the two scaling regimes (Fig. 5.10). The Fourier power spectrum of the 1D signal of a stylolite in the intermediate class (Fig. 5.10 b) shows a change from a shallow to a steep slope indicating small and large roughness exponents on large and small scales, respectively. To avoid bias due to improper fitting of the crossover-length we used a nonlinear least square curve fitting algorithm in logarithmic space to model our scaling function (Ebner et al., 2009):

$$f(x) = (a_L x + m_L)(1 - w(x)) + (a_S x + m_S)w(x) \quad (5.11a)$$

and

$$w(x) = \frac{(\tanh(x + L) + 1)}{2}, \quad (5.11b)$$

where  $a_{L,S}$  are the exponents of the scaling function for large and small scales,  $m_{L,S}$  the corresponding intercepts with the ordinate and  $w(x)$  the weighting function. During this procedure the roughness exponents of our nonlinear model function were fixed according to the roughness exponents ( $a_S \sim 1.1$ ;  $a_L \sim 0.5$ ) reported from natural stylolites (Renard et al., 2004; Schmittbuhl et al., 2004; Ebner et al., 2009).

The crossover-lengths obtained for all experiments of the intermediate class are in a range of  $L \sim 1.33 \pm 0.09$  mm, the crossover length usually develops simultaneously with the achievement of the plateau values (compare Fig. 5.4 d). Neither of the quenched noise parameters influenced the crossover-length significantly (Fig. 5.11).

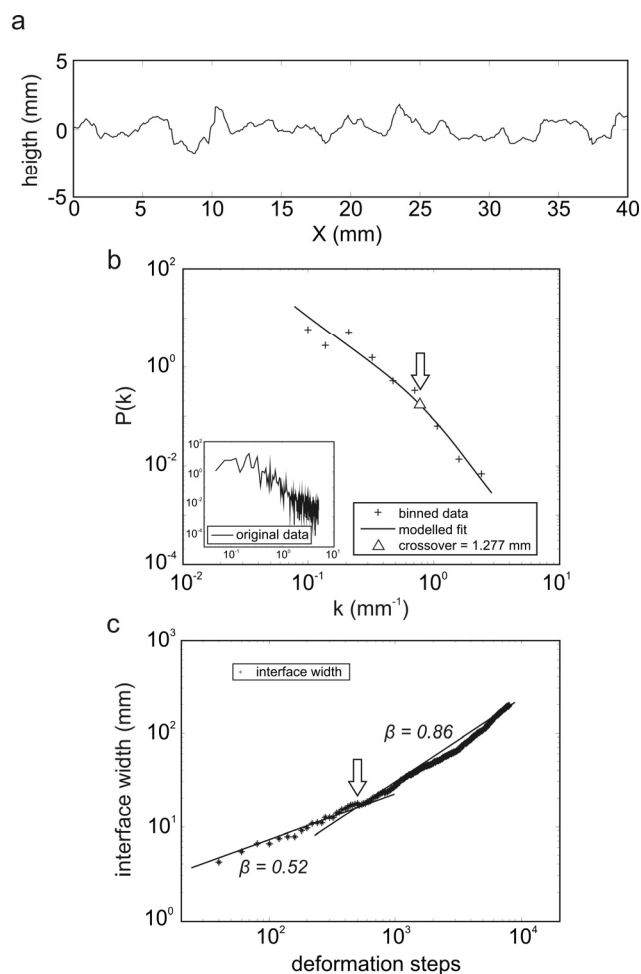


**Figure 5.10** Crossover phenomena in the roughness scaling and interface growth. **(a)** 1D signal of an experiment from the intermediate class (5% pinning particles; dissolution rate constant  $k=0.4$ ); **(b)** Fourier power spectrum (inset) of the signal and binned spectra (crosses). A nonlinear model function (for explanation see text) used to minimize the original data (solid line) is used to accurately locate the position of the crossover length (triangle)  $L=1.27$  mm; **(c)** Log-log plot of the interface width versus time of the elastic class (5% pinning particles & dissolution rate constant  $k=0.4$ ). Notice the two successive growth regimes characterized by an initial growth exponent of  $\beta=0.5$  up to a crossover width  $w=1.24$  mm followed by an exponent of  $\beta=0.8$ . Notice that both crossover scales correspond to the transition from a surface to an elastic energy dominated regime.

The time evolution of the roughness presented in the previous section showed that the surface energy dominated regime is characterized by a growth exponent of 0.5 whereas the elastic energy dominated regime is characterized by a growth exponent of 0.8. However, the surface energy dominated growth can be detected at the beginning of the roughness evolution of the elastic energy dominated regime (Fig. 5.6). Therefore the growth exponents also show a transition (that we term the crossover interface width) between growth in the surface energy dominated regime and growth in the elastic energy dominated regime, similar to the two roughness exponents that are characteristic for these two regimes. The crossover interface width is very consistent for all experiments with  $w \sim 1.23 \pm 0.04$  mm, independent of the quenched noise introduced in the system. We did not observe a crossover in the interface growth of the *intermediate* and *surface* class because the interface width in these classes is simply not large enough to reach the elastic growth regime. Due to the very good correlation between the magnitudes of the

crossover-length and the crossover interface width (Fig. 5.11) we argue that both crossovers arise from the same process, namely the transition from a surface energy to an elastic energy dominated regime.

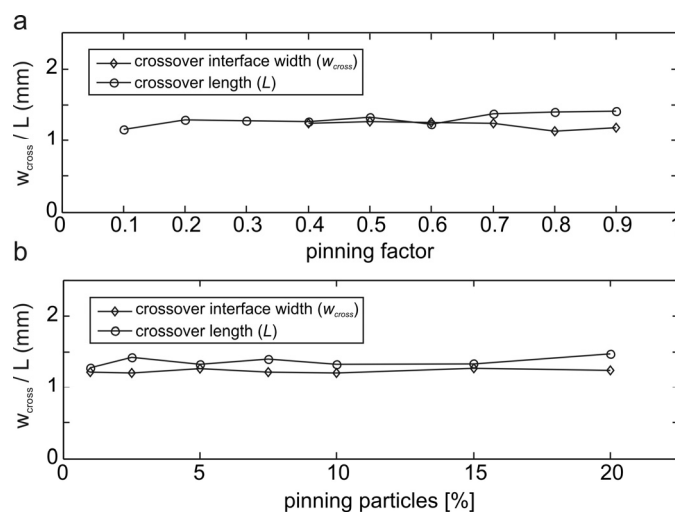


**Figure 5.11** Crossover length  $L$  and crossover interface width  $w$  plotted as a function of the quenched noise. **(a)** Crossover length (circles) calculated from the Fourier power spectrum (cp. Fig. 5.10 b) and crossover interface width (diamonds) for simulations with different dissolution rate constants. **(b)** Crossover length (circles) and crossover interface width (diamonds) for simulations with different amounts of pinning particles.

## 5.4. Discussion

In the following section we first discuss the influence of the quenched noise on the scaling parameters in our numerical simulations, deal with the relevance of the noise and compare the results to natural stylolites. Secondly, we focus on the crossover phenomena and their significance for the estimate of volume loss along a finite natural stylolite.

The influence of the exact nature of the heterogeneities (i.e. pinning factor, amount and size of pinning particles) on the scaling exponents can be directly investigated by a close examination of Figures 5.5, 5.8 and 5.11. The pinning factor has the least influence on the roughness and growth exponents as well as on the crossover scaling ( $L$  and  $w_{\text{cross}}$ ), resulting in values that are very consistent over wide ranges of the parameter space. The amount of pinning particles only shows an influence on the maximum interface width  $w_{\text{max}}$ , which decreases with increasing amount of heterogeneities (Fig. 5.8 f). This fact is in agreement with qualitative observations made on natural stylolites that stylolite amplitudes decrease with the amount of heterogeneities (e.g. Tada and Siever, 1989; and references cited therein). The scaling exponents themselves are independent of the amount of pinning particles. The biggest influence seems to be exerted by the particle sizes. But these differences have been shown to arise (Renard et al., 2004; Schmittbuhl et al., 2004; Koehn et al., 2007) from a transition from surface energy dominated smoothing to elastic energy dominated smoothing. The differences in the scaling exponents between the experimental classes are therefore not caused by the heterogeneities themselves but by the processes that govern the roughening on respective scales. We are thus convinced that the influence of the exact



nature of the heterogeneities plays a minor role and that roughening is dominated by an inherent process that depends on the length-scale.

The quenched noise we introduced in the different simulations, i.e. changes in the dissolution rate constant that influence the dissolution velocity of a particle (compare. Eq. 5.1), represents simple chemical noise as pointed out by Koehn et al. (2007). We are aware that along natural stylolitic interfaces the elastic parameters, surface energies and crystallographic orientations change, in addition to chemical variations. However, the effects of change in these other parameters in our model will ultimately result in a change of the dissolution velocity. We therefore argue that for the developing structure it should make no difference what the exact nature of the noise is, since any particle with a slower dissolution velocity will pin the surface and therefore cause a roughening of the interface.

It was demonstrated that individual natural stylolites from different outcrop localities and lithologies, i.e. different host-rock compositions, reveal the same scaling behavior (e.g. Renard et al., 2004; Schmittbuhl et al., 2004; Ebner et al., 2009). Consequently the investigation of these natural stylolites corroborates the evidence that a common underlying mechanism for the roughening of the investigated stylolites can be assumed rather than a roughening that is dominated by the composition of the host rock.

Nevertheless we do not claim that knowledge of the exact nature or distribution of the material heterogeneities is unimportant. Brouste et al. (2007) have shown that a changing amount of heterogeneities might cause a stylolite to become a non-stationary signal with alternating wavy and flat portions along the interface. This study also demonstrates that correlated quenched noise only influences the stylolite morphology above a crossover-length scale, implying that two scaling regimes, which can be connected to surface and elastic energy dominated roughening (e.g. Renard et al., 2004; Schmittbuhl et al., 2004), can also be found in the case of correlated noise. We have not investigated the effects of irregularly distributed (correlated) noise since the heterogeneities are distributed equally in our model setup.

The roughness data of simulated stylolites presented in this study reveal two self-affine scaling regimes that are separated by a distinct crossover-length of  $L \sim 1.3$  mm, which is well in line with investigations of natural stylolites (Renard et al., 2004; Schmittbuhl et al., 2004, Ebner et al., 2009). Additionally we have detected a crossover in the growth of the interface during which the initial growth exponent of  $\beta \sim 0.5$  up to a crossover interface width of  $w \sim 1.23$  mm is replaced by a growth regime with an exponent of  $\beta \sim 0.8$ . Due to the very good correlation between the magnitudes of the crossover-length and the crossover interface width we argue that both crossovers arise from the same process, namely the transitions from a surface energy to an elastic energy dominated regime. The knowledge of the crossover length  $L$  which can be derived from the finite pattern of a natural stylolite with the above methods is thus equivalent to knowledge of the crossover interface width. This fact has important consequences regarding the assessment of the amount of total compaction of individual stylolites. Substituting the growth exponents and the compaction prefactors found for the two growth regimes in combination with the crossover-length, which separates the two growth regimes (compare Fig. 5.10 c), into Equation 5.10 should allow an approximate reconstruction of the amount of total compaction from finite pattern of a natural stylolites.

## 5.5. Conclusions

In the course of this study we evaluated the scaling properties of simulated stylolites, which facilitate a quantitative comparison with natural examples, reproducing their scaling. We observed only minor correlation between the exact nature of the noise introduced in the model or the topography of the predefined interface and the scaling parameters investigated, concluding that inherent processes, i.e. the transition from a surface to an elastic energy dominated regime, control the roughening process.

Nevertheless the amount of heterogeneities has a negative effect on the maximum interface width ( $w_{max}$ ) achieved during deformation, revealing increasing interface width with decreasing amount of quenched noise. The absolute particle/noise size influences the roughness and growth exponents, which in turn is caused by the transition from a surface to an elastic energy dominated regime. Therefore it is important to know how large the noise or pinning particles are in natural systems. The transition from surface energy as the dominant stabilizing force of the interface to the dominance of elastic energies causes the most significant scaling transitions: (i) the roughness is characterized by two distinct spatial scaling regimes on small and large length scales, respectively; (ii) the interface growth reveals two growth regimes with a growth exponent of  $\beta \sim 0.5$  up to a crossover interface width that coincides with the crossover-length  $L$  followed by a growth regime with an exponent of  $\beta \sim 0.8$  that eventually saturates due to finite size effects; (iii) the crossover interface width  $w$  coincides with the crossover-length  $L$  and thus allows to accurate reconstruction of the compaction history of finite stylolite patterns.

Our study corroborates the evidence that the simple mechanisms summarized above support analytical predictions and natural observations given in previous studies, and are a convincing cause for the formation of stylolite roughness. However a detailed study on the exact nature and distribution of quenched noise in the host rocks of natural stylolites would shed light on the origin and initiation of these complex structures.

## 5.6. References

- Barabasi, A.L., Stanley, H.E., 1995. Fractal concepts in surface growth. Cambridge University Press.
- Bathurst, R.G.C., 1987. Diagenetically Enhanced Bedding in Argillaceous Platform Limestones - Stratified Cementation and Selective Compaction. *Sedimentology* 34, 749-778.
- Bons, P.D.D., Koehn, D., Jessell, M.W., 2008. Microdynamics Simulation. In: *Lecture Notes in Earth Sciences* (edited by Friedmann, G. M. & Seilacher, A.) 106. Springer, Berlin, 406.
- Brouste, A., Renard, F., Gratier, J.P., Schmittbuhl, J., 2007. Variety of stylolites' morphologies and statistical characterization of the amount of heterogeneities in the rock. *Journal of Structural Geology* 29, 422-434.

- Buxton, T.M., Sibley, D.F., 1981. Pressure Solution Features in a Shallow Buried Limestone. *Journal of Sedimentary Petrology* 51, 19-26.
- Clark, S.P.J., 1966. *Handbook of Physical Constants*. Geological Society of America, New York.
- Dunnington, H.V., 1954. Stylolite development post-dates rock induration. *Journal of sedimentary Petrology* 24, 27-49.
- Ebner, M., Koehn, D., Toussaint, R., Renard, F., Schmittbuhl, J., 2009. Stress sensitivity of stylolite morphology. *Earth and Planetary Science Letters*(277), 394-398.
- Fletcher, R.C., Pollard, D.D., 1981. Anti-Crack Model for Pressure Solution Surfaces. *Geology* 9, 419-424.
- Gratier, J.P., Muquet, L., Hassani, R., Renard, F., 2005. Experimental microstylolites in quartz and modeled application to natural stylolitic structures. *Journal of Structural Geology* 27, 89-100.
- Guzzetta, G., 1984. Kinematics of Stylolite Formation and Physics of the Pressure-Solution Process. *Tectonophysics* 101, 383-394.
- Hansen, A., Schmittbuhl, J., Batrouni, G.G., de Oliveira, F.A., 2000. Normal stress distribution of rough surfaces in contact. *Geophysical Research Letters* 27, 3639-3642.
- Heald, M.T., 1955. Stylolites in Sandstones. *Journal of Geology* 63, 101-114.
- Katsman, R., Aharonov, E., Scher, H., 2006. A numerical study on localized volume reduction in elastic media: Some insights on the mechanics of anticracks. *Journal of Geophysical Research-Solid Earth* 111, B03204.
- Karcz, Z., Scholz, C.H., 2003. The fractal geometry of some stylolites from the Calcare Massiccio Formation, Italy. *Journal of Structural Geology* 25, 1301-1316.
- Koehn, D., Dysthe, D.K., Jamtveit, B., 2004. Transient dissolution patterns on stressed crystal surfaces. *Geochimica et Cosmochimica Acta* 68, 3317-3325.
- Koehn, D., Malthe-Sorensen, A., Passchier, C.W., 2006. The structure of reactive grain-boundaries under stress containing confined fluids. *Chemical Geology* 230, 207-219.
- Koehn, D., Renard, F., Toussaint, R., Passchier, C.W., 2007. Growth of stylolite teeth patterns depending on normal stress and finite compaction. *Earth and Planetary Science Letters* 257, 582-595.
- Merino, E., 1992. Self-organization in stylolites. *American Scientist* 80, 466.
- Merino, E., Calas, A., Fletcher, R.C., 2006. Genesis of self-organized zebra textures in burial dolomites: Displacive veins, induced stress, and dolomitization. *Geologica Acta* 4, 383-393.
- Park, W.C., Schot, E.H., 1968. Stylolites: their nature and origin. *Journal of sedimentary Petrology* 38, 175-191.
- Railsback, L.B., 1993. Lithologic Controls on Morphology of Pressure-Dissolution Surfaces (Stylolites and Dissolution Seams) in Paleozoic Carbonate Rocks from the Mideastern United-States. *Journal of Sedimentary Petrology* 63, 513-522.
- Railsback, L.B., 1998. Evaluation of spacing of stylolites and its implications for self-organizations of pressure dissolution. *Journal of Sedimentary Research* 68, 2-7.
- Renard, F., Schmittbuhl, J., Gratier, J.P., Meakin, P., Merino, E., 2004. Three-dimensional roughness of stylolites in limestones. *Journal of Geophysical Research-Solid Earth* 109, B3209.

- Rutter, E.H., 1983. Pressure solution in nature, theory and experiment. *Journal of the Geological Society of London* 140, 725-740.
- Schmittbuhl, J., Vilotte, J.P., Roux, S., 1995. Reliability of Self-Affine Measurements. *Physical Review E* 51, 131-147.
- Schmittbuhl, J., Renard, F., Gratier, J.P., Toussaint, R., 2004. Roughness of stylolites: Implications of 3D high resolution topography measurements. *Physical Review Letters* 93, 238501.
- Simonsen, I., Hansen, A., Nes, O.M., 1998. Determination of the Hurst exponent by use of wavelet transforms. *Physical Review E* 58, 2779-2787.
- Stockdale, P.B., 1922. Stylolites: their nature and origin. *Indiana University Studies* 9, 1-97.
- Tada, R., Siever, R., 1989. Pressure Solution during Diagenesis. *Annual Review of Earth and Planetary Sciences* 17, 89-118.

## 6. Synthesis and general conclusions

Based on the work presented in the previous chapters of this thesis, a general conclusion is presented here. As outlined in the introduction, this work focused on three distinct aspects of stylolites (i) a quantitative description of the stylolite morphology and the implications for the formation conditions, namely the stress state; (ii) the cause for the initiation of stylolite roughness and finally to a subordinate amount (iii) on the origin and initiation of localized pressure solution. These topics are addressed in detail in the specified order in this chapter. At the end a short outlook and suggestion for further research is given which results from questions arisen in the course of this thesis and shortcomings of this work.

### 6.1. Scaling of natural stylolites

This thesis reports 1D and 2D scaling analysis of natural stylolites in limestones of both bedding parallel (chapter 2) and bedding normal (i.e. tectonic) stylolites (chapter 3). It is demonstrated that 1D stylolite signals, i.e. intersections normal to the stylolite plane, obey a fractal scaling over several orders of magnitude (Drummond & Sexton 1998, Karcz & Scholz 2003). However, only the investigations of the full topography of opened interfaces revealed that stylolites exhibit a self-affine scaling invariance (Renard et al. 2004, Schmittbuhl et al. 2004), with distinct roughness exponents for small and large length scales, which are separated by a crossover length at the millimeter scale. Analytical considerations of these authors demonstrated that these scaling regimes coincide with thermodynamic regimes for which the roughening is either balanced by surface energies or elastic energies that work against a quenched material disorder inducing the roughness on small and large scales.

Based on this pioneering approach (Renard et al. 2004, Schmittbuhl et al. 2004) the current work demonstrates that 1D signals of bedding parallel stylolites exhibit two self-affine scaling regimes with characteristic Hurst or roughness exponents of  $\sim 1.1$  and for small and  $\sim 0.5$  at large length scales i.e. below and above the millimeter scale. In addition the scaling of the crossover-length ( $L$ ) with the normal stress on the interface during formation as analytically predicted was verified in the field. Analyzing samples from different depths in a sedimentary basin in southern France reveals that the crossover-length decreases in a nonlinear fashion with increasing formation depth and thus increasing normal stress. Using the expected relation  $L \sim \sigma^{-2}$  (where  $\sigma$  is the stylolite formation stress or the normal stress on the interface) reasonable absolute stress magnitudes can be deduced from the crossover length using relevant material parameters. This result entails two significant conclusions: First, the morphology of a bedding parallel stylolite contains a signature of the stress field during formation and thus can be used as quantitative stress gauge. Second, because the formation of bedding parallel stylolites is due to the layer

normal overburden good estimates of the depth of formation of the stylolites can be made and the depositional history of sedimentary basins can be assessed.

Extending this procedure to tectonic stylolites is less trivial, since for tectonic stylolites the principal stress is (sub)-vertical and the in-plane stresses are dissimilar which in turn does not allow simplifications used for bedding parallel stylolites. Chapter 3 reports the scaling analysis of such tectonic stylolites from two different tectonic settings in SW Germany and NE Spain. 1D signals of tectonic stylolites reveal the same characteristics as bedding parallel stylolites, showing two distinct self-affine scaling regimes separated by a well defined crossover length. Investigation the full surface morphology of opened stylolite interfaces by means of high resolution laser profilometry allows to study all possible orientations within the stylolite plane, revealing that a scaling anisotropy of the crossover length exists. But neither the scaling exponents, i.e. the Hurst exponents, nor the scaling prefactor, i.e. the topothesy (Simonsen et al. 2000, Schmittbuhl et al. 2008), are modified. Since the samples were taken oriented in the field, the anisotropy can be correlated spatially to the vertical and horizontal directions. All samples showed that the largest crossover length scales coincide with the vertical direction ( $\sigma_2$ ) and the smallest with the horizontal direction ( $\sigma_3$ ). This relationship demonstrates that the in-plane scaling anisotropy is a function of the 3D stress field during formation, since the crossover length scales inversely to the in-plane differential stress of tectonic stylolites. In addition, effect of synthetic self affine surfaces with teeth oriented different than  $90^\circ$  to the mean plane about which they fluctuate, which is a definition for slickolites (Simon 2007), is studied. These synthetic surfaces reveal that the anisotropy introduced by varying inclination of the teeth introduces a different anisotropy (i.e. anisotropy of the small length scales). This allows to conclude that tectonic stylolites, although similar to bedding parallel stylolites in their 1D scaling behavior, show a strong in-plane scaling anisotropy of the crossover-length which can be related to the 3D stress field during formation. Tectonic stylolites also contain a signature of the stress field but require more prerequisites to estimate the stress magnitudes than bedding parallel stylolites. In addition it is necessary to investigate the 3D morphology of tectonic stylolites to capture the full complexity of their scaling.

## 6.2. Initiation of stylolite roughness

To investigate the cause of the formation and initiation of the intriguing roughness of stylolites is the second focus of this thesis. The two main concepts prevailing in the literature claim that either a stress-induced instability (Gal & Nur 1998, Gal et al. 1998, Angheluta et al. 2008, Bonnetier et al. 2009) or heterogeneities initially present in the host rock (Renard et al. 2004, Schmittbuhl et al. 2004, Brouste et al. 2007, Koehn et al. 2007, Ebner et al. 2009) cause the pressure solution surface to roughen. To address this issue a twofold approach is used founded on microstructural analysis and numerical modeling. First a microstructural approach based on SEM/EBSD analysis combined with orientation contrast (OC) imaging is used to investigate the distribution of material disorder in limestones hosting stylolites. Careful examination of initial (micro)-stylolites i.e. stylolites which have not formed a continuous layer of residual material, reveals that virtually all asperities along the stylolite interface are occupied by a single or clumps

of clay particles on the convex side of the interface. This observation provides strong arguments for heterogeneities as a cause for the roughness. Furthermore the quenched disorder is made up of varying composition e.g. quartz grains, clay particles on several orders of magnitude to form a polymict multi scale quenched noise. The distribution of heterogeneities seems to be quasi-random and no clear spatial correlation exists on the observed scales. In addition the grain size and shape analysis of the calcite matrix around the stylolites exhibit considerable modifications in the vicinity of the stylolite which can not be observed away from the stylolite. For the investigated samples a possible influence of the soft sediment deformation or compaction during diagenesis can be excluded as a reason for the matrix modifications around the stylolite.

Second, a numerical approach based on a 2D linear elastic spring model developed by Koehn et al. (2007), is used to study the development of stylolite roughness from an initially flat fluid filled interface. The quenched noise initially present in the material is varied systematically i.e. the size, amount and dissolution rate of heterogeneities in the system, which controls the roughening. Quantitative investigation of the evolving structure shows that the roughness and growth exponents (i.e. the morphology and the rate at which the morphology develops) are independent of the exact nature of the heterogeneities. The evolving interface is characterized by two self-affine scaling regimes separated by a crossover length at the millimeter scale. Therefore the numerical results resemble very closely the scaling of natural stylolites. A crossover length scale exists in space and time which separates scaling regimes for which the roughening and the rate at which this roughness grows is either balanced by surface or elastic energies. The rate at which the roughness evolves is strictly nonlinear and eventually saturates due to finite size effects. This has important implications for the assessment of the volume loss along stylolites. As long as the stylolite is not saturated the root-mean-square width of the interface only gives a minimum of the volume loss along the interface. Knowledge of the growth exponents and the crossover length would enable one to decipher the exact amount of volume lost during pressures solution. If however the stylolite interface is saturated, equivalent with the cessation of the roughness growth, the stylolite roughness loses its memory for the amount of volume change. Conventional methods assessing the amount of volume change thus tend to highly underestimate the volume lost along individual stylolite interfaces. In summary, it can be concluded that stylolite roughness is induced by heterogeneities initially present in the host rock. Nevertheless, only the position of the evolving asperity along the interface is determined by the heterogeneity, whereas inherent processes, i.e. the transition of a surface to an elastic energy dominated regime, control the roughening process and thus the morphology.

### **6.3. Formation of localized pressure solution features**

What causes the formation of localized pressure solution surfaces and how these features propagate is not a primary focus of this work, but some analysis performed in the course of this thesis allow indirect conclusions of why and how localized pressure solution features form.. This work provides arguments for two of the three prevailing mechanisms argued for the formation of localized pressure solution surfaces,

i.e. the formation along preexisting planar anisotropies (Bathurst 1987) and by local stress concentration which drive the lateral propagation similar to anticracks (Fletcher & Pollard 1981).

Preexisting planes of anisotropy are considered important for two reasons. Anisotropy planes e.g. bedding planes for horizontal stylolites or joints for tectonic stylolites are necessary to produce stylolites with teeth not normal to the mean pressure solution plane i.e. slickolites (Simon 2007). In the investigated field areas in southern France (chapter 2) and northeastern Spain (chapter 3) the pressure solution surfaces caused by horizontal compression have the orientation of preexisting joint sets but the teeth point to in the direction of the far field compression which is not normal to the plane about which the roughness fluctuates. This thus implies that the pressure solution is accommodated along a preexisting plane of anisotropy. In addition the numerical model used in chapter 5 demonstrated that stylolite teeth track the compression direction independent of how the far field compression is oriented with respect to the imposed flat interface (Koehn et al. 2007) thus corrugating the evidence for the formation along a preexisting surface. Microstructural investigation of bedding parallel stylolites (chapter 4) showed that stylolites have a certain tendency to form along planes of changes in the compositional layering e.g. grain size variation, but these stylolites are not limited to these changes in compositional layering.

Secondly, observations made by Fletcher and Pollard (1981) on natural stylolites which lead to the thought-concept of anticracks can be supported by this work in two aspects: The tapering of the roughness towards the tips and bending of the step-over between overlapping adjacent stylolite terminations suggests that that stylolites propagate laterally from a nucleation site. In addition the artifacts in the numerical model reported in chapter 5 show exactly this behavior. These artifacts are anticracks which develop on peaks of pronounced stylolite teeth when two pinning particles at opposing sides of the interface meet. The development of anticracks only occurs if the pinning strength is very high (i.e. the dissolution rate is low compared to the matrix), which enable stress concentrations that allow the dissolution of lateral grains. Thus, both field observations and numerical models provide arguments for a lateral propagation from a local site of stress concentration.

In summary, it can be argued that the formations along preexisting planar anisotropies as well as the anticrack concept facilitate anisotropies, one punctiform, the other planar, which allow stress concentrations. It is thus concluded that a combined mechanism of planar and/or punctiform anisotropies cause the formation of localized pressure solution surfaces such as stylolites, due to stress concentrations.

## 6.4. Outlook: suggestion for further research

This work does not claim to investigate or explain all issues of stylolite formation but shed light on some of the key topics necessary for a wider understanding of this complex subject. Several important issues of stylolites were not addressed in this thesis, either simply because they are beyond the scope of this work due to timely constraints, or arose during the course of this subject. Some of these will be addressed in this chapter.



The utilization of the scaling methods presented in this study relies on one important assumption: the signal has to be stationary. This means that the statistics of the signal does not vary along the strike of the interface. Brouste et al. (2007) pointed out that this is not necessarily the case for stylolites and found that stylolite morphology can be non-stationary and thus have wavy portions which alternate with flatter ones. If this is the case the methods used here fail to capture the roughness property from a scaling property. Brouste et al. (2007) further argue that non-stationary stylolites are the expression of the distribution of the heterogeneities in the host rock and therefore only local scaling exponents can be deduced reliably. Using such elaborate methods to investigate the local scaling properties of stylolites might allow extracting more intrinsic parameters from stylolite roughness and thus infer more about stylolite formation.

Microstructural analysis of the heterogeneities has shown that various impurities can impose the formation of roughness along stylolite interfaces. But rough calcite-calcite interfaces demonstrate that the identified heterogeneities only scratch the surface of the full range of possible noise, even in a monomineralic rock. In addition to different phases and crystallographic orientation of the major matrix mineral, a detailed chemical analysis is necessary to identify how a possible compositional variation of the major matrix mineral influences the roughness evolution of stylolites. Furthermore it is crucial to investigate the distribution of insoluble particles and their enrichment in the residual layer quantitatively (Renard et al. 2004). Thus a chemical mapping technique is suggested (e.g. nuclear microprobe) with a resolution down to the  $\mu\text{m}$ -scale. This technique should be combined with the scaling analysis of Brouste et al. (2007) to investigate the effect of non-uniformly distributed heterogeneities. The knowledge gained from this combined approach would allow constructing numerical models with a more realistic distribution and composition of the quenched noise and thus enable to refine growth exponents which are necessary to estimate the amount of volume loss along a stylolite interface from the finite morphology.

A last point to be mentioned here is the investigation of stylolites and their surrounding host rock with X-ray computer tomography (XCT). Preliminary results on stylolites in limestones and (gold bearing) quartz not reported in this thesis indicate that the residual (clay) layer shows a complex aperture scaling. This residual layer reduces to a minimum around pronounced peaks and reaches a maximum where the topography is rather flat. This has important implications for the pressure solution process along the interface and for fluid flow along the stylolite interface. Especially for ‘fractured’ hydrocarbon reservoirs and gold deposits the understanding of fluid flow along stylolites is very important both for scientific and economic reasons. The  $\mu\text{m}$  scale spatial resolution of XCT presently available allows the investigation of the complete system and thus the aperture scaling without mechanical opening of the interface and consequently permit the investigation of the “undisturbed” stylolite structure.

## 6.5. References

- Angheluta, L., Jettestuen, E., Mathiesen, J., Renard, F. & Jamtveit, B. 2008. Stress-Driven Phase Transformation and the Roughening of Solid-Solid Interfaces. *Physical Review Letters* 100(9), 096105.
- Bathurst, R. G. C. 1987. Diagenetically Enhanced Bedding in Argillaceous Platform Limestones - Stratified Cementation and Selective Compaction. *Sedimentology* 34(5), 749-778.
- Bonnetier, E., Misbah, C., Renard, F., Toussaint, R. & Gratier, J. P. 2009. Does roughening of rock-fluid-rock interfaces emerge from a stress-induced instability? *The European Physical Journal B - Condensed Matter and Complex Systems* 67(1), 121-131.
- Brouste, A., Renard, F., Gratier, J. P. & Schmittbuhl, J. 2007. Variety of stylolites' morphologies and statistical characterization of the amount of heterogeneities in the rock. *Journal of Structural Geology* 29(3), 422-434.
- Drummond, C. N. & Sexton, D. N. 1998. Fractal structure of stylolites. *Journal of Sedimentary Research* 68(1), 8-10.
- Ebner, M., Koehn, D., Toussaint, R. & Renard, F. 2009. The influence of rock heterogeneity on the scaling properties of simulated and natural stylolites. *Journal of Structural Geology* 31(1), 72-82.
- Fletcher, R. C. & Pollard, D. D. 1981. Anticrack model for pressure solution surfaces. *Geology* 9(9), 419-424.
- Gal, D. & Nur, A. 1998. Elastic strain energy as a control in the evolution of asymmetric pressure-solution contacts. *Geology* 26(7), 663-665.
- Gal, D., Nur, A. & Aharonov, E. 1998. Stability analysis of a pressure-solution surface. *Geophysical Research Letters* 25(8), 1237-1240.
- Karcz, Z. & Scholz, C. H. 2003. The fractal geometry of some stylolites from the Calcare Massiccio Formation, Italy. *Journal of Structural Geology* 25(8), 1301-1316.
- Koehn, D., Renard, F., Toussaint, R. & Passchier, C. W. 2007. Growth of stylolite teeth patterns depending on normal stress and finite compaction. *Earth and Planetary Science Letters* 257(3-4), 582-595.
- Renard, F., Schmittbuhl, J., Gratier, J. P., Meakin, P. & Merino, E. 2004. Three-dimensional roughness of stylolites in limestones. *Journal of Geophysical Research-Solid Earth* 109(B3), -.
- Schmittbuhl, J., Renard, F., Gratier, J. P. & Toussaint, R. 2004. Roughness of stylolites: Implications of 3D high resolution topography measurements. *Physical Review Letters* 93(23), -.
- Schmittbuhl, J., Steyer, A., Jouniaux, L. & Toussaint, R. 2008. Fracture morphology and viscous transport. *International Journal of Rock Mechanics and Mining Sciences* 45(3), 422-430.
- Simon, J. L. 2007. Analysis of solution lineations in pebbles: Kinematical vs. dynamical approaches. *Tectonophysics* 445(3-4), 337-352.
- Simonsen, I., Vandembroucq, D. & Roux, S. 2000. Wave scattering from self-affine surfaces. *Physical Review E* 61(5), 5914.

## 7. Appendix

The appendix contains the most important *Matlab*® scripts and functions developed for the data analysis in this thesis. All scripts and functions are written in *Matlab*® 7.5 and should be compatible to *Matlab*® 7.0-7.xx. These scripts use built-in functions which require the additional Wavelet toolbox (Appendix A) Optimization Toolbox (Appendix A,B & C). The *Matlab*® scripts and functions documented in this Appendix can be employed by copy/paste of the text into the *Matlab*® editor.

### 7.1. Appendix A

Appendix A contains the scripts developed for Chapter 2. These scripts are used in Chapter 3 & 5 as well. script: *fourier1D\_workflow.m*, function: *fourier1D.m*; *logbin1D.m*; *nonlin\_fourier\_diff.m*; *nonlin\_fourier\_model.m*; *awc1D.m*

```
% FOURIER_1D_WORKFLOW demonstrates the workflow for data analysis:
% used in Chapter 2 of this thesis and in Ebner et al. 2009, EPSL
% -from a digitized stylolite to the calculation of the crossover-length-
% self-written functions called during execution of this script (in order
% of appearance):
%   fourier1D.m
%   logbin1D.m
%   nonlin_fourier_diff.m
%   nonlin_fourier_model.m

% load a manually digitized dataset:
load data_NavaS14.mat h x dx

% h -> heights of a 1D signal
% x -> x-positions of discrete measurements
% dx-> distance between measurements

% remove any linear trend from the data
h1 = detrend(h);

%plot the stylolite
figure (1)
plot (x,h1);
title('stylolite');
xlabel ('x [mm]'), ylabel ('y [mm]'), axis equal;

% calculate the Fourier power spectrum
[k,ps] = fourier1D(h1,dx);

% do a logarithmic binning of the power spectrum
intervall = 1.5; % define intervall
[x_av,y_av] = logbin1D(k,ps,intervall);

% plot original and binned power spectrum in log-log space
figure (2)
loglog(k(2:end),ps(2:end),'r',x_av(2:end),y_av(2:end),'b*-');
title ('Power spectrum')
legend('original data','binned data');
hold on
```

```

xlabel('k (mm-1)'); ylabel('power spectrum');

% non-linear data fitting (using the built in function LSQNONLIN) to
% estimate the crossover length L
% set options for LSQNONLIN
options = optimset('Largescale','off','MaxFunEvals', 500);

% define dataset used for minimization
X = x_av(2:end);
Y = y_av(2:end);

% STARTING GUESS MINIMIZATION:
%CASE 1: minimization for Lx* and Ly* (Hs & Hl are fixed)
l1 = [1 1];
%CASE 2: minimization for L*, hL*, Hs and Hl
l2 = [1 1 1 0.5];

% Invoke optimization using LSQNONLIN (see Matlab help for details)
[new_L,resnorm] = lsqnonlin(@nonlin_fourier_d,l1,[],[],options,X,Y);

%calculate the model with minimized coefficients
samplevector = linspace(min(X),max(X),500);
Y_bin        = nonlin_fourier_m(new_L,samplevector);

% Plot the original and modeled data with fixed slopes
figure (3)
loglog (X,Y,'+r',samplevector,exp(Y_bin),'b'),hold on;
loglog (1/new_L(1),new_L(2),'*g')
title ('binned and modeled data')
legend ('original data','modelled fit',...
        sprintf('%s %1.3f %s', 'crossover =',new_L(1),'mm'))
xlabel ('k [mm-1]', ylabel('power spectrum');
%%%%%%%%%%%%%%%%%%%%%%%%%%%%%%%%%%%%%%%%%%%%%%%%%%%%%%%%%%%%%%%%%%%%%%%%

function [k,ps] = fourier1D(profX,pixel_size)
% FOURIER1D calculates the power spectrum of a 1D signal
%Input parameters:
% profX      => a linearly spaced vector containing the hights of a 1D-signal
% pixel_size => distance betweenen points of the vector profX
% Output parameters:
% k          => wave number (m-1)
% ps         => power spectrum

% calculate the power spectrum
nx = length(profX);
fftx = fft(profX);
ps = fftx .* conj(fftx)/length(profX);
ps = ps(1:length(profX)/2+1);

%calculate the wave number (k)
length_distance = nx*pixel_size;
deltaf          = 1./length_distance;
k               = deltaf:deltaf:1./pixel_size;
k               = k(1:length(k)/2+1);
%%%%%%%%%%%%%%%%%%%%%%%%%%%%%%%%%%%%%%%%%%%%%%%%%%%%%%%%%%%%%%%%%%%%%%%%

function [k_av,ps_av]=logbin1D(k,ps,interval)
% LOGBIN1D does a logarithmic binning (i.e. the average of all points in a
% certain interval in log-space) of the Fourier power spectrum as
% calculated from the fourier1D function. This gives a power spectrum with
% a constant density in log-space.
%
% INPUT VARIABLES:
% k          -> wave number of the power spectrum
% ps         -> power spectrum over the range of k
% interval   -> binning interval (=log(interval))
% OUTPUT VARIABLES:
% k_av       -> linear vector containing averaged wave numbers
% ps_av      -> linear vector containing averaged power spectra

```

```

% logarithmize the input variables
x      = log(k);
y      = log(ps);
bin_size = log(interval);

% initialize first interval
start  = min(x);
ende   = start + bin_size;
i=1;

while ende <= max(x)
    x_ind = find(start<=x & x<ende);
    y_av(i) = mean(y(x_ind)');
    x_av(i) = mean(x(x_ind)');
    start  = ende;
    ende   = ende+bin_size;
    i      = i+1;
end

k_av   = exp(x_av);
ps_av  = exp(y_av);

%%%%%%%%%%%%%%%%%%%%%%%%%%%%%%%%%%%%%%%%%%%%%%%%%%%%%%%%%%%%%%%%%%%%%%%%

function c = nonlin_fourier_d(l,k,ps)
% The function NONLIN-FOURIER_D describes the nonlinear behaviour of the
% Fourier power spectrum (= fx as a function of L* and Ly) and calculate the
% differences between the function as input for the LSQNONLIN
% function.
% LSQNONLIN minimizes the differences by finding new L* and Ly* values.
%
% INPUT VARIABLES:
%   l  =>   a [1 2] vector containing starting guess for L* and Ly*
%   k  =>   wave numbers from dataset
%   ps =>   power spectrum from dataset
% OUTPUT VARIABLE:
%   c  =>   vector containing the differences between original and
%           modeled data for all points in the data range

% INITIALISE AND DEFINE THE VARIABLES USED
c      = zeros(size(k));
fx     = zeros(size(k));

x      = log(k);           % x values of input data
L      = l(1);             % L* crossover length
Ly     = l(2);             % Ly* y-value of L*

if length(l) == 2          %CASE 1: minimize only L* and Ly*
    Hs  = 1.1;             % predefined Hurst exponents Hs & Hl
    Hl  = 0.5;
else                        %CASE 2: minimize for L*, Ly*, Hs and Hl
    Hs  = l(3);             % Hs & Hl from starting guess
    Hl  = l(4);
end

alpha_s = (-1-2*Hs);       % slope of the function (small scale)
alpha_l = (-1-2*Hl);       % slope of the function (large scale)
a        = log(Ly) + alpha_l*log(L); % intercept of function (large scale)
b        = log(Ly) + alpha_s*log(L); % intercept of function (small scale)
sx       = (tanh(x+log(L))+1) ./2; % weighting function

% calculate the model and the difference between original and the model
for i=1:length(x)
    fx(i) = ((a + alpha_l*x(i)) * (1-sx(i))) + ((b + alpha_s*x(i)) * (sx(i)));
    c(i)  = log(ps(i))-fx(i) ;
end
c = c';                    % produce a column vector for output
%%%%%%%%%%%%%%%%%%%%%%%%%%%%%%%%%%%%%%%%%%%%%%%%%%%%%%%%%%%%%%%%%%%%%%%%

```

```

function c = nonlin_fourier_m(l,k)
%The function NONLIN-FOURIER_M calculates the modeled data using the
%minimized output values from LSQNONLIN over the defined data range.
% INPUT VARIABLES:
%   l   =>   a vector containing L* and Ly*
%   k   =>   data range to calculate the fit
% OUTPUT VARIABLE:
%   c   =>   vector containing modeled data in log-space values

% INITIALISE AND DEFINE INPUT AND LOCAL VARIABLES
c = zeros(size(k));

x   =   log(k);           % data range
L   =   l(1);            % crossover L*
Ly  =   l(2);            % y-value of crossover L*

if length(l) == 2        %CASE 1: minimize only L and Ly
    Hs = 1.1;            % predefined Hs & Hl
    Hl = 0.5;
else                      %CASE 2: minimize for L*, hL*, Hs and Hl
    Hs = l(3);           % Hs & Hl from starting guess
    Hl = l(4);
end

alpha_s = (-1-2*Hs);     % slope of the function (small scale)
alpha_l = (-1-2*Hl);     % slope of the function (large scale)
a        = log(Ly) + alpha_l*log(L); % intercept of function (large scale)
b        = log(Ly) + alpha_s*log(L); % intercept of function (small scale)
sx       = (tanh(x+log(L))+1)./2;   % weighting function

for i = 1:length(x)
    c(i) = ((a + alpha_l*x(i))*(1-sx(i))) + ((b + alpha_s*x(i))*(sx(i)));
end
c = c';
%%%%%%%%%%%%%%%%%%%%%%%%%%%%%%%%%%%%%%%%%%%%%%%%%%%%%%%%%%%%%%%%%%%%%%%%

function [a,awc] = awc1D(profX,pixel_size)
% AWC1D computes the averaged wavelet coefficient spectrum of a 1D profile
% following the approach of Simonsen et al. (1998)
% This functions requires the MATLAB WAVELET TOOLBOX!
% Input parameters:
% profX      => a linearly spaced vector containing the heights of a
%              1D-signal
% pixel_size => distance between points of the vector profX
% Output parameters:
% a          => scale parameter (m^-1)
% awc       => averaged wavelet coefficient spectrum

% Daubechies wavelet of order 4 used as basis

N      = wmaxlev(length(profX),'db4');
[C,L] = wavedec(profX,N,'db4');

for i = 1:N
    a(i) = 2*pixel_size*L(length(L))/L(length(L)-i);
    D    = detcoef(C,L,i);
    awc(i) = mean(abs(D));
end
%%%%%%%%%%%%%%%%%%%%%%%%%%%%%%%%%%%%%%%%%%%%%%%%%%%%%%%%%%%%%%%%%%%%%%%%

```

## 7.2. Appendix B

Appendix B contains the scripts used in Chapter 3. In addition Chapter 3 utilizes the scripts presented in Appendix A. script: *fourier2D\_workflow.m*; functions: *fourier2D.m*; *data\_mod.m*; *topot.m*; *synthetic\_signal.m*;

```
% This script demonstrates the data-analysis workflow of 2D topography data
% from high resolution laser profilometry of stylolite surfaces (Chapter 3
% of this thesis)
% self-written functions called during execution of this script (in order
% of appearance):
%   data_mod.m
%   fourier2D.m

% load height data of a regular square grid
load map_m4_3_dat_asc_cal.mat Z

[Z_tape] = data_mod(Z);           %remove trend & do a data windowing
[z_new]  = fourier2D(Z_tape,2);   %calculate the 2D FFT

% Create a double log map of the Fourier transform////////////////////////////////////
n        = length(z_new);
x        = -(n-1)/2:(n-1)/2;
y        = -(n-1)/2:(n-1)/2;
[X,Y]    = meshgrid(x,y);        % Cartesian XY coordinates
[T,R,Z]  = cart2pol(XY, z_new);  % Cartesian -> polar coordinates
r_new    = log(abs(R));          % logarithmise the RHO component
% of the polar coordinates
[X,Y,Z]  = pol2cart(T,r_new,Z);  % polar -> Cartesian coordinates

% 2D logarithmic binnig
%(to create a constant spacing of data points in log(kx)-log(ky) space)
m        = X(end,end);
xl       = linspace(-m,m,26);
xl2      = xl(2:end-1);
[Xs Ys]  = meshgrid(xl2,xl2);    %Cartesian coordinates of new grid
bs       = abs(xl(1)-xl(2));      %BINSIZE
Zs       = zeros(size(Xs));

% find all x/y pairs that fall in one 2D-bin and calculate the mean
for i = 1:length(Ys)
    j = 1;
    for j = 1:length(Xs)
        ind = find((Xs(1,i)-bs/2)<=X & X<(Xs(1,i)+bs/2)&...
            (Ys(j)-bs/2)<=Y & Y<(Ys(j)+bs/2));
        bin = Z(ind);
        Zs(j,i) = mean(bin(:));
    end
end

% Plot the original and binned data
figure (3)

subplot (221)
surf(X,Y,log(Z))
shading interp, axis equal, axis tight, view([0 0])
colormap gray
title('log(orig. data)')

subplot (222)
plot3(Xs, Ys, log(Zs),'+')
axis equal, xlabel('kx'), ylabel('ky')
legend(sprintf('Binsize: %1.2f',abs(bs)), 'Location', 'NorthWest')
title('log(binned data)')
```

```

subplot (223)
surf(Xs, Ys, log(Zs))
axis equal, shading faceted, xlabel('kx'), ylabel('ky')
title('log(binned data)')

subplot (224)
[C,h]=contourf(Xs, Ys, log(Zs), (2:2:22));
surface(Xs,Ys,log(Zs),'EdgeColor',[0.8 0.8 0.8],'FaceColor','none')
grid off
view(-15,25)
xlabel('x'), ylabel('y')
title('log(binned data)')
%%%%%%%%%%%%%%%%%%%%%%%%%%%%%%%%%%%%%%%%%%%%%%%%%%%%%%%%%%%%%%%%%%%%%%%%

function [H_tape]=data_mod(H)
%DATA_MOD does a series of pre-treatments to decrease bias in dataset. First
% linear trends are removed from the data; that the height-field is set to
% have zero mean and finally the data is forced to taper of to zero at the
% ends.
% INPUT VARIABLE:
%   H       =>   a 1D vector or 2D matrix containing the output from the
%               1D/2D Fourier transform.
% OUTPUT VARIABLE:
%   H_tape=>   the modified/pre-treated dataset (see above description)

if isvector(H)                                % input-data is a 1D vector
    win      = hann(length(H));                % create 1D Hanning window
    H_de     = detrend(H);
    H_de     = H_de-mean(H_de(:));
    H_tape   = H_de(:).*win;

    figure
    subplot(221)
    plot(H)
    xlim([0 length(H)])
    title('raw data')
    subplot(222)
    plot(H_de)
    xlim([0 length(H_de)])
    title('detrended data')
    subplot(223)
    plot(win)
    xlim([0 length(win)])
    title('hanning window')
    subplot(224)
    plot(H_tape)
    xlim([0 length(H_tape)])
    title('detrended & windowed data')
else
    % input-data is a 2D map
    % crop to square grid with odd number of points (to have a single
    % data point in the center of the map)
    if mod(min(size(H)),2)
        snew  = min(size(H));
    else
        snew  = min(size(H))-1;
    end
    H        = H(1:snew,1:snew);
    H_de     = detrend(H);
    H_de     = H_de-mean(H_de(:));
    win      = hann(length(H));                % create a 2D Hanning window
    win      = meshgrid(win,win);
    win      = win.*win;
    H_tape   = H_de.*win;

    figure
    subplot (221)
    imshow (H,[min(H(:)) max(H(:))])
    title ('raw data')
    subplot (222)

```



```

    imshow (H_de,[min(H_de(:)) max(H_de(:))])
    title ('detrended data')
    subplot (223)
    imshow (win)
    title ('2D hanning window')
    subplot (224)
    imshow (H_tape,[min(H_tape(:)) max(H_tape(:))])
    title ('detrended & windowed data')
end
%%%%%%%%%%%%%%%%%%%%%%%%%%%%%%%%%%%%%%%%%%%%%%%%%%%%%%%%%%%%%%%%%%%%%%%%

function [Z_new]=fourier2D(Z,i)
%FOURIER2D calculates the 2D Fourier transform of a square surface
% INPUT VARIABLES:
%   Z => heights of a stylolite surface on a regular square grid
%   i => optional input variable; a number that gives a figure number
%       in which the Fourier transform should be exported
% OUTPUT VARIABLE:
%   Z_new => map containing the 2D Fourier transform with the same size
%           as Z. Note that the center represents the largest length
%           scales.

Z1 = fft2(Z);
Z2 = fftshift(Z1);
Z_new = (abs(Z2));

if nargin>1
    figure(i)
    h=imshow(Z_new,[min(min(Z_new)) max(max(Z_new))]);
    colormap(gray),colorbar;
    set(h,'CDataMapping','direct')
    title('2D FFT')
    xlabel('k_x'), ylabel('k_y')
end
%%%%%%%%%%%%%%%%%%%%%%%%%%%%%%%%%%%%%%%%%%%%%%%%%%%%%%%%%%%%%%%%%%%%%%%%

function [p,t]=topot(profile,pixelsize)
% TOPOT calculates the topothesis i.e. the scaling prefactors of a 1D-signal
% extracted from the surface (e.g. Simonsen et al. 2000). The scaling
% prefactor and thus the topothesis for the small and large scale regimes
% can be found by intersection of the two sub-branches of the scaling
% function with the 1/1 line.
% INPUT VARIABLE:
%   profile => vector containing the hights of a 1D signal
%   pixel size => distance between discrete measurements
% OUTPUT VARIABLE:
%   p => scaling (roughness) exponents
%   t => topothesy for small and large length scale

profile = detrend(profile);
% calculate the correlation function (Barabasi & Stanley 1995)
[lag,cor] = HH_cor(profile,pixelsize);

% crop the correlation function
lag = lag(2:length(profile)/2);
cor = cor(2:length(profile)/2);
% date binning to get
[lag_av,cor_av] = bin(lag,cor);

llog_av = log(lag_av);
lcor_av = log(cor_av);

Hs= 0.6; % scaling exponents are fixed to these values
Hl= 0.3;
% use a nonlinear fit to find the position of the crossover length L. The
% crossover length is then used to separate the small and large length
% scales
[L,Ly,new_L] = nonlin(lag_av,cor_av,Hs,Hl,'fix','yess');

%calculate the linear fit for the small scale regime and the topothesy

```

```

As    = [1 Hs; 1 1];
intercept_s = -(log((1/new_L(1))*Hs) + log(new_L(2)));
bs    = [intercept_s; 0];
topos = As\bs;
ts    = exp(topos(1));
ys    = polyval([Hs intercept_s],llag_av);

%calculate the linear fit for the large scale regime and the topothesy
Al    = [1 H1; 1 1];
intercept_l = -(log((1/new_L(1))*H1)+log(new_L(2)));
bl    = [intercept_l; 0];
topol = Al\bl;
tl    = exp(topol(1));
yl    = polyval([H1 intercept_l],llag_av);

% plot the graphical reconstruction of the topothesy
figure (1),clf
plot (log(lag),log(cor),'r*' ,llag_av,lgcor_av,'bo'), hold on
plot (llag_av ,llag_av, 'b--',llag_av,ys,'r--',llag_av,yl,'r--')
plot (topos(1),topos(1),'dg',topol(1),topol(1),'dg')
plot (log(1/new_L(1)),log(new_L(2)),'gd')

p = [Hs H1];
t = [ts tl];
%%%%%%%%%%%%%%%%%%%%%%%%%%%%%%%%%%%%%%%%%%%%%%%%%%%%%%%%%%%%%%%%%%%%%%%%
%LOCAL SUBFUNCTIONS%%%%%%%%%%%%%%%%%%%%%%%%%%%%%%%%%%%%%%%%%%%%%%%%%%%%%%%%%%%%%%%%%%%%%%%%
%%%%%%%%%%%%%%%%%%%%%%%%%%%%%%%%%%%%%%%%%%%%%%%%%%%%%%%%%%%%%%%%%%%%%%%%
function [lag,cor] = HH_cor(profX,pixel_size)
%calculate the correlation function (Barabasi & Stanley 1995 p. 303)
cor = linspace(0,length(profX)-2,length(profX)-2);
lag = cor*pixel_size;
i = 1;
while i < (length(profX)-1)
    j = 1;
    hav = 0;
    count = 0;
    while j < (length(profX)-i)
        h = profX(j) - profX(j+i);
        h = h^2;
        hav = hav + h;
        j = j + 1;
        count = count + 1;
    end
    hav = hav / count;
    hav = hav^0.5;

    cor(i) = hav;
    i = i + 1;
end
%%%%%%%%%%%%%%%%%%%%%%%%%%%%%%%%%%%%%%%%%%%%%%%%%%%%%%%%%%%%%%%%%%%%%%%%
function [x_av,y_av]=bin(x,y)
% do a logarithmic binning (compare Appendix A)
x = log(x);
y = log(y);
bin = 1.5;
start = min(x);
bin_size = log(bin);
ende = start + bin_size;
i=1;

while ende <= max(x)
    x_ind = find(start<=x & x<ende);
    y_av(i) = mean(y(x_ind)');
    x_av(i) = mean(x(x_ind)');
    i = i+1;
    start = ende;
    ende = ende+bin_size;
end

x_av = exp(x_av);

```

```

y_av = exp(y_av);
%%%%%%%%%%%%%%%%%%%%%%%%%%%%%%%%%%%%%%%%%%%%%%%%%%%%%%%%%%%%%%%%%%%%%%%%%%%%%%
function [L,Ly,new_L]=nonlin(k,ps,hs,h1,set,output)
%NONLINFIT calculates the nonlinear fit of a function using the definition
%of Ebner et al., 2008 EPSL; NONLINFIT uses the built-in optimization
%function LSQNONLIN with NONLINFIT_COR_DIFF (to minimize the
%difference between the original data and the modeled fit) and
%NONLIN_FOURIER_MODEL (to plot the modeled fit)
% compare functions in Appendix A for details.

X = k; % data range
Y = ps; % original data

% STARTING GUESS MINIMIZATION:
l1 = [0.5 1];
options = optimset('Largescale','on','MaxFunEvals',1000);

% Invoke optimization using LSQNONLIN
[new_L,resnorm] = lsqnonlin(@nonlin_cor_diff,l1,[0.5,0.01],[2,0.5],...
options,X,Y,hs,h1);
L = new_L(1);
Ly = new_L(2);

% Plot the original and modeled data.
% calculate the model with minimized coefficients
if strcmp(output,'yess')
    samplevector = linspace(min(X),max(X),500);
    Y_bin = nonlin_cor_model(new_L(1:2),samplevector,hs,h1);
    figure
    loglog(X,Y,'+r',samplevector,exp(Y_bin),'b'),hold on;
    plot(1/new_L(1),new_L(2),'*g')
    title('modeled fit')
    legend('original data',...
    sprintf('%s %3.3f, ','fit with norm of redsidual=',resnorm),...
    sprintf('%s %1.3f %s', 'crossover =',1/L,'mm'))
end
%%%%%%%%%%%%%%%%%%%%%%%%%%%%%%%%%%%%%%%%%%%%%%%%%%%%%%%%%%%%%%%%%%%%%%%%%%%%%%
function c = nonlin_cor_diff(l,k,ps,hs,h1)
% The function NONLIN_cor_diff describes the nonlinear behavior of the
% correlation function and calculates the differences between the original
% and the model for all points in the data range to create a vector valued
% function as input for the LSQNONLIN function.
% compare functions in Appendix A for details.

c = zeros(size(k));
fx = zeros(size(k));
x = log(k);
L = l(1);
hL = l(2);

if nargin == 5 & length(l)==2
    Hs = hs;
    Hl = h1;
else
    Hs = l(3);
    Hl = l(4);
end

alpha_s = Hs;
alpha_l = Hl;
a = log(hL) + alpha_l*log(L);
b = log(hL) + alpha_s*log(L);
sx = (tanh(x+log(L))+1)./2;

for i=1:length(x)
    fx(i) = ((b + alpha_s*x(i))*(1-sx(i))) + ((a + alpha_l*x(i))*(sx(i)));
    c(i) = log(ps(i))-fx(i);
end
c = c';
%%%%%%%%%%%%%%%%%%%%%%%%%%%%%%%%%%%%%%%%%%%%%%%%%%%%%%%%%%%%%%%%%%%%%%%%%%%%%%

```

---

```

function c = nonlin_cor_model(l,k,hs,hl)
%The function NONLIN-FOURIER_MODEL calculates the modelled data using the
%minimized output values from LSQNONLIN over the defined data range.
% compare functions in Appendix A for details.
c = zeros(size(k));
fx = zeros(size(k));
x = log(k);
L = l(1);
hL = l(2);

if nargin == 4 & length(l) == 2
    Hs = hs;
    Hl = hl;
else
    Hs = l(3);
    Hl = l(4);
end

alpha_s = Hs;
alpha_l = Hl;
a = log(hL) + alpha_l*log(L);
b = log(hL) + alpha_s*log(L);
sx = (tanh(x+log(L))+1)./2;

for i=1:length(x)
    c(i) = ((b + alpha_s*x(i))*(1-sx(i))) + ((a + alpha_l*x(i))*(sx(i)));
end
c=c';
%%%%%%%%%%%%%%%%%%%%%%%%%%%%%%%%%%%%%%%%%%%%%%%%%%%%%%%%%%%%%%%%%%%%%%%%

%Generate a synthetic self-affine signal following the approach of Meheust
%& Schmittbuhl 2001 PAGEOPH.

N = 400; %matrix size
Y = (randn(N)-0.5)*2; %generate white noise between [-1,1]
delta= 1;

%calculate the frequencies
n = zeros(size(Y));
l = -N*N/2;

for aa=1:N;
    for bb=1:N;
        n(aa,bb)=1;
        l=l+1;
    end
end

fx = n/(N*N*delta);
fy = n'/(N*N*delta);
kx = 2*pi*fx;
ky = 2*pi*fy;
kn = sqrt((kx).^2+(ky).^2);

% Fourier transform of the white noise and shift the zero frequency
% component to the center
Yfft = fft2(Y);
H = fftshift(Yfft);

%define the topological dimension and roughness exponent (zeta)
d = 2;
zeta = 0.5;
g = zeros(size(Y));

for i = 1:N
    for j = 1:N
        g(i,j)= abs(kn(i,j)).^(-d/2-zeta)*(H(i,j));
    end
end
end

```

```

%create self-affine surface of size N^2
g      = fftshift(g);
sa_surf = ifft2(g,N,N);

% plot the rough surface
figure(1)
surf(abs(sa_surf))
axis equal
shading interp
title(sprintf('surface with a Hurst exponent of = %1.1f',zeta))
%%%%%%%%%%%%%%%%%%%%%%%%%%%%%%%%%%%%%%%%%%%%%%%%%%%%%%%%%%%%%%%%%%%%%%%%

```

### 7.3. Appendix C

Appendix C contains the scripts written for Chapter 5. In addition Chapter 5 utilize the scripts presented in Appendix A. Script: *exp\_data\_workflow.m*; *read\_exp\_output.m*, function: *data\_width.m*

```

% Script explores the amplitude width evolution, growth exponent,
% compaction displacement and compaction prefactor of simulated stylolites
% using the model from Koehn et al. 2007 & Ebner et al. 2009
% self-written functions called during execution of this script:
%   data_width

load ('0.15_0.5_0.04.mat');           % load dataset

w      = data_width(Y_mat(1:400,:));   % calculate the interface width
w_log  = log(w);                       % log width data
x_log  = log(1:20:8000);               % deformation steps

%plot width evolution
figure (1);
loglog (1:20:8000, w,'b*'), hold on;
xlabel ('deformation step'),
ylabel ('amplitude width [mm]');
title ('interface width');

% cut off for linear fit
fit_low = 2;
fit_hi  = 400;

% calculate linear fit (slope of the fit is the growth exponent)
[p,s]   = polyfit(x_log(fit_low:fit_hi),w_log(fit_low:fit_hi),1);
y_fit   = polyval(p,x_log);
beta    = p(1);                        % growth exponent

% plot linear fit ontop of the width evolution
figure(1)
loglog(exp(x_log),exp(y_fit),'r');

% model defined compaction per deformation step in mm
comp    = 0.00004 *2 ; % top and bottom are moved in (1 = boxsize)
box_size = dx*400;    % particle size times number of particles
mod_comp = (1:20:8000)*comp*box_size; %compaction per 20 steps

% linear scaling relation of Koehn et al. 2007 for the stylolite growth as
% a function of the compaction
A       = ((w./dx).^1/beta)*dx;        % Eq. 13 Koehn et al. 2007

[p1,s1] = polyfit(A(fit_low:fit_hi),mod_comp(fit_low:fit_hi),1);
y        = polyval(p1,A);
comp_pre = p1(1);

```

```

% plot the compaction as a function of the scaling relation and the linear
% fit
figure(2)
plot (A,mod_comp(1:length(w)), '*'), hold on;
plot (A,y,'r');
title ('compaction prefactor');
xlabel(texlabel('(W/dx)^(1/beta))*dx [mm]'));
ylabel('Compaction [mm]');
%%%%%%%%%%%%%%%%%%%%%%%%%%%%%%%%%%%%%%%%%%%%%%%%%%%%%%%%%%%%%%%%%%%%%%%%

function w=data_width(surf)
%DATA_WIDTH calculates the interface width (Barabasi & Stanley 1995) given
%in Eq. 8 Ebner et al. 2009 JSG for every deformation step
% IMPUT VARIABLES:
% surf => surface with 1D simulated stylolites for every
% deformation step stacked along the first dimension
% OUTPUT VARIABLE:
% w => vector containing the interface width for every
% deformation

m = mean(surf,2);
ii = 1;

while ii <= length(m)
    jj = 1;
    sum = 0;
    while jj <= length(surf(1,:))
        sum = sum + (surf(ii,jj)-m(ii))^2;
        jj = jj + 1;
    end
    w(ii) = (sum/length(surf(1,:)))^0.5;
    ii = ii+1;
end
%%%%%%%%%%%%%%%%%%%%%%%%%%%%%%%%%%%%%%%%%%%%%%%%%%%%%%%%%%%%%%%%%%%%%%%%

% This script reads the output data from elle (.txt file) and scales and
% converts it to a .mat file (conversion from .txt -> .mat)
% load "elle" text file
filename = '0.05_0.2_0.04.txt';
S = load (filename);

%define dimensions of experiment
npart = 400; % number of particles in x direction
x_dim = 40; % physical dimension of the box in mm
dx = x_dim/npart; % Pixel size in mm

% initialise variables
ii=1;
numstrain=1;

% go through all deformation steps and sort the data accordingly
while ii < length(S(:,1))
    jj = 1;
    oldstrain = S(ii,1); % define 1. deformation step value from file
    while S(ii) == oldstrain % find all x/y values of the deformation step
        x(jj) = S(ii,2);
        y(jj) = S(ii,3);
        ii = ii+1;
        jj = jj+1;
    end
    [xs,ix] = sort(x); % sort data
    ys = y(ix);
    clear xnew ynew
    il = npart;
    xnew = linspace(0,1,il);
    i = 1;
    imax = length(xs);
    xs(imax+1) = 1;
    for j=2:il % calculate the average y at every x position
        av = 0;

```

---

```
k = 0;
while xs(i) < xnew(j)
    av = av+ys(i);
    i = i+1;
    k = k+1;
end
ynew(j-1) = av/k;
end
ynew = detrend(ynew,'constant'); % set mean height to zero
xnew = xnew(1:i1-1)+xnew(2)/2;
xs = xs(1:imax);

%stack 1D signals along the 1 matrix dimension
if numstrain == 1
    SYa = ynew;
else
    SYa = cat(1,SYa,ynew);
end
numstrain = numstrain+1;
end

Y_mat=SYa*x_dim; % scale the data to the correct physical dimension
%%%%%%%%%%%%%%%%%%%%%%%%%%%%%%%%%%%%%%%%%%%%%%%%%%%%%%%%%%%%%%%%%%%%%%%%%
```





## Curriculum Vitae

**Marcus Johannes Ebner**

- date/place of birth:* 07. December 1980, Linz / Austria
- nationality:* Austrian
- address:* Am Römerlager 23  
55131 Mainz, Germany  
ebnerm at uni-mainz.de
- education:*
- Oct 1995 - Jul 1999:* Gymnasium BORG Honauerstrasse in Linz
- Sept 1999 - Feb 2002:* Earth Sciences, Faculty of Natural Sciences, University of Vienna
- Feb 2002 - Sept 2004:* Geology, Faculty of Natural Sciences, University of Vienna
- Oct 2003 - Jun 2004:* Study abroad at the Geological Institute ETH-Zürich, Switzerland
- Diploma thesis: Deformation in the footwall of the Brenner-Normal-Fault: normal versus strike slip faulting  
Supervisors: Prof. Dr. B. Grasemann and Dr. K. Decker
- Sept 2004:* Graduation “summa cum laude” to Mag. rer. nat. at the Faculty Geosciences, Geography and Astronomy, University of Vienna
- Oct 2006 - Oct 2009:* PhD student, Tectonophysics, Institute of Geosciences, Johannes Gutenberg University Mainz
- PhD thesis: The development of stylolites, from small-scale heterogeneities to multi-scale roughness  
Supervisors: Prof. Dr. C. W. Passchier and PD Dr. D. Köhn